Master Thesis

Catalytic performance of Co-based spinel oxides in isopropanol oxidation

carried out for the purposes of obtaining the degree of Diplom-Ingenieur (Dipl.-Ing.),
submitted at TU Wien, Faculty of Technical Chemistry, by

Marianne IVKIĆ, BSc

[redacted]

[redacted]

under the supervision of

Associate Prof. Dipl.-Ing.in Dr.in techn. Karin Föttinger
(E165-01-4 Institute of Technical Catalysis)

Projektass. Alberto Tampieri, PhD
(E165-01-4 Institute of Technical Catalysis)

Vienna, January 2025

Marianne Ivkić, BSc

Affidavit

I declare in lieu of oath, that I wrote this thesis and carried out the associated research myself, using only the literature cited in this volume and ChatGPT for rephrasing purposes. If text passages from sources are used literally, they are marked as such.

I confirm that this work is original and has not been submitted for examination elsewhere, nor is it currently under consideration for a thesis elsewhere.

I acknowledge that the submitted work will be checked electronically-technically using suitable and state-of-the-art means (plagiarism detection software). On the one hand, this ensures that the submitted work was prepared according to the high-quality standards within the applicable rules to ensure good scientific practice "Code of Conduct" at the TU Wien. On the other hand, a comparison with other student thesis avoids violations of my personal copyright.

Vienna, January 2025

Marianne Ivkić, BSc

Acknowledgement

First and foremost, I would like to express my sincere gratitude to my professor, Karin Föttinger, for her insightful guidance and constructive feedback throughout this thesis. Her expertise and encouragement have been pivotal in shaping my research, and I truly appreciate the opportunities and support she has provided.

I would also like to extend my heartfelt thanks to my supervisor, Dr. Alberto Tampieri, for his patient guidance, constructive advice, and encouragement. His availability and expertise have been instrumental in navigating the challenges of this research, and I am sincerely grateful for his commitment to my academic growth.

I am deeply thankful to my entire research group for their camaraderie and assistance. Whether it was providing technical help, engaging in thoughtful discussions, or simply offering words of encouragement, their support made this journey not only manageable but enjoyable.

To my family, my mother, father, and brother, I owe endless gratitude. Their unconditional love, patience, and belief in me have been the foundation of my perseverance. Thank you for standing by me in moments of doubt and for celebrating every milestone, big or small, with me.

Finally, to my friends, thank you for being my oasis of relief in times of stress and for bringing much-needed laughter and perspective to this journey. Your motivation, kindness, and companionship have been indispensable, and I am truly grateful for the balance you brought to my life.

To all of you, this work is as much yours as it is mine. Thank you.

Kurzfassung

Diese Masterarbeit verfolgte primär zwei Ziele: Zum einen wurde die katalytische Leistung von Co-basierten Spinelloxiden in Isopropanol-Oxidationsreaktionen mithilfe eines kontinuierlichen Fest-Gas-Durchflussreaktorsystems untersucht. Der Fokus lag auf dem Co_3O_4-Katalysator, dessen Verhalten unter verschiedenen Reaktionsbedingungen, wie Temperatur, Reaktionsdauer, Heizrate, Gasflussraten und Anzahl der Reaktionszyklen, analysiert wurde. Fortgeschrittene Analysemethoden wie temperaturprogrammierte Reduktionsanalyse (TPR), Röntgenbeugung (XRD) und Brunauer-Emmett-Teller (BET)-Analyse wurden verwendet, um tiefere Einblicke in die strukturellen und mechanistischen Aspekte der katalytischen Prozesse zu gewinnen.

Als ein essenzieller Teil der Arbeit erwies sich hierbei die genauere Untersuchung eines Bereichs mit hoher Aktivität im Reaktionsprofil des Kobalt-Katalysators bei niedrigen Reaktionstemperaturen von 200°C, welcher bereits in zuvor erschienen Veröffentlichungen zu sehen war, allerdings noch nicht erklärt werden konnte. Des Weiteren zeigte sich eine Reduktion des Spinells bei einer Reaktionstemperatur von 400°C, während die Reaktionstemperatur von 200°C keinerlei Einfluss auf die Struktur des Festkörpers aufwies.

Das zweite Ziel beinhaltete eine vergleichende Analyse der Auswirkungen unterschiedlicher Kalzinierungstemperaturen, Isopropanol-zu-Sauerstoff-Verhältnisse und verschiedener Zusammensetzung von MCo_2O_4-Katalysatoren. Diese Tests wurden unter identischen Reaktionsbedingungen durchgeführt, um einen möglichst zuverlässigen Vergleich zwischen den Katalysatoren zu ermöglichen. Hierbei zeigten sowohl die Variation der Kalzinierungstemperatur, als auch die des Reaktanten-Verhältnisses keinen erheblichen Einfluss auf das Reaktionsergebnis zu haben. Der Vergleich unterschiedlicher MCo_2O_4-Katalysatoren hingegen zeigte deutliche Unterschiede in Bezug auf die Ausbeute und Selektivität der Reaktion. Hierbei wies besonders der Kupfer-Katalysator eine vielversprechende Aceton-selektivität auf. Während $NiCo_2O_4$ nur mittelmäßige katalytische Fähigkeiten aufwies, zeigten sich im Reaktionsprofil bei niedrigen Temperaturen kleiner als 400°C Aktivitätspeaks, welche, ähnlich zu Co_3O_4, auf charakteristische sehr reaktive Oberflächenzentren oder –spezies hinweisen. Die Studie lieferte wertvolle Einblicke in das katalytische Verhalten des Co_3O_4-Katalysators, jedoch zeigte sie auch die Notwendigkeit weiterer Untersuchungen an den anderen getesteten Katalysatoren auf, insbesondere den $CuCo_2O_4$- und $NiCo_2O_4$-Katalysatoren, die unter bestimmten Reaktionsbedingungen einzigartige mechanistische Merkmale zeigten.

Zusammenfassend bietet diese Arbeit eine solide Grundlage für das Verständnis des katalytischen Verhaltens von Co-basierten Spinelloxiden in der Isopropanol-Oxidation und weist auf wichtige Forschungsbereiche hin, um diese Katalysatoren für industrielle Anwendungen zu optimieren.

Abstract

This Master's thesis primarily pursued two objectives. Firstly, the catalytic performance of cobalt-based spinel oxides in isopropanol oxidation reactions was investigated using a continuous solid-gas flow reactor system. The focus was placed on the Co_3O_4 catalyst, whose behaviour under various reaction conditions, such as temperature, reaction duration, heating rate, gas flow rates, and the number of reaction cycles, was thoroughly analyzed. Advanced characterization techniques, including temperature-programmed reduction (TPR), X-ray diffraction (XRD), and Brunauer-Emmett-Teller (BET) surface area analysis, were employed to gain deeper insights into the structural and mechanistic aspects of the catalytic processes.

A key part of the study involved investigating the high activity peak observed in the reaction profile of the cobalt catalyst at a low reaction temperature of 200°C, a phenomenon noted in previous publications but not understood yet. Furthermore, the reduction of the spinel structure was observed at a reaction temperature of 400°C, whereas the reaction at 200°C had no discernible impact on the solid-state structure.

The second objective encompassed a comparative analysis of the effects of different calcination temperatures, isopropanol-to-oxygen ratios, and of the composition of various MCo_2O_4 catalysts. These experiments were conducted under identical reaction conditions to ensure reliable comparisons between the catalysts. Neither the variation in calcination temperature nor the reactant ratio significantly influenced the reaction outcomes. However, the comparison of different MCo_2O_4 catalysts revealed notable differences in terms of yield and selectivity. In particular, the copper-based catalyst ($CuCo_2O_4$) demonstrated promising acetone selectivity. While $NiCo_2O_4$ exhibited only moderate catalytic performance, its reaction profile below 400°C displayed low temperature activity peaks, similar to Co_3O_4, which could indicate characteristic surface sites or species of high activity.

The study provided valuable insights into the catalytic behaviour of the Co_3O_4 catalyst but also highlighted the need for further investigation of the other tested catalysts, particularly $CuCo_2O_4$ and $NiCo_2O_4$, which exhibited unique mechanistic features under specific reaction conditions.

In conclusion, this thesis establishes a solid foundation for understanding the catalytic behaviour of cobalt-based spinel oxides in isopropanol oxidation reactions and identifies key areas of research needed to optimize these catalysts for industrial applications.

Table of contents

1 Introduction

The selective oxidation of isopropanol (IPA) is a widely studied reaction in heterogeneous catalysis due to its role as a model reaction for investigating catalytic properties, such as redox activity and acid-base behaviour, as well as its industrial significance. IPA can undergo two distinct reaction pathways. The first involves dehydrogenation, producing hydrogen, which is subsequently oxidized to water. The second pathway begins with oxidative dehydrogenation to form acetone, which is then further oxidized to carbon dioxide (CO_2) and water. The ability to control these reaction pathways and achieve high selectivity towards desirable products, such as acetone, makes this reaction an excellent probe for evaluating catalytic performance. (S. Najafishirtari, 2021)

Spinel oxides, with the general formula AB_2O_4 represent a versatile class of materials in catalysis due to their structural stability, tuneable surface chemistry, and redox properties. Among them, cobalt-based spinel oxides have gathered particular attention due to the high activity of cobalt in oxidation reactions and the ability to engineer their electronic structure by substituting or doping with different cations. The octahedral and tetrahedral coordination of the cations in spinel structures can significantly influence the distribution of active sites, making them highly adaptable to specific catalytic applications. (A. K. Lebechi, 2022)

In this study, we investigate the catalytic performance of Co-based spinel oxides in the gas-phase oxidation of IPA, focusing on their activity, selectivity, and stability. The research aims to unravel the structure-performance relationships by examining the effects of cation composition, surface properties, and oxygen mobility on the catalytic behaviour. Special attention is paid to the potential trade-offs between activity and selectivity.

The significance of this research lies in both its fundamental and applied aspects. From a fundamental perspective, it contributes to the understanding of the catalytic mechanisms of spinel oxides, shedding light on the interplay between redox properties, oxygen vacancies, and reaction pathways. From an applied perspective, it provides insights into the design of efficient catalysts for selective oxidation reactions, which are pivotal in the production of value-added chemicals and environmental remediation.

This work builds on previous studies that have highlighted the potential of Co-based spinel oxides in oxidation catalysis but seeks to provide a more comprehensive understanding of their performance in IPA oxidation. The findings could have broader implications for developing spinel-based materials for other oxidation reactions, including methane activation and alcohol reforming.

The experimental approach combines detailed material characterization using techniques such as X-ray diffraction (XRD), and temperature-programmed desorption (TPD), with catalytic testing under controlled conditions. This methodology ensures a robust evaluation of the structure-activity correlations and the factors governing the catalytic performance of Co-based spinel oxides.

2 Theoretical background

2.1 Alcohol oxidation

Alcohol oxidation is a process that converts hydroxyl groups into other functional groups through an irreversible and exothermic reaction, which is thermodynamically favorable at all temperatures. However, the complex nature of these reactions, involving sequential and parallel pathways, necessitates the use of highly selective catalysts to achieve specific outcomes, such as selective oxidation, without overoxidation. Primary alcohols can be converted to aldehydes but risk further oxidation to carboxylic acids, while secondary alcohols generally produce ketones that are resistant to further transformation. Traditional methods rely on stoichiometric oxidants like chromium or manganese compounds, which pose environmental and economic challenges, prompting a shift towards greener catalytic solutions using molecular oxygen or air.

To enhance sustainability, the development of novel heterogeneous catalysts that rely on abundant elements and milder reaction conditions is critical. This need becomes even more pressing for higher alcohols, which often require lower temperatures and liquid-phase reactions. These systems are particularly complex when aerobic oxidation is involved, as the interplay of gas, liquid, and solid phases adds to the challenge, emphasizing the importance of continued innovation in catalyst design. (A. Tampieri, 2024)

In the oxidation of isopropanol, two primary pathways are possible. The first involves oxidative dehydrogenation, where isopropanol is converted to acetone, which can subsequently undergo further oxidation, potentially leading to complete oxidation to CO_2 and water. Alternatively, isopropanol can undergo simple dehydrogenation to produce acetone and hydrogen. The hydrogen formed in this process can later oxidize to water, resulting in the same overall products as those obtained through oxidative dehydrogenation. (Wagner, 1934) (R. Kellogg, 1998)

- **Dehydrogenation to acetone:**

$$C_3H_7OH \rightarrow C_3H_6O + H_2$$

- **Oxidative dehydrogenation to acetone:**

$$C_3H_7OH + \frac{1}{2}O_2 \rightarrow C_3H_6O + H_2O$$

- **Total oxidation to CO_2 and water:**

$$C_3H_7OH + 4O_2 \rightarrow 3CO_2 + 4H_2O$$

2.2 Fundamentals of catalytic testing in reactor systems

In the development of catalysts for novel processes or the optimization of existing catalytic systems, several distinct stages can be identified. This progression encompasses the initial conceptualization of a process or catalyst, followed by catalyst preparation, screening, the establishment of reaction networks, kinetic analysis, life testing, and ultimately scaling up to pilot-plant operations prior to implementation. Throughout this development, iterative feedback loops are integral to refining both the catalyst and the process.

As development advances, the number of catalyst formulations typically decreases, while the associated costs, equipment requirements, and labor demands increase significantly. This necessitates a systematic and efficient approach to laboratory-scale experimentation. Selecting the appropriate reactor is a critical step in this process, as the criteria for laboratory-scale catalyst testing differ from those for industrial reactors. It is essential to avoid a direct miniaturization of the industrial setup ("Dinky Toy" approach), as laboratory reactors are specifically designed to yield precise and intrinsic data about catalyst behaviour.

Scaling down reactor systems offers numerous benefits, including reduced equipment costs, lower material and utility demands, minimal waste generation, enhanced safety, and decreased laboratory infrastructure requirements. However, smaller-scale experimentation also imposes stricter demands on accuracy and necessitates the use of representative catalyst samples.

To accurately determine the intrinsic properties of a catalyst, such as reaction kinetics and selectivity, experimental conditions must meet several criteria: efficient contact between reactants and the catalyst, the absence of mass and heat transport limitations both within and around catalyst particles, and a well-characterized reactor system with clearly defined residence time distributions under isothermal conditions. Meeting these requirements ensures that the data obtained reflects the true catalytic properties without interference from extraneous factors. (F. Kapteijn, 2008)

2.2.1 Catalytic reactors

Catalytic reactors are typically classified by their operational modes (Figure 1), steady-state or transient, or by the contact and mixing mechanisms within fluid-solid systems, both of which are essential for achieving uniform material characteristics. Effective interaction between the catalyst and reaction mixture is critical in all applications to ensure optimal reaction efficiency and reproducibility.

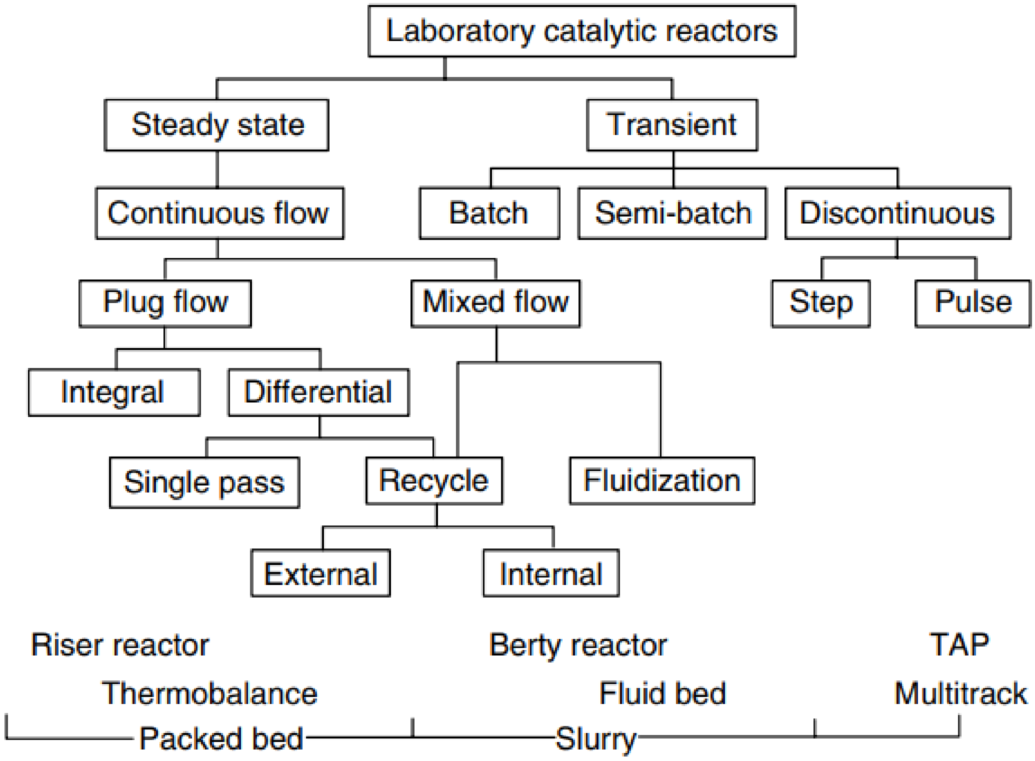

Figure 1: Classification of laboratory reactors according to mode of operation with permission from (F. Kapteijn, 2008)

Steady-state reactors, particularly packed-bed configurations, are widely employed in material synthesis for their simplicity, scalability, and cost efficiency. These reactors maintain constant operating conditions, making them ideal for the large-scale production of uniform materials, such as advanced ceramics, catalysts, and polymers. Their ability to sustain continuous processes makes them indispensable in industrial applications like the synthesis of nanomaterials, where consistent temperature and pressure are crucial for achieving controlled particle size and morphology.

Transient reactors, although less commonly used for direct material synthesis, are valuable in studying reaction mechanisms and optimizing synthesis protocols. Systems like the Temporal Analysis of Products (TAP) reactor and Multitrack reactor provide detailed kinetic and mechanistic information, which is critical for designing efficient synthesis routes. For instance, TAP reactors can evaluate reaction pathways in the production of metal-organic frameworks (MOFs) or assess intermediates in the formation of spinel oxides.

Transient operation using isotopically labelled species, such as positron emission profiling or steady-state isotope transient kinetic analysis (SSITKA), offers dual advantages. These techniques not only provide steady-state data but also deliver insights into individual reaction steps, facilitating the fine-tuning of synthesis processes for complex materials like perovskites or zeolites.

In the synthesis of spinel oxides, for instance, packed-bed reactors ensure uniform deposition and crystallization, crucial for maintaining their electrochemical and thermal stability. For photocatalytic materials like titanium dioxide or bismuth vanadate, transient reactor systems help optimize reaction conditions to enhance photocatalytic efficiency and surface activity.

Despite their versatility, catalytic reactors face challenges such as heat and mass transfer limitations, particularly in the production of highly porous or hierarchical structures. Reactor miniaturization and advanced control systems are being developed to address these limitations, enabling precise control over reaction parameters, reducing waste, and enhancing safety. Innovations like microreactors have opened new possibilities in high-throughput material synthesis, allowing for the rapid screening of conditions for producing advanced nanomaterials. (F. Kapteijn, 2008), (G. F. Forment, 2010)

2.2.2 Introduction to packed-bed tubular reactors

The packed-bed tubular reactor is the most widely used and straightforward laboratory reactor for gas-solid reaction systems, often referred to as the "workhorse" of catalytic testing. It consists of a reaction tube where the catalyst is typically secured between quartz wool plugs on a sintered frit or wire mesh gauze. The choice of tube material depends on the reaction conditions: glass is suitable for low-temperature and low-pressure operations, while steel is required for high-pressure applications, and quartz or ceramics, such as SiC or alumina, are ideal for high-temperature conditions where steel may lose strength. Ceramics are particularly advantageous in high-pressure and high-temperature environments due to their superior durability.

The reactor's optimal internal diameter ranges from 4 to 6 mm to ensure efficient heat transfer to or from the catalyst bed. It can feature various geometries, including straight, U-shaped, or concentric designs, where the catalyst is often positioned in the inner tube. To enhance heat transfer and achieve plug flow conditions, the porous catalyst is frequently diluted with an inert material, such as SiC, known for its excellent thermal conductivity. Additional inert materials may be placed before and after the catalyst bed to preheat the reactant stream and prevent fluidization in up-flow setups. Packed-bed reactors are versatile and can also accommodate liquid-solid reactions.

Operation modes for the packed-bed reactor depend on the desired conversion levels. In differential mode, the reactor handles low conversions, while integral mode is suited for high conversions. Recirculating the reactor outlet flow allows the system to approximate a well-mixed reactor, similar to a continuously stirred tank reactor (CSTR). This adaptability and simplicity make packed-bed reactors a fundamental tool in catalytic reaction studies and material synthesis processes. (F. Kapteijn, 2008)

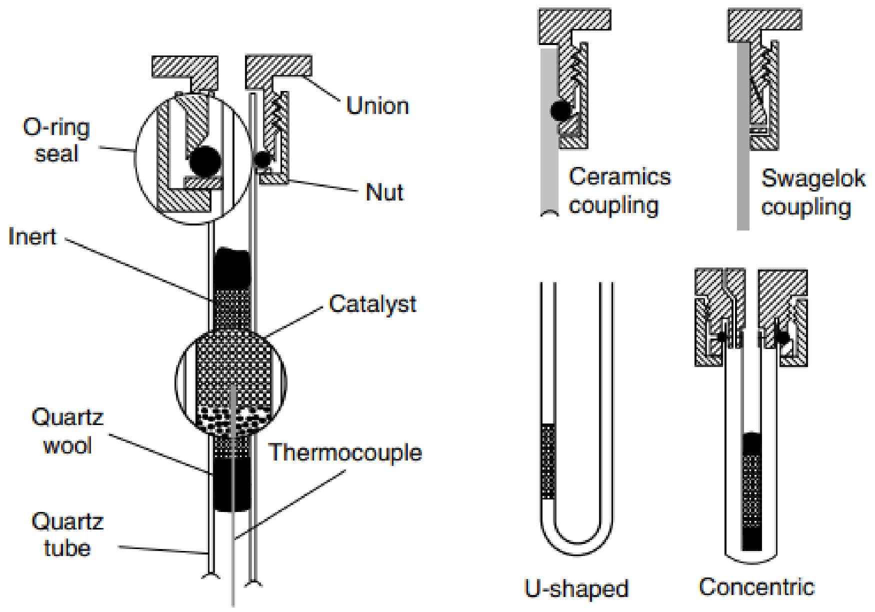

Figure 2: Packed bed reactor design, examples of geometries and connections with permission from (F. Kapteijn, 2008)

2.3 Catalysts and catalysis

2.3.1 Introduction to catalysis

As early as the 18th century, scientists recognized that adding certain compounds could markedly accelerate specific chemical reactions, with these compounds remaining chemically unchanged upon completion of the reaction. Importantly, some reactions could only proceed with the involvement of these unique compounds. In 1835, Swedish chemist Jöns Jakob Berzelius coined the term "catalysis" to describe this phenomenon. He proposed that a catalyst, the compound facilitating the reaction, increases its rate without undergoing any permanent transformation.

Modern scientific understanding, however, has refined Berzelius’s theory. It is now clear that while a catalyst does indeed facilitate reactions, it undergoes a temporary chemical transformation during the reaction. This temporary change enables the catalyst to interact effectively with the reactants, but it reverts to its original structure by the reaction's end, thus allowing it to be used repeatedly across multiple reaction cycles. Despite Berzelius’s initial idea that catalysts could function indefinitely without alteration, practical challenges arise in real-world applications.

Most catalysts in industrial and laboratory settings are solid materials, providing extensive surface areas where chemical reactions occur more readily than they would in the gas or liquid phases. Over time, however, solid catalysts face inevitable limitations in efficiency due to surface contamination (deactivation). In severe cases of deactivation, the catalyst must be regenerated to restore its functionality.

Wilhelm Ostwald later refined Berzelius's initial concept by offering a more nuanced definition: "A catalyst changes the rate but not the chemical equilibrium of a reaction." This distinction highlights the essential role of catalysts in reaction kinetics without altering the fundamental thermodynamic balance of the system, underscoring their unique role in both industrial processes and natural systems. (R. Prins, 2022)

2.3.2 Difference between homogeneous and heterogeneous catalysis

In homogeneous catalysis, the catalyst, reactants, and products all coexist in the same phase. An example of this process is the production of acetic acid from methanol and carbon monoxide. In contrast, heterogeneous catalysis involves the catalyst being in a solid phase, while the reactants and products are in either the gas or liquid phase. Gas-solid heterogeneous catalysis is commonly employed in the refining and base chemicals industries, whereas liquid-solid heterogeneous catalysis is prevalent in the fine chemicals sector.

In heterogeneous catalysis, reactions occur exclusively on the surface of the solid catalyst, making the catalyst's porosity a critical factor in maximizing its efficiency. Porous particles play a pivotal role in providing an extensive internal surface area, significantly enhancing the availability of active sites for catalytic reactions. These pores facilitate efficient transport of reactants and products within the catalyst structure, reducing diffusion limitations and ensuring optimal contact with active sites. Moreover, the porosity of the particles mitigates the challenges associated with particle sintering, as the distributed pore network helps maintain structural stability and a high effective surface area, thereby preserving catalytic activity over time.

In heterogeneous catalysis, only the atoms on the catalyst's surface, rather than those within the bulk of the particles, are accessible to the reacting molecules and contribute to the catalytic process. One advantage of homogeneous catalysis is that all catalyst complexes, and thus all metal atoms, are accessible for the reaction. However, a major drawback is the difficulty in separating the catalyst from the products, as they are in the same phase. In contrast, heterogeneous catalysis offers easier separation because the catalyst and products exist in different phases. In a heterogeneous continuous process, the catalyst remains within the reactor, and in a batch process, it can be easily separated by filtration. (R. Prins, 2022)

2.3.3 Mechanisms of heterogeneous catalytic reactions

Heterogeneous catalysis plays a crucial role in numerous industrial processes, including the production of chemicals, fuels, and environmental management. The detailed understanding of the mechanisms by which these reactions occur has been shaped by several key models that describe the interaction between reactants and the catalyst surface. This chapter discusses the mechanisms of heterogeneous catalytic reactions, with a focus on the Langmuir-Hinshelwood, Eley-Rideal, and Mars van Krevelen models.

The key concept of catalytic reactions is the idea that the rate of reaction depends on the coverage of the adsorbed species. Furthermore the adsorption of reactants occurs in three steps:

Adsorption of reactants: The reactant molecules (denoted as A and B) adsorb onto active sites on the catalyst surface. The adsorption can either be physisorption or chemisorption, with the latter being stronger and leading to more significant interactions with the surface.

Surface reaction: Once adsorbed, the reactants can react to form products, which then desorb from the surface. The rate of reaction is influenced by the number of active sites available, the concentration of the reactants on the surface (coverage), and the activation energy of the reaction.

Desorption: Upon formation on the catalytic surface, the reaction products dissociate from the active sites and are released into the surrounding medium. This final step is essential for liberating the active sites, allowing the adsorption of new reactant molecules and ensuring the continuation of the catalytic cycle. Effective desorption is critical for maintaining catalyst activity and preventing the accumulation of products, which could otherwise hinder subsequent reactions.

The Langmuir-Hinshelwood mechanism is one of the most fundamental and widely accepted models in heterogeneous catalysis. It assumes that both reactants adsorb on the catalyst surface, where they can undergo a reaction. Examples include hydrogenation and oxidation reactions.

The Eley-Rideal mechanism differs from the Langmuir-Hinshelwood mechanism in that it assumes one reactant adsorbs on the surface while the other reacts directly with the adsorbed species without adsorption. In this model, one of the reactants (say A) is adsorbed on the catalyst surface, and the other reactant (B) approaches the surface in the gas phase and reacts with the adsorbed species A. This is particularly important for reactions where one reactant has a much higher adsorption energy than the other, or where one reactant is much less likely to adsorb at low temperatures.

This model is especially useful in describing catalytic reactions involving a highly reactive adsorbate and a less reactive species in the gas phase, such as in certain oxidation or reduction reactions. A common example of the Eley-Rideal mechanism is the reaction of atomic oxygen with hydrocarbons on metal surfaces, where the hydrocarbon adsorbs while the oxygen comes from the gas phase.

The Mars van Krevelen mechanism takes often place in redox reactions, particularly those involving transition metal oxides as catalysts. In this mechanism, the catalyst undergoes periodic oxidation and reduction cycles as part of the reaction process. The key feature of the Mars van Krevelen model is that the catalyst itself participates in the reaction by changing its oxidation state, in contrast to the Langmuir-Hinshelwood and Eley-Rideal models, where the catalyst is assumed to remain in a fixed oxidation state.

In the Mars van Krevelen mechanism, one of the reactants reacts with the surface of the catalyst, leading to the formation of oxygen vacancies on the surface. These vacancies are then filled by the other reactant, typically in a process where the catalyst returns to its initial oxidation state.

This mechanism is commonly observed in catalytic oxidation reactions and is especially relevant in the case of metal oxide catalysts such as CeO_2 and TiO_2, which can undergo reversible changes in oxidation state.

Each of these mechanisms, Langmuir-Hinshelwood, Eley-Rideal, and Mars van Krevelen, offers a distinct perspective on how catalytic reactions proceed. The Langmuir-Hinshelwood mechanism is most applicable when both reactants adsorb on the surface and react in close proximity. The Eley-Rideal mechanism is more suitable when one reactant is strongly adsorbed and the other interacts directly from the gas phase. Finally, the Mars van Krevelen mechanism is important for reactions where the catalyst itself undergoes changes in oxidation state, such as in redox processes.

In practice, many catalytic reactions can involve a combination of these mechanisms, depending on factors such as the nature of the catalyst, the reactants, the temperature, and the pressure. Understanding the underlying mechanism allows for the optimization of catalyst design and reaction conditions, which are essential for improving catalytic efficiency and selectivity in industrial applications. (G. Rupprechter, 2023), (G. A. Somorjai, 2010), (M. Boudart, 1984)

2.3.4 Deactivation and regeneration of catalysts

Catalysts often experience a significant loss of their activity during operation, primarily due to three main causes: solid-state transformations, poisoning, and coking. Understanding the mechanisms behind these processes and the methods of catalyst regeneration is critical for maintaining long-term catalyst performance and optimizing industrial processes.

Solid-State Transformations

Solid-state transformations occur when the physical structure of the catalyst material undergoes changes due to prolonged exposure to operational conditions, such as high temperature or the presence of impurities. These transformations can lead to reduced surface area or altered pore structures, thus decreasing the catalyst's active sites. For example, alumina may transform from the γ-structure to the more stable α-modification, or silica supports can crystallize when exposed to high temperatures or contaminating substances like sodium ions. Regeneration of catalysts affected by solid-state transformations typically involves techniques such as thermal treatment to restore the catalyst’s original structure. For instance, calcination, a process involving heating the catalyst in the presence of air, can reverse some types of crystallization, promoting the reversion to the original phase and thus recovering some catalytic activity. However, this process is not always effective for all types of transformations, and more advanced regeneration methods may be necessary for materials that have undergone severe structural changes, such as sintering or severe crystallization.

In addition, sintering (the coalescence of small crystallites into larger ones) and ripening (where atoms move from smaller to larger crystallites) are common phenomena in catalysts like platinum supported on alumina. These processes lead to a reduction in the accessible surface area and thus catalyst activity. To regenerate catalysts suffering from sintering, methods such as reduction (exposing the catalyst to a hydrogen or other reducing environment) can help restore smaller active particles or reestablish more favorable surface structures. While sintering can often be mitigated by adjusting temperature and gas-phase atmosphere during regeneration, some catalysts may require more specific treatment, including the addition of stabilizers or promoters to prevent sintering from occurring in the first place.

Poisoning

Poisoning occurs when impurities in the feed stream irreversibly bind to the active sites of the catalyst, blocking the surface from interacting with the reactants. Poisoning is a major concern in many catalytic processes, as even trace amounts of certain compounds can deactivate the catalyst. For example, sulfur compounds can poison platinum-based reforming catalysts, while nickel-based catalysts in steam reforming processes can be poisoned by compounds like sulfur and carbon monoxide. The primary method for regenerating a poisoned catalyst is to remove the poisons from the catalyst surface. In many industrial settings, "guard" reactors are employed upstream of the main reaction to convert or remove poisonous impurities before they reach the catalyst. These guard reactors typically use less active catalyst materials, such as Co/Mo, which are specifically chosen to neutralize sulfur or other poisons without significantly affecting the main catalytic process.

In some cases, poisoned catalysts can be regenerated by exposing them to specific treatments that remove or neutralize the poison. For example, for catalysts poisoned by sulfur, regeneration often involves high-temperature oxidation or exposure to reducing agents, which can facilitate the removal of sulfur from the catalyst’s surface. In other cases, solvents or washing techniques can be used to physically remove poison residues from the catalyst surface, restoring the activity to some extent. However, it is important to note that some poisons bind so strongly to the catalyst that regeneration may not be fully successful. In such cases, the catalyst may require replacement after a certain period of operation, despite periodic regeneration efforts. (M. D, 2015)

Coking

Coking, the deposition of carbonaceous residues on the catalyst surface, is a major cause of deactivation in many petrochemical and petroleum refining processes. Coking occurs when carbon-containing compounds, often by-products of the reaction or impurities, decompose and form carbon deposits (referred to as coke) that adhere strongly to the catalyst. This reduces the available active sites on the catalyst and can lead to a sharp decrease in catalytic activity. Coking is particularly common in processes like catalytic cracking, reforming, and dehydrogenation, where high molecular weight species, such as aromatic compounds or olefins, polymerize and deposit on the catalyst.

The regeneration of coked catalysts typically involves high-temperature treatments that remove the carbon deposits by combustion. In this process, the catalyst is heated in an oxidizing environment, such as air, to burn off the coke and restore the surface area. In some cases, controlled regeneration can be achieved by heating the catalyst in a fluidized bed or using moving bed reactors, which continuously regenerate the catalyst without interrupting the reaction process. Fluidized bed regeneration is particularly effective in processes where catalyst circulation is already part of the reaction system, allowing for continuous catalyst activation and deactivation. However, this process must be carefully controlled to avoid excessive oxidation or thermal damage to the catalyst.

Another method of coke removal is steam treatment, in which the catalyst is exposed to steam at high temperatures. This process helps break down the carbonaceous deposits into gaseous products like methane and carbon dioxide, which are then removed. Steam regeneration is particularly useful in preventing the catalyst from undergoing excessive thermal degradation, which could permanently alter its structure.

In some cases, regeneration may not fully restore the catalyst's original performance, especially if the coke deposits are extensive or if the catalyst has been severely damaged by the coking process. In such cases, partial regeneration may allow the catalyst to be reused for a limited time, but eventually, the catalyst may need to be replaced or undergo more intensive regeneration procedures. (Ostrovskii, 2022)

2.3.5 Spinel oxides

Spinel oxides are a versatile class of metal oxides known for their diverse properties, including electrochemical energy storage, electrocatalysis, high thermal stability, superconductivity, and ferromagnetism. These characteristics make them suitable for various applications, such as sensors, supercapacitors, fuel cells, energy storage, catalysis, and photocatalysis.

Recent advancements in spinel oxide synthesis have broadened their application range, especially in fuel cell and metal–air technologies, where they serve as efficient electrocatalysts for the oxygen reduction and evolution reactions (ORR and OER). Their redox stability and multiple valence states make them promising alternatives to noble metals in these reactions.

Spinel oxides also exhibit excellent resistance to chemical attacks and mechanical strength, making them ideal for refractory materials. Their photocatalytic properties enable the degradation of environmental pollutants, such as phenols and pesticides. Furthermore, their magnetic properties, including large saturation magnetization and high Curie temperature, make them suitable for applications in magnetic sensing and data storage. (R. J. Harrison, 1998)

The AB_2O_4 lattice structure consists of two sub-lattices: the A-site, which hosts tetrahedrally coordinated divalent metal ions, and the B-site, where trivalent metal ions are arranged in octahedral coordination. This structure adopts the $Fd\bar{3}m$ space group. Spinel oxides, with the general formula AB_2O_4, feature an anionic sublattice that forms a cubic arrangement. In this structure, 1/8 of the tetrahedral A-sites and 1/2 of the octahedral B-sites are occupied by cations. Specifically, in the AB_2O_4 unit cell, 8 out of 64 tetrahedral sites are filled by A^{2+} cations, while 16 out of 32 octahedral sites are occupied by B^{3+} cations.

The spinel structure can exhibit strong frustration when it crystallizes in the cubic $Fd\bar{3}m$ space group, particularly when a corner-shared tetrahedral network, known as the "pyrochlore sublattice," is formed by the B-site cations in the absence of distortions. Larger cations tend to occupy the B-sites, as the octahedral interstices are more spacious than the tetrahedral ones, which accommodate smaller cations. A spinel is termed a "normal spinel" if only the B cations occupy the octahedral sites. If both A and B cations are found in equal numbers at the octahedral sites, the spinel is classified as an "inverse spinel." When an unequal distribution of A and B cations occurs at the octahedral sites, the structure is referred to as a "mixed spinel." (D. Srikala, 2024), (K. E. Sickafus, 2004)

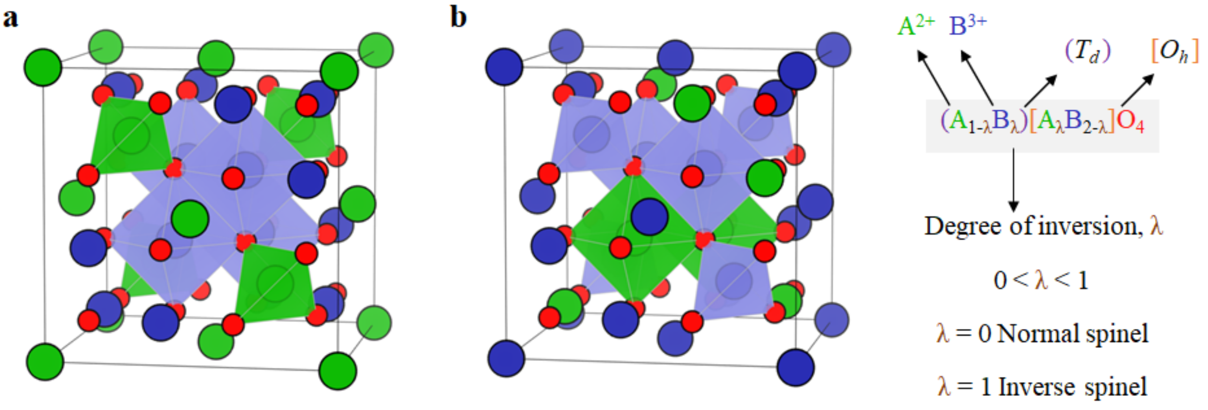

Figure 3: Normal (a) and inverse (b) spinel structure.

2.4 Synthesis methods: Coprecipitation and combustion synthesis

2.4.1 Coprecipitation synthesis

The coprecipitation technique is a widely employed synthesis method within materials science, particularly valued for producing homogeneous solid mixtures, including metal oxides, hydroxides, and composite materials. Known for its simplicity and scalability, this technique enables the production of materials with fine particle size and uniform chemical composition, making it an attractive approach for both research and industrial applications.

Coprecipitation begins with the preparation of a solution containing the desired metal ions, typically achieved by dissolving metal salts such as nitrates, chlorides, or sulfates in water. The precipitation process is then initiated by adding a precipitating agent, often an alkaline solution like sodium hydroxide (NaOH) or ammonium hydroxide (NH_4OH), which raises the pH level. This pH increase drives the metal ions to precipitate as hydroxides, forming a solid phase within the solution.

Control of the synthesis environment, such as pH, temperature, and the concentrations of reactants, is crucial for determining the characteristics of the final material. Consistent pH levels, for example, can promote uniform particle size and inhibit the development of secondary, undesired phases. Other factors, including mixing speed and the order of reagent addition, also influence the morphology and particle distribution of the resulting precipitate.

The coprecipitation mechanism relies on the simultaneous precipitation of ions, which induces the rapid formation of nuclei, followed by particle growth once the ions' concentration surpasses the solubility threshold. This fast nucleation enables the formation of a homogeneous material, even for complex compounds. One of the notable advantages of this method is its ability to produce chemically uniform products, making it especially useful for synthesizing complex oxides and multi-component materials where precise elemental distribution is critical to material performance.

Following precipitation, the solid product is typically isolated through filtration or centrifugation, then washed to remove residual ions or impurities. The resulting precipitate is dried and, if needed, subjected to calcination, a thermal treatment that converts the precursor into the oxide form and enhances its crystallinity. Calcination settings, including temperature and duration, are carefully chosen based on the material's thermal stability and the properties desired for the final product. Depending on the target characteristics, calcination can be performed in various atmospheres, such as air, inert gases, or reducing conditions.

Due to its versatility, coprecipitation is widely applied in the synthesis of catalysts, ceramics, battery electrodes, and magnetic materials, among other fields. For instance, in the production of battery cathodes, the homogeneity achieved through coprecipitation is essential for optimizing electrochemical performance. In catalysis, this method enables fine dispersion of active sites, thereby maximizing catalytic efficiency.

Nonetheless, coprecipitation presents certain challenges. For example, agglomeration of particles can occur, which reduces the surface area and can negatively affect the material's reactivity. Achieving consistent control over particle size and morphology can be challenging, as slight variations in pH or temperature significantly affect the outcome. To address these limitations, advanced approaches, such as controlled pH conditions, the use of surfactants to stabilize particle formation, or ultrasonication, are often employed. (A. Yelten-Yilmaz, 2018) (J. Subrt, 2006)

2.4.2 Combustion synthesis

Combustion synthesis (CS) represents a highly energy-efficient technique well-suited for large-scale, continuous production of diverse material types. This method relies on the principles of self-sustaining exothermic reactions, which progress independently of external heat sources, thereby making CS considerably more energy-efficient compared to traditional synthesis methods. Solution combustion synthesis (SCS), a specialized form of CS, is characterized by dissolving reactants at the molecular level in an aqueous medium, thus allowing precise control over material composition and tuneable properties, such as particle size, crystallinity, surface area, and chemical composition.

SCS enables fine control over material characteristics by adjusting specific variables, including the type of reactants, fuel-to-oxidizer ratios, and combustion conditions. Such control is essential as it directly influences the quality and suitability of the materials for energy storage applications. Furthermore, the release of gas during SCS promotes the formation of nanostructures with high specific surface areas.

The SCS process itself is initiated by preparing a reactive solution that comprises an oxidizing agent, such as metal nitrates, and a fuel, which could include compounds like glycine, citric acid, or urea. These components are typically dissolved in water, allowing the formulation of a homogenous mixture with a carefully controlled oxidizer-to-fuel ratio. This ratio is critical, as it governs the thermal properties of the reaction, including the ignition temperature, heat release, and reaction kinetics. The combustion process in SCS can be initiated through two primary mechanisms: volume combustion synthesis (VCS) or self-propagating high-temperature synthesis (SHS).

In VCS, the reactive solution is uniformly heated to a specific ignition temperature (T_{ig}), at which point combustion begins uniformly across the entire volume. This mode of reaction results in the homogeneous formation of a solid product, which can be advantageous when consistency in material distribution is required throughout the product matrix. VCS thus enables a level of uniformity across the entire reaction medium that may be essential for applications where material homogeneity is crucial.

The SHS method, by contrast, initiates the reaction through localized heating, which triggers a combustion wave that propagates through the reactive solution. This mode allows distinct control over particle morphology, microstructure, and other material characteristics due to the sequential propagation of the combustion front. This wave-based approach is particularly effective in cases where controlled material textures and structures are desired, as the reaction front can influence grain boundaries, porosity, and other features at the microscopic level. In both VCS and SHS, the exothermic nature of the reaction ensures that, once initiated, the process becomes self-sustaining and does not require further external energy input. (N. Sisakyan, 2023)

2.5 Mass spectrometry and its application in reaction monitoring

2.5.1 Principles of mass spectrometry

Mass spectrometry has become one of the most vital analytical techniques due to its exceptional sensitivity, low detection limits, rapid processing, and wide-ranging applications. Recent developments in analytical chemistry emphasize its use in biochemical fields, including proteomics, metabolomics, high-throughput drug discovery, and pharmacokinetics. Mass spectrometry is also frequently applied in environmental monitoring, food safety, forensic science, natural product analysis, and industrial process control. Beyond these areas, its applications extend to atomic physics, reaction kinetics, geochronology, inorganic analysis, ion-molecule reaction studies, and thermodynamic parameter determination.

The initial step in mass spectrometric analysis is ionizing the compound in the gas phase, often through electron ionization. This process generates a molecular ion that typically fragments, producing ions with distinct chemical properties. Fragmentation can yield either a radical with an even-electron ion or a neutral molecule with a radical cation, each fragment carrying unique information about the structure of the precursor molecule. These ions are then separated based on their mass-to-charge (m/z) ratios within the spectrometer and detected proportionally to their abundance.

The resulting mass spectrum is displayed as a plot of ion abundance versus m/z. The most intense peak in this spectrum, the base peak, is standardized to an abundance of 100%, with all other peaks scaled accordingly. Although terms like "ion counts" or "relative intensity" are sometimes used, "relative abundance" is the most precise descriptor for the y-axis. The x-axis, labelled m/z, represents the dimensionless mass-to-charge ratio. In cases where m is the mass in atomic mass units (u) and z is the charge in elementary charges, m/z denotes a unitless ratio; for convenience, this ratio can be expressed in Thomson (Th) units.

In a spectrum of a pure compound, the molecular ion appears as the highest m/z peak, indicating the molecular mass. For stoichiometric and mass spectrometric calculations, scientists use different mass definitions: average mass, based on the atomic weights of each element's isotopes, or nominal and monoisotopic masses. The nominal mass uses the predominant isotope of each element rounded to the nearest whole number, while the monoisotopic mass accounts for isotopic mass defects. (E. d. Hoffmann, 2007)

2.5.2 Setup and operating principle

A mass spectrometer typically comprises several core components: a sample inlet for introducing the analyte (such as a gas chromatograph or direct insertion probe), an ionization source to generate ions from the sample, one or more mass analyzers to separate these ions, a detector to count the ions exiting the final analyzer, and a data processing system to generate the mass spectrum in a usable format. In some designs, the sample inlet and ionization source are combined, or the mass analyzer and detector are integrated into a single unit.

A mass spectrometer follows a series of essential steps: first, ions are generated from the sample in the ionization source. These ions are then separated based on their mass-to-charge (m/z) ratios in the mass analyzer. Selected ions may undergo further fragmentation, with the resulting fragments analysed in a subsequent analyzer if present. Next, ions emerging from the last analyzer are detected, and their relative abundances are measured by the detector, which converts these ions into electrical signals. Finally, the detector signals are transmitted to a computer for data processing, and the system is controlled through feedback mechanisms to ensure precise and accurate analysis.

The initial step in mass spectrometry involves a variety of ionization techniques, each optimized for specific sample types and analytical goals. A common method is electron ionization (EI), where electrons collide with molecules, transferring energy and forming positively charged ions. For more delicate or larger molecules, such as biomolecules, gentler techniques are often preferred, including electrospray ionization (ESI) and matrix-assisted laser desorption/ionization (MALDI). In ESI, the sample is dispersed into a fine spray and ionized via an applied electric field, while MALDI uses a laser to ionize molecules within a protective matrix. These varied ionization methods extend the versatility of mass spectrometry, making it suitable for analysing a broad spectrum of samples, from small organic compounds to large biomolecules like proteins and nucleic acids. (E. d. Hoffmann, 2007)

The subsequent step in analyzing an analyte by mass spectrometry involves separating the ions by means of a mass analyzer. Among the most widely utilized analyzers are the quadrupole, time-of-flight (TOF), ion trap, and orbitrap analyzers. A particularly common type is the quadrupole mass filter, which comprises four parallel, cylindrical or hyperbolic metal rods, typically crafted from stainless steel or molybdenum. To enhance durability, these rods are sometimes coated with a ceramic layer to resist corrosion.These rods are generally 15–20 cm in length and approximately 1 cm in diameter.

The quadrupole's filtering function is achieved by applying a direct current (DC) voltage to one pair of electrodes and a radio frequency (RF) voltage to the other pair. This configuration induces oscillations in the incoming ions, but only ions with a specific mass-to-charge ratio (m/z) have stable oscillations and can pass through the quadrupole mass filter. Ions with other m/z values experience unstable oscillations and are thus ejected from the filter. This selective passage is due to the electrostatic potential, which guides particles centrally along the path between the four electrodes. Ions with unstable oscillations deviate and exit the filter.

After passing through the quadrupole mass filter, the ions are detected and converted into electrical pulses for measurement. This process is repeated sequentially for ions of varying m/z values until all target analytes have been detected. Due to the high speed of this process, multiple elements can be detected in rapid succession (approximately 0.01 seconds per element) with high sensitivity, enabling efficient and precise analysis. (Thomas, Beginners's Guide to ICP-MS: PartVI - The Mass Analyzer, 2001)

Once the analyte has been separated, the next step is its detection, for which various methods can be employed. One of the most commonly used techniques is the discrete dynode electron multiplier (DDEM). To reduce background signals caused by scattered or neutral particles, this detector is placed off-axis after the quadrupole mass filter.

After exiting the mass filter, the ions pass through a curved path leading to the first dynode. Upon impact with this dynode, ions release energy-specific secondary electrons. These secondary electrons trigger further electron production due to the dynode's characteristic design, with the electrons being accelerated to the next dynode. This cascade effect continues, amplifying the electron output after each dynode. The accumulated electron pulse is subsequently captured by the anode, which converts it into a measurable signal expressed as counts per second.

The detection process in a discrete dynode electron multiplier is comparable to that of a channeltron, where ions strike a glass cylinder lined with semiconductor-like materials, generating secondary electrons that are further amplified as they travel through the narrowing cone. However, the DDEM offers superior sensitivity, owing to both the materials used and the differences in the electron generation process.

This detection method exhibits linear sensitivity across a concentration range from ng/L to several hundred µg/L. With specific modifications, the dynamic range can be extended to hundreds of mg/L. One early approach to controlling ion flux at the detector involved applying suboptimal voltages in the ion optics or directly at the quadrupole, thereby reducing the number of ions reaching the detector. However, this required prior knowledge of the sample to determine the correct voltage. Another approach involved using two detectors and performing two scans with a single detector, leading to the development of a two-stage discrete dynode detector.

The two-stage DDEM allows for the simultaneous measurement of both high and low concentrations in a single scan. Ion signals are first measured and evaluated analogously at the central dynode. If the ion count surpasses a predetermined threshold, the signal is processed using analog circuitry. If the threshold is not reached, the ions follow the normal dynode path and are measured in pulse mode. This process is fully automated, providing the advantage of detecting both analog and pulsed signals in one scan.

Despite some variations in this method, all configurations share the benefit of requiring only a single scan to measure both low and high concentrations. As a result, sample throughput and the total data acquisition rate can be significantly increased without extending the measurement time. (Thomas, A Beginner's Guide to ICP-MS: Part X - Detectors , 2002)

3 Experimental details

The following chapter has been organized into four main sections to address the research question concerning the catalytic performance of cobalt-based spinel oxides in isopropanol oxidation, with each section to be discussed in greater detail in the subsequent chapters.

3.1 Equipment

Table 1: Utilized equipment

Application	Device identification	
	Name/Model No.	Manufacturer
N_2-physisorption	ASAP 2020	Micromeritics
Temperature programmed reduction	BELCAT II	Microtrac
X-ray diffraction method	PW3040/60 X'Pert PRO	PHILIPS
Mass spectrometer	OmniStar	PFEIFFER Vacuum + Fab Solutions
Oxygen mass flow controller	0154/-C1A1	BROOKS INSTRUMENT
Isopropanol water bath heating element	DC30 K20	Thermo Scientific
Argon mass flow controller	247D	MKS Instruments

3.2 Synthesis of cobalt-based oxide nanoparticles

Cobalt-based oxide nanoparticles were synthesized via coprecipitation and combustion methods using different stoichiometric ratios. The resulting samples were then calcined at various temperatures for one hour. The synthesis and calcination parameters, along with their corresponding nomenclature, are summarized in Table 2. The calcination heating rate was approximately 10°C/min, with a gradual reduction as the target temperature was approached. The calcination duration was initiated once the temperature stabilized near the desired value.

The coprecipitation method was applied uniformly across all synthesised catalysts. Initially, the stoichiometric amount of the metal nitrate (poly)hydrates ($Me(NO_3)_2 \cdot xH_2O$) was dissolved in 100 mL of deionized water in a 500 mL beaker. To the solution was then slowly 1 M sodium hydroxide added until the pH reached approximately 14, leading to the formation of a precipitate. This precipitate was transferred to two Falcon vials and centrifuged at 4500 rpm (3260 xg) for 5 minutes. The supernatant was carefully decanted, and the vials were refilled with deionized water, followed by additional centrifugation and decanting.

The remaining precipitate was resuspended in 40 mL of deionized water, using a spatula and vigorous shaking. Since the pH of the supernatant remained above 7, the washing process was repeated twice more, adding deionized water each time and centrifuging for 40 minutes. Once the pH stabilized between 7 and 8, the supernatant was discarded, and the solid was transferred to a sintered crucible. The material was then dried overnight at 100°C in a drying oven. The entire procedure is illustrated in Figure 4. A small sample of the coprecipitation product was withdrawn for characterization.

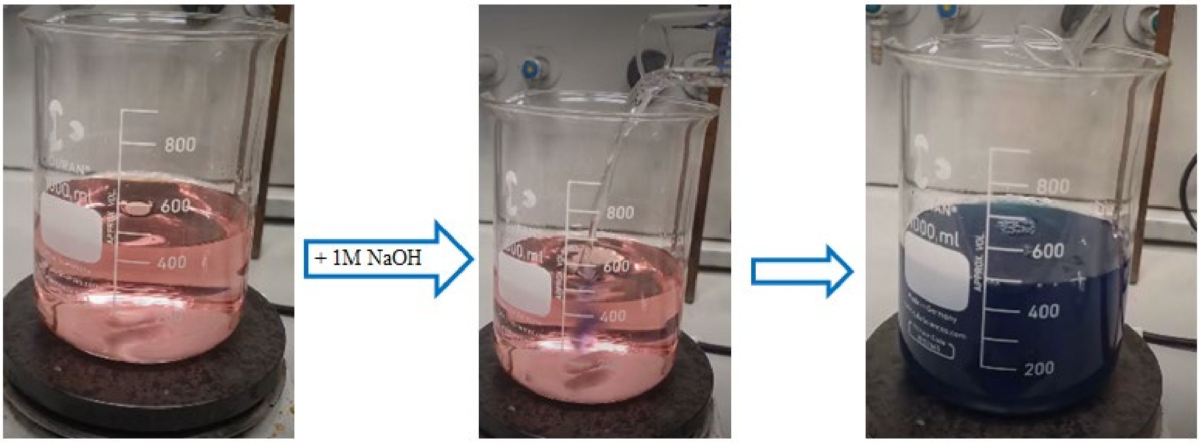

Figure 4: Coprecipitation of cobalt nitrate

The combustion synthesis of various cobalt-based oxides was carried out by preparing an aqueous solution of metal nitrates in a stoichiometric ratio corresponding to the desired metal composition. Glycine was used as the fuel in the process. The amount of precursor salts was calculated to yield three grams of the desired oxide if full selectivity was reached. The calculations were performed using the following equation:

$$aA(NO_3)_x * yH_2O + bB(NO_3)_w * zH_2O + nG \rightarrow A_aB_bO_4 + gases$$

Since the synthesis aimed solely at producing spinels, the sum of parameters a and b was always constrained to be equal to three. The amount of glycine, expressed as glycine equivalents n (the ratio of moles of glycine to the expected moles of spinel oxide), is typically considered non-essential as it mainly facilitates combustion. However, its role has been subject to debate. It was discussed that glycine not only acts as a fuel in the combustion reaction but also as a reducing agent, reducing both nitrate and metal ions. This suggests that the presence of different oxide phases, characterized by varying oxidation states of the metal ions, is influenced by n. Therefore, n can serve as a tuning parameter to control the combustion process, thus influencing the properties of the resulting metal oxides, including their morphology and specific surface area. For the catalysts tested in this study, three glycine equivalents ($3G$) were used. (X. Wang, 2017)

The solution was transferred to a 1-liter Duran beaker with a stir bar and placed on a heated magnetic stirrer under a fume hood. The solution was stirred until complete dissolution of the components. Subsequently, heating was initiated at maximum, and the fume hood was closed. The system was maintained under continuous heating and stirring. Within minutes, water began to evaporate, and the solution transformed into a viscous, gelatinous substance. After approximately 10 minutes, a Büchner funnel was inverted and placed above the beaker to prevent the ejection of materials. Once the water had evaporated, approximately 15 minutes after heating commenced, a violent combustion reaction occurred, propagating throughout the beaker. After most of the heat had dissipated, the funnel was carefully removed, and the beaker was tilted to ensure the reaction front reached the entire system. The reaction product appeared as a dark solid (usually black, sometimes brownish). Most of the powder remained in the beaker, both at the bottom and on the walls, but a significant amount was captured by the funnel, while some product escaped into the fume hood. To avoid contamination, this fraction, consisting of low particle size material unsuitable for continuous flow catalytic tests, was discarded. A small sample of the combustion product was taken for characterization, while the rest was submitted to calcination and the beaker was washed thoroughly, allowing for reuse.

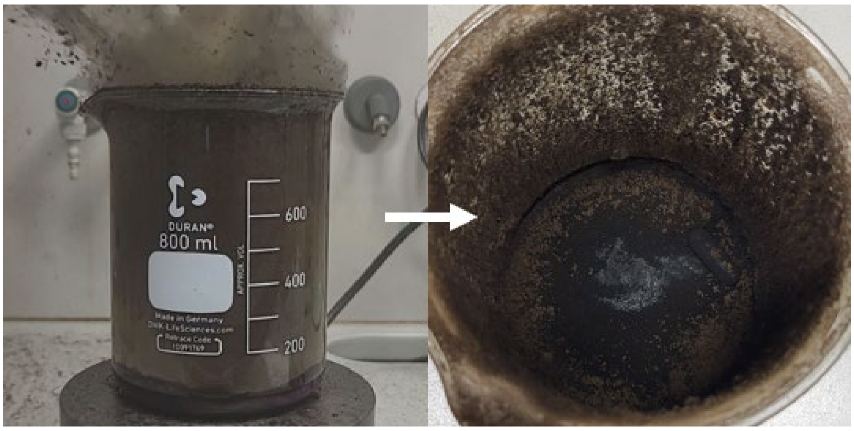

Figure 5: Combustion of Co_3O_4 without Büchner funnel

Table 2:List of synthesised catalysts.

code	metal ratio	composition (XRD)	composition (XRD) after calcination	preparation process	drying temp.	calcination temp.(+code addition) [1h]
1	Co	CoO_2 (1)	Co_3O_4 (1A)	coprecipitation (CPT) in water	100 °C over night	400°C (A)
2	2/3 Mn + 1/3 Co	$MnCo_2O_4$ (2)	$MnCo_2O_4$ (2A)	CPT in water	100 °C over night	400°C (A)
3	5/6 Co + 1/6 Mn	$MnCo_2O_4$ (3)	$MnCo_2O_4$ (3A)	CPT in water	100 °C over night	400°C (A)
4.1	1Ni + 2Fe	Fe_2O_3 + NiO		CPT in water	300 °C for 1 h	
4.2	1Ni + 2Fe	Fe_2O_3 + NiO		CPT in water	400 °C for 1 h	
5	1Ni + 2Fe		$NiFe_2O_4$ + Fe_2O_3 (5A)	direct decomposition in water	100 °C for 3 h	400°C (A)
6	1Ni + 2Fe	$NiFe_2O_4$ + residual Fe_2O_3		DD in ethanol	100 °C for 1:10 h	800°C (B)
7	1Ni + 2Fe			DD in ethanol	roomtemp. over weekend	950°C (C)
comb 1 (C1)	Co_3O_4			combustion		
comb 2 (C2)	Co_3O_4			combustion		300°C (no code, but A)
comb 3 (C3)	Co_3O_4	CoO_2	Co_3O_4	combustion		300°C (A)

As shown in Table 2, three of the coprecipitation processes (samples 5, 6 and 7) were performed using a modified method. In these cases, the required nitrates were fully dissolved in 10 mL of water or ethanol within a ceramic crucible and subsequently dried under the conditions outlined in the table. Notably, sample 7 was not completely dry before proceeding to the calcination step. The drying process was regularly monitored, but no further progress was observed at a certain point, leading to the decision to terminate drying and continue with calcination.

The objective of this synthesis approach was to produce nickel ferrite oxide in its purest form, free from any residual byproducts. However, due to the challenges associated with achieving complete drying and the superior catalytic performance observed in other samples, this synthesis method was not pursued further

3.3 Characterization of the cobalt-based oxides

The following characterization techniques were employed: Temperature-Programmed Reduction (TPR), N_2-physisorption with analysis according to the Brunauer-Emmett-Teller (BET) method, and X-ray Diffraction (XRD). However, not all characterization methods were applied to all the samples listed in Table 2, as only those demonstrating promising catalytic performance were further analysed.

After completing all characterization steps, the catalyst was subjected to reaction testing. Following the reaction (as described in chapter 3.4), the recovered catalyst was analysed using X-ray diffraction (XRD) to determine whether any structural properties had undergone changes.

3.3.1 Temperature-programmed reduction (TPR)

Temperature-Programmed Reduction (TPR) with hydrogen is a widely applied method for characterizing reducible solids and catalytic materials. In this technique, the sample, typically a reducible catalyst or catalyst precursor is subjected to a flow of a reducing gas mixture, often composed of a few volume percent hydrogen in an inert carrier gas, while the temperature is ramped linearly. The reduction process is monitored in real time by analysing the hydrogen concentration in the gas stream exiting the reactor. This allows the quantification of the total hydrogen consumption, enabling the calculation of the degree of reduction and the average oxidation state of the material post-reduction. (M. A. Reiche, 2000) The objective of this analysis was to evaluate the reducibility and performance differences among the synthesized catalysts.

Table 3: TPR pretreatment program

Step	Time (min)	Target (°C)	MFC3 Gas	MFC3 (mL/min)	MFC2 Gas	MFC2 (mL/min)
1	37	400	Argon	40	Oxygen	10
2	30	400	Argon	40	Oxygen	10
3	30	50	Argon	40	Oxygen	10
4	30	50	Argon	50	Oxygen	0

Table 4: H2-TPR program parameters

Time for detector stabilization (min)	30
Target temperature (°C)	800
Ramp rate (°C/min)	5
Target temperature holding time (min)	0
Carrier Gas MFC1	Argon
Flow MFC1 (sccm)	45
Carrier Gas MFC2	Hydrogen
Flow MFC2 (sscm)	5

3.3.2 N_2-physisorption by BET

Nitrogen physisorption, or nitrogen adsorption, is a widely employed technique in materials science for assessing the textural properties of porous materials. The specific surface area is commonly quantified using the Brunauer-Emmett-Teller (BET) method.

The BET surface area analysis, named after Stephen Brunauer, Paul Hugh Emmett, and Edward Teller, is the most widely accepted method for determining the specific surface area of materials. This technique, introduced in their seminal 1938 work, builds on Langmuir's adsorption model from 1918 by extending it to multilayer adsorption. The BET method links adsorption behavior to material properties such as total surface area, pore size distribution, micropore analysis, and porosity.

The accuracy of BET analysis depends on the validity of several assumptions:

Homogeneous surface: The surface of the material is assumed to be uniform, with adsorption occurring equally across all sites without preferential sorption. Each site can hold at most one molecule, and the total adsorption is expressed as fractional surface coverage.

Limited molecular interactions: Adsorbed molecules act as potential sites for further adsorption, forming multilayers. Interactions between adsorbed molecules, between gas-phase molecules, or nonsorptive interactions are neglected.

Local equilibrium: At equilibrium, the rate of adsorption equals the rate of desorption, ensuring no net change in adsorbed molecules at a given vapor pressure. This assumes a saturated system where each layer is in balance with the gas phase.

Kinetics and energetics: Adsorption is kinetically controlled, requiring energy for surface adsorption equivalent to the heat of adsorption. Subsequent layers behave as condensed liquid, needing energy equivalent to the heat of condensation. These energy requirements are uniform across the material.

Saturation and multilayer formation: At the saturation pressure (p_0), the material is assumed to be fully covered by a condensed liquid-phase adsorbate, signifying infinite adsorption layers.

Understanding these assumptions is essential for interpreting BET-derived data reliably and applying it to characterize material properties with confidence. (J. Brame, 2016)

Table 5: BET program parameters

Evacuation Phase		Heating Phase	
Temperature ramp rate (°C/min)	10	Ramp rate (°C/min)	10
Target temperature (°C)	90	Hold temperature (°C)	200
Evacuation rate (mbar/s)	6.7	Hold time (min)	360
Unrestricted evac. from (mbar)	6.7	Hold pressure (mbar)	133
Vacuum setpoint (µbar)	13		
Evacuation time (min)	60		

3.3.3 X-Ray diffraction method (XRD)

X-ray diffraction (XRD) is a non-destructive analytical technique widely utilized to study the structural, crystallographic, and phase-related properties of materials. The method is based on the diffraction of X-rays by the periodic atomic lattice in crystalline materials. When an X-ray beam interacts with a crystal, the scattering of the beam is governed by Bragg's Law, $n\lambda=2d\sin\theta$, where λ is the wavelength of the X-rays, d is the interplanar spacing, θ is the diffraction angle, and n represents the order of reflection. This relationship underpins the analysis of the diffraction pattern, allowing for the determination of atomic arrangements and lattice structures.

The technique is particularly effective for identifying crystalline phases, quantifying phase fractions, determining lattice parameters, and analysing microstructural features such as crystallite size, strain, and defects. These properties are critical in various fields, including materials science, geology, chemistry, and engineering. Advanced analysis methods, such as Rietveld refinement, enable the extraction of precise structural information, even for complex mixtures or distorted lattices. (Y. Waseda, 2011)

XRD can be performed using different methods, depending on the type of sample and the desired information:

Powder diffraction: Commonly used for polycrystalline samples, this technique produces diffraction rings due to the random orientation of microcrystals. The diffraction pattern is recorded as intensity peaks versus the diffraction angle (2θ), providing insights into phase composition and crystal structure.

Single-crystal diffraction: This method determines the precise three-dimensional arrangement of atoms in single crystals. It is widely used in the characterization of minerals, pharmaceuticals, and novel materials.

Laue method: This technique is used to study single crystals and is particularly suited for analysing crystal orientation and detecting defects.

Grazing incidence XRD (GIXRD): Applied to thin films and surface layers, this method enhances sensitivity to surface features by using a shallow incident angle.

High-resolution XRD (HRXRD): Used for semiconductor materials and epitaxial films, HRXRD provides detailed information about strain, layer thickness, and composition in multilayer structures. (Warren, 1941)

An XRD setup typically consists of an X-ray source (commonly Cu-Kα radiation), a sample holder, and a detector to record the diffracted beams. Modern XRD systems often incorporate rotating anodes, monochromators, and advanced detectors, improving data resolution and reducing noise. Computational tools play a crucial role in analysing diffraction data, enabling phase identification through database comparisons (e.g., ICDD or COD databases) and refining structural models.

XRD is highly versatile and widely applicable for crystalline materials. It offers non-destructive characterization and rapid phase identification, making it ideal for quality control and research. However, it has limitations, particularly with amorphous materials, which lack the long-range periodicity required for distinct diffraction peaks. Additionally, the technique is less sensitive to light elements unless specific instrumentation is used. (Y. Waseda, 2011)

The data analysis was performed using the HighScore Plus program in conjunction with the PANalytical database (see Figure 54 and Figure 55).

3.4 Catalytic performance of cobalt-based oxides

To obtain the necessary data for this thesis, a packed bed reactor setup was designed using a quartz tube with a length of 33.5 cm and an inner diameter of 4.5 mm. The catalyst was positioned 14 cm from the bottom of the tube, securely held in place between two quartz wool plugs. A thermocouple was inserted 17 cm into the reactor tube to monitor the internal temperature. For external heating, the reactor tube was placed within a heating mantle. Furthermore a mass spectrometer was used to analyse the reaction gases. A schematic representation of the setup is provided in Figure 6, while Figure 7 shows an actual photograph of the setup during operation.

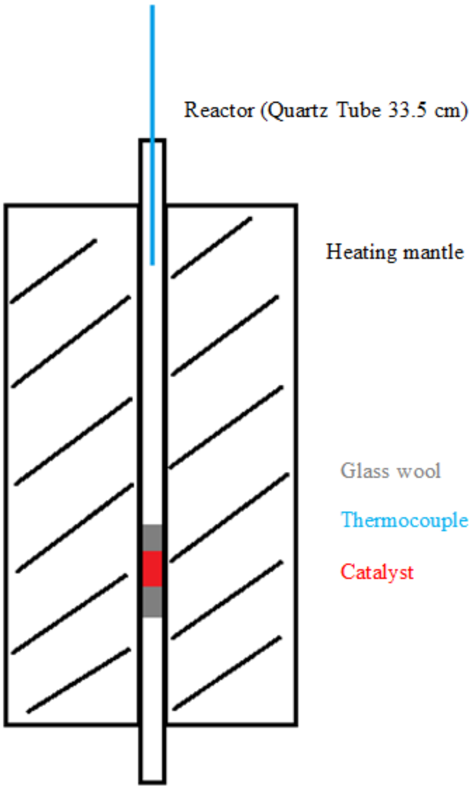

Figure 6: Schematic image of the reactor and oven

Figure 7: Reactor and oven

For the reaction process, a pretreatment step was performed to eliminate surface species that might reduce the activity of the catalyst and/or produce molecules that could be mistakenly attributed to the reaction. The pretreatment involved exposing the sample to a flow of synthetic air (80% argon, 20% oxygen) at 50 mL/min. Initially, the sample was flushed at 50°C for approximately one hour to stabilize the gas flow and ensure the synthetic air composition was constant. The temperature was then ramped up at a rate of 10°C/min to 250°C, where it was maintained for 30 minutes.

After the pretreatment, the sample was externally cooled to below 50°C, at which point the desired reaction gas flow was introduced as specified in

Table 7. While MFCs were used to regulate the oxygen and argon gas flows, for the isopropanol flow a saturator was placed in a heated (32°C) water bath and argon was passed through until a total isopropanol flow of 1.8 mL/min was achieved. The reaction was held at 50°C for one hour before heating to the target reaction temperature. During this phase, only the reaction-specific parameters were adjusted, which included the oxygen-to-isopropanol ratio, reaction temperature, duration, heating rate, and the number of reaction cycles. Following the completion of the reaction, the system was allowed to cool automatically via the programmed temperature profile.

A modified protocol was applied to sample 17 (Table 7). While the pretreatment followed the same procedure, the sample was manually cooled after the first reaction cycle to quickly reach room temperature. Once the target temperature was achieved, the sample was exposed to synthetic air at 50°C overnight. The next day, the reaction was repeated under identical conditions to the previous day, including the pretreatment using the same catalyst without any further modifications.

The reactants and resulting products were analysed utilizing a gas analyser equipped with mass spectrometry. The reaction profiles were obtained using the m/z signals corresponding to 2 (H_2), 18 (H_2O), 32 (O_2), 40 (Ar), 44 (CO_2), 45 (isopropanol) and 58 (acetone). The m/z ratio for isopropanol (45) was selected due to its higher reliability, as it exhibits fewer overlaps with other fragments and signals. Furthermore, all the specified m/z-ratios were normalized by dividing their respective signals by the corresponding argon signal.

To quantify the detected signals calibration curves were generated by measuring known concentrations and plotting them against the corresponding signal intensities. A reliable quantification of water using mass spectrometry is challenging due to the reason that water has a high tendency to adsorb onto surfaces within the reactor, associated sampling lines and mass spectrometer, leading to inconsistent signal intensities. Additionally, water's ubiquitous presence in the environment as moisture can cause background interference, further complicating accurate calibration. The following formulas were employed for the calculation of yield, conversion, efficiency and selectivity:

- **Yield (%):**

$$\frac{concentration_{product}\left(\frac{mmol}{\mathrm{min}}\right)}{initial\ concentration_{isopropanol}\left(\frac{mmol}{min}\right)} * 100$$

- **Conversion (%):**

$$\frac{initial\ concentration_{reactant}\left(\frac{mmol}{min}\right) - concentration_{reactant}\left(\frac{mmol}{min}\right)}{initial\ concentration_{reactant}\left(\frac{mmol}{min}\right)} * 100$$

- **Efficiency (%):**

$$\frac{initial\ concentration_{isopropanol}\left(\frac{mmol}{min}\right) - concentration_{isopropanol}\left(\frac{mmol}{min}\right)}{2 * \left(initial\ concentration_{oxygen}\left(\frac{mmol}{min}\right) - concentration_{oxygen}\left(\frac{mmol}{min}\right)\right)} * 100$$

- **Selectivity (%):**

$$\frac{yield_{product}\ (\%)}{conversion_{isopropanol}\ (\%)} * 100$$

Table 6: List of used catalysts

Nr.	Sample	Composition	Calcination temp.	Weight [mg]
1	PG443	Co_3O_4	200	20.80
2	PG443	Co_3O_4	200	20.40
3	PG444	Co_3O_4	500	20.40
4	PG444	Co_3O_4	500	20.40
5	PG613	$CrCo_2O_4$	500	20.60
6	PG617	$NiCo_2O_4$	500	20.10
7	PG619	$CuCo_2O_4$	500	20.20
8	PG620	$ZnCo_2O_4$	500	20.00
9	PG621	Co_3O_4	500	20.30
10	PG614	$MnCo_2O_4$	500	20.30
11	C3A	Co_3O_4	300	20.30
12	C3A	Co_3O_4	300	20.00
13	C3A	Co_3O_4	300	20.40
14	1A (cop)	Co_3O_4	400	20.00
15	C3A	Co_3O_4	300	20.30
16	C3A	Co_3O_4	300	20.00
17	C3A	Co_3O_4	300	20.80
18	C3A	Co_3O_4	300	20.40

Table 7: Reaction parameters

Nr.	sample	IPA/O_2	O_2 [mL/min]	IPA [mL/min]	Argon [mL/min]	T_{max} reaction [°C]	reaction at T_{max} [hrs]	heating rate [°C/min]	cycles
1	PG443	1:1	1.8	1.8	46.4	400	0.5	2	2
2	PG443	2:1	0.9	1.8	47.3	400	0.5	2	2
3	PG444	1:1	1.8	1.8	46.6	400	0.5	2	2
4	PG444	2:1	0.9	1.8	47.3	400	0.5	2	2
5	PG613	1:1	1.8	1.8	46.6	400	0.5	10	2
6	PG617	1:1	1.8	1.8	46.6	400	0.5	10	2
7	PG619	1:1	1.8	1.8	46.6	400	0.5	10	2
8	PG620	1:1	1.8	1.8	46.6	400	0.5	10	2
9	PG621	1:1	1.8	1.8	46.6	400	0.5	2	2
10	PG614	1:1	1.8	1.8	46.6	400	0.5	2	2
11	C3A	2:1	0.9	1.8	47.3	400	0.5	2	1
12	C3A	2:1	0.9	1.8	47.3	200	0.5	2	1
13	C3A	2:1	0.9	1.8	47.3	200	8		1
14	1A (CPR)	1:1	1.8	1.8	46.6	400	0.5	2	2
15	C3A	2:1	0.9	1.8	47.3	200	4	2	2
16	C3A	2:1	0.9	1.8	47.3	400	10	2	1
17	C3A	2:1	0.9	1.8	47.3	200	2	2	2
18	C3A	2:1	0.9	1.8	47.3	100, 200, 300, 400	0.5	2	4

4 Analysis and results

This chapter aims to present and analyze the collected data by structuring the subchapters according to the tested catalysts, including their characterizations and reactions. At the conclusion of the chapter, the obtained results will be compared and discussed in detail.

Unless explicitly stated otherwise, the experimental parameters used for the tests correspond to those previously described in the relevant chapters and/or tables.

4.1 Co_3O_4 by combustion (C3A)

4.1.1 N_2-physisorption

Figure 8 illustrates the hysteresis loop observed for the Co_3O_4 catalyst synthesized via combustion. Additionally, a BET surface area of 19.7 m^2/g was determined.

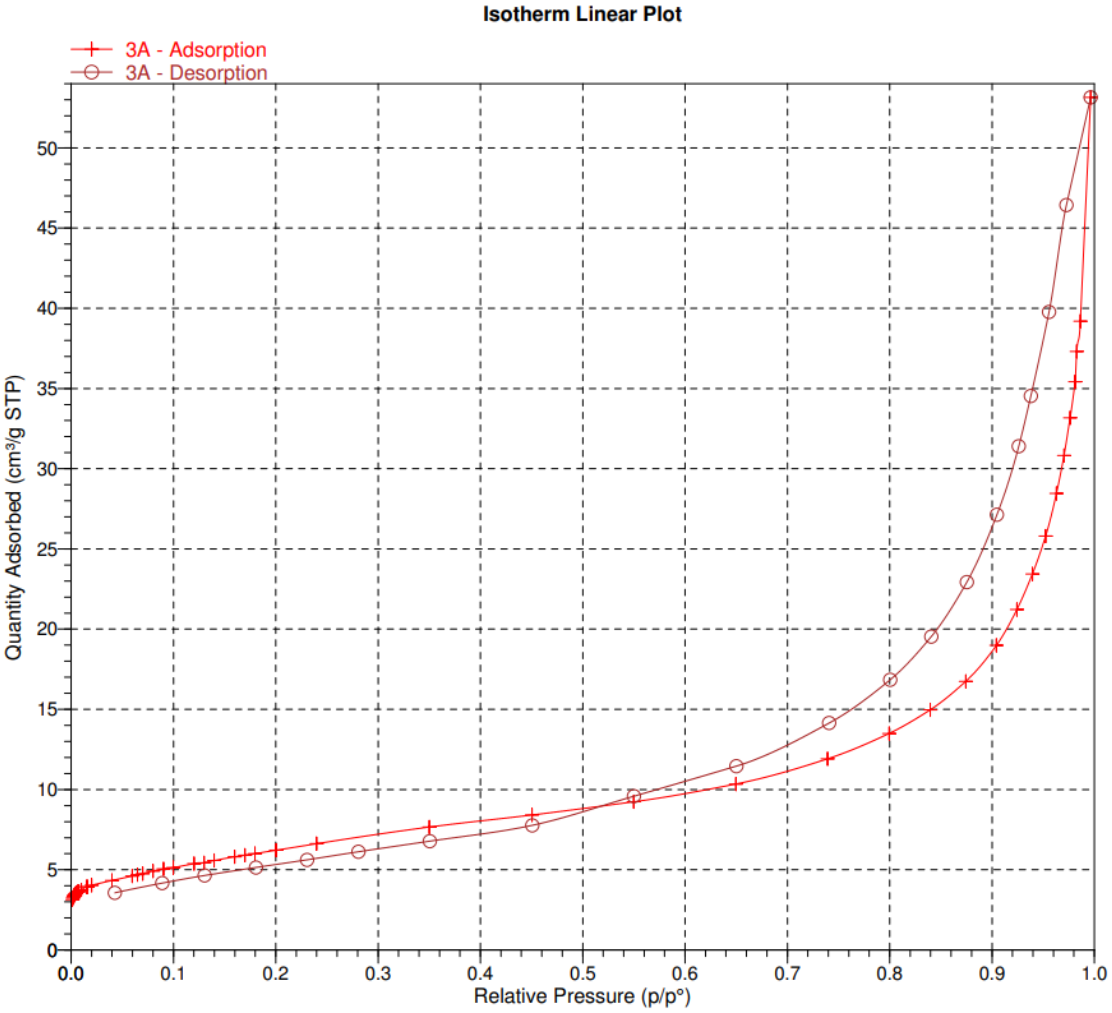

Figure 8: N_2 adsorption results for the C3A catalyst

The adsorption curve exhibits strong similarities to a Type III isotherm, primarily due to the absence of a distinct plateau at low relative pressures (p/p_0) and the overall shape of the isotherm. In Type III isotherms, weak adsorption at low relative pressures suggests limited interaction between the adsorbate and the surface, which aligns with the gradual increase in adsorption observed in the plot, indicating an absence of pronounced monolayer formation. The continuous and accelerated rise in adsorption at higher relative pressures ($p/p_0 > 0.8$), coupled with the lack of clear multilayer formation in the intermediate range ($p/p_0 = 0.2–0.6$), further supports the classification as a Type III isotherm. This is typically associated with non-porous or macroporous materials where adsorbate-adsorbate interactions predominate.

Consequently, the material likely exhibits relatively low adsorbate-surface interactions, consistent with the moderate BET surface area of 19.7 m²/g. This interpretation suggests that the Co_3O_4 catalyst has limited microporosity with weak interactions between the adsorbate and the pore walls. (M. Thommes, 2015)

4.1.2 TPR

The following figure illustrates the reduction behaviour of Co_3O_4, synthesized via combustion, during a reduction reaction with hydrogen as the reducing agent under increasing temperature. The x-axis represents the temperature, while the y-axis denotes the signal intensity, which is proportional to the amount of hydrogen consumed during the reduction process.

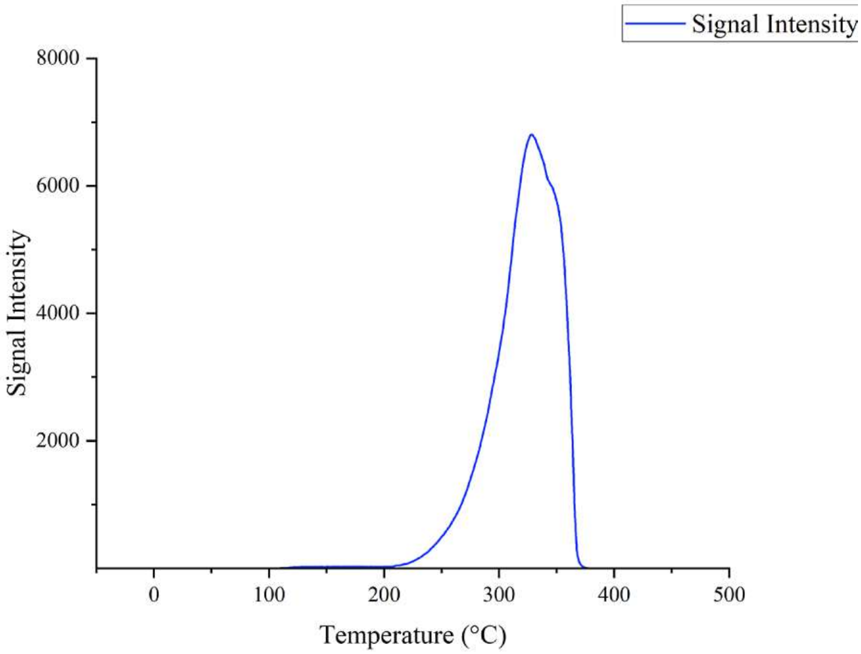

Figure 9: Temperature programmed reduction of Co_3O_4 (C3A)

The reduction process was anticipated to occur in two distinct steps: the reduction of cobalt (III) oxide (Co_3O_4) to cobalt (II) oxide (CoO) at approximately 260°C, followed by further reduction to metallic cobalt (Co) at 320°C. (Y. Wang, 2019) The latter reduction could take place immediately after the former, resulting in the observation of a single peak.

Reduction begins at approximately 200°C, suggesting that the material exhibits reduction at relatively low temperatures. The main reduction peak occurs between 300–350°C, with the lack of multiple distinct peaks indicating an overlap of peaks. This reduction behaviour is likely influenced by the physical properties of the sample, such as its surface area, crystallinity, or particle size. (P. H. Silva, 2020)

4.1.3 XRD

The X-ray diffraction (XRD) measurement shown in the provided Figure 10 represents the analysis of cobalt oxide (Co_3O_4) prepared via the combustion synthesis process and after the calcination for an hour at 300°C.

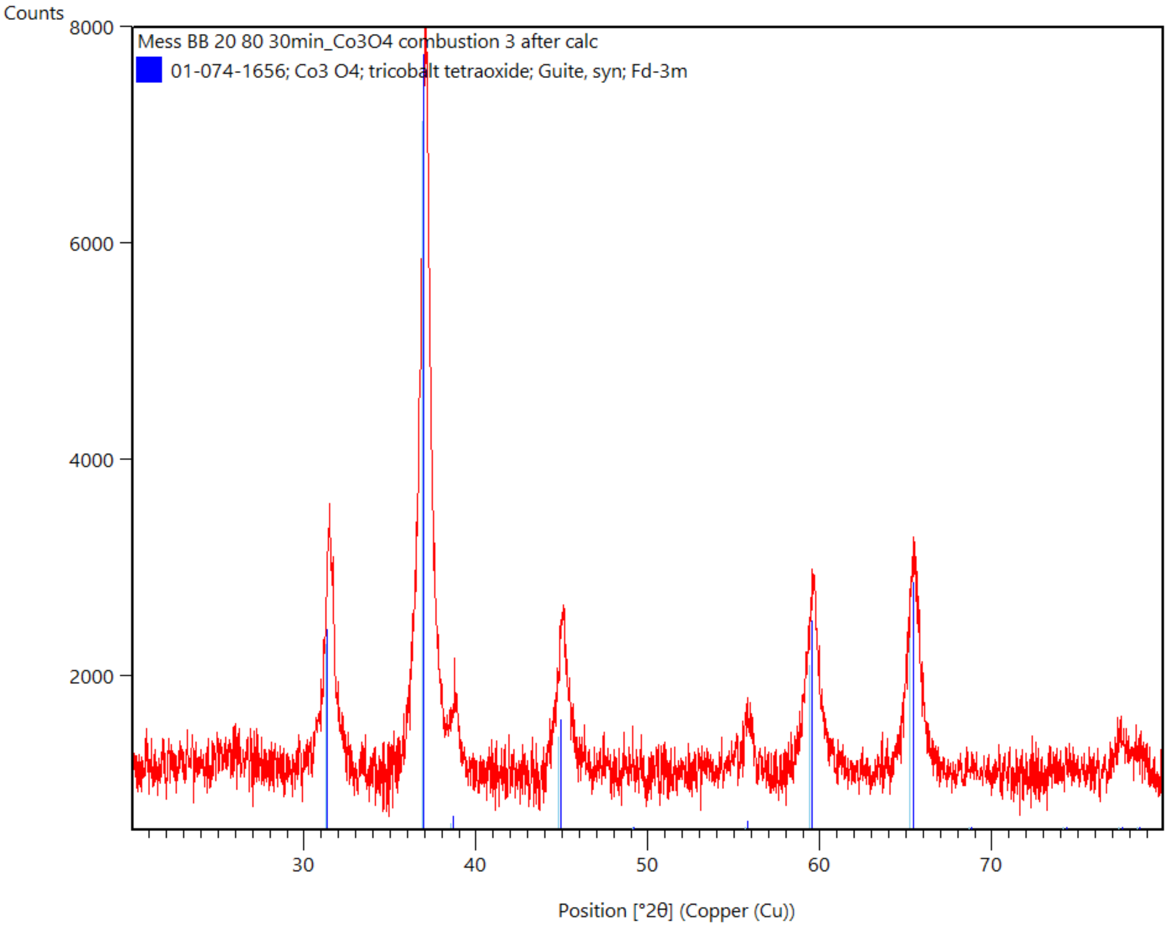

Figure 10: XRD of combustion Co_3O_4 after calcination (300°C)

The red diffraction pattern represents the XRD measurement of the synthesized sample and is compared to the reference pattern for cobalt (II,III) oxide (Co_3O_4), displayed in blue. Co_3O_4 exhibits a cubic spinel structure with the space group $Fd\bar{3}m$.

The alignment of the experimental peaks with the reference pattern confirms the successful synthesis of phase-pure Co_3O_4. The absence of any additional peaks indicates negligible or no contamination from secondary phases.

The primary diffraction peaks observed at characteristic 2θ positions, such as approximately 31°, 37°, 44°, 59°, and 65°, correspond to the (220), (311), (400), (511), and (440) crystal planes of Co_3O_4. The sharpness and intensity of these peaks are indicative of good crystallinity in the synthesized material. (Suresh, 2017)

This measurement was performed following a combustion synthesis process, a widely used method for rapid and energy-efficient material production. The results demonstrate that this approach successfully yielded Co_3O_4 with the expected structural properties.

In summary, the XRD analysis confirms the formation of cobalt(II,III) oxide (Co_3O_4) with excellent phase purity and crystallinity achieved through combustion synthesis. Further quantitative evaluation of peak broadening and intensity could offer deeper insights into crystallite size and lattice strain.

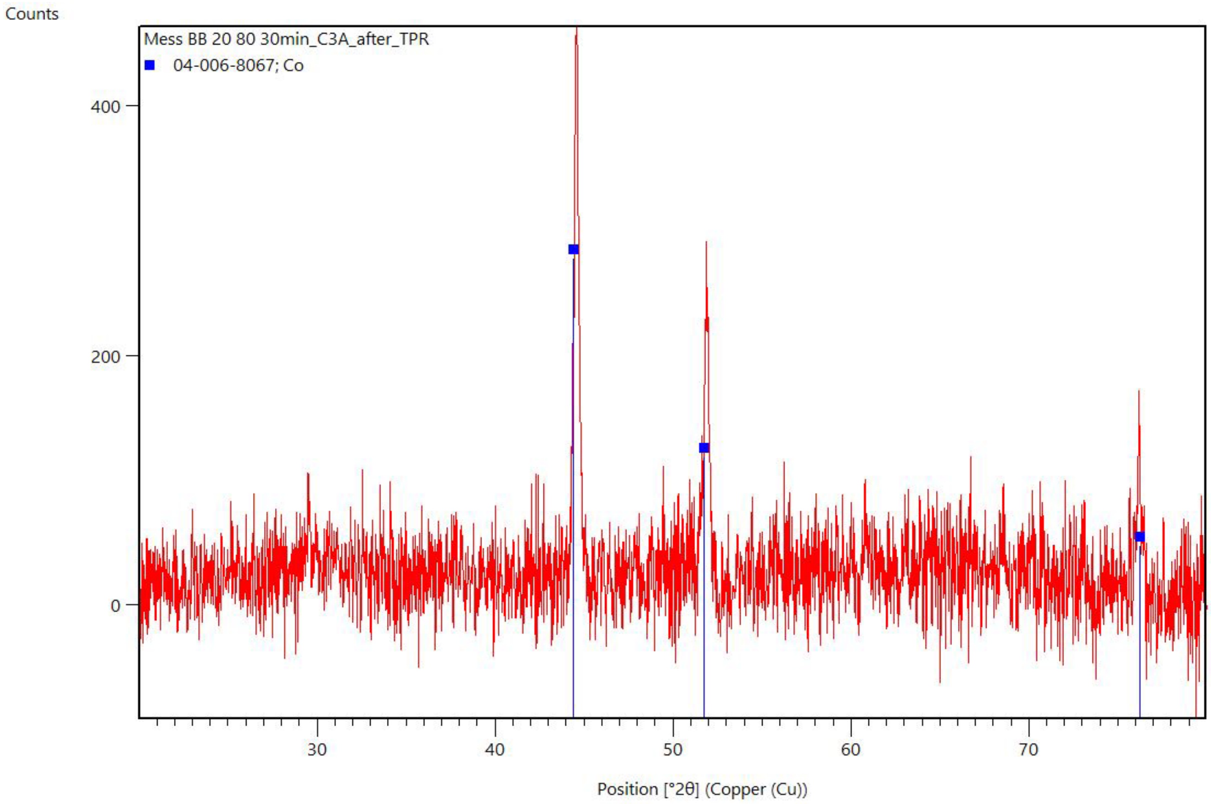

Figure 11: XRD of C3A after TPR

Figure 11 presents the XRD pattern of Co_3O_4 prepared via combustion synthesis and subsequently calcined at 300°C, following its TPR measurement. The diffraction peaks observed at approximately 44.2°, 51.5°, and 75.8° (2θ) are characteristic of metallic cobalt (Co) in its cubic phase, as corroborated by the reference pattern indicated in blue.

The absence of peaks corresponding to Co_3O_4 (e.g., ~36.8°, ~42.4°, ~61.4°) provides strong evidence that the Co_3O_4 phase has been fully reduced during TPR. Additionally, the lack of other significant peaks suggests that the material is a single-phase system rather than a mixture of Co_3O_4, CoO, and metallic Co.

This analysis supports the conclusion that the reduction process resulted in the complete transformation of Co_3O_4 to metallic cobalt, with no detectable oxide-related phases remaining.

4.1.4 Reaction 2:1 (IPA:Oxygen) at 400°C for 30 min

Figure 12 illustrates the catalytic performance of the Co_3O_4 catalyst during the reaction at 400°C for 30 minutes, using a 2:1 isopropanol-to-oxygen concentration ratio. Co_3O_4 is known to facilitate both oxidation and dehydrogenation of isopropanol.

Cobalt oxide (Co_3O_4), as an active oxidation catalyst, provides active sites for the adsorption and activation of isopropanol and oxygen. It is expected that at lower temperatures, the catalyst predominantly promotes the dehydrogenation of isopropanol to acetone. At higher temperatures, a shift toward complete oxidation occurs, where acetone and any unconverted isopropanol are oxidized further to CO_2 and water.

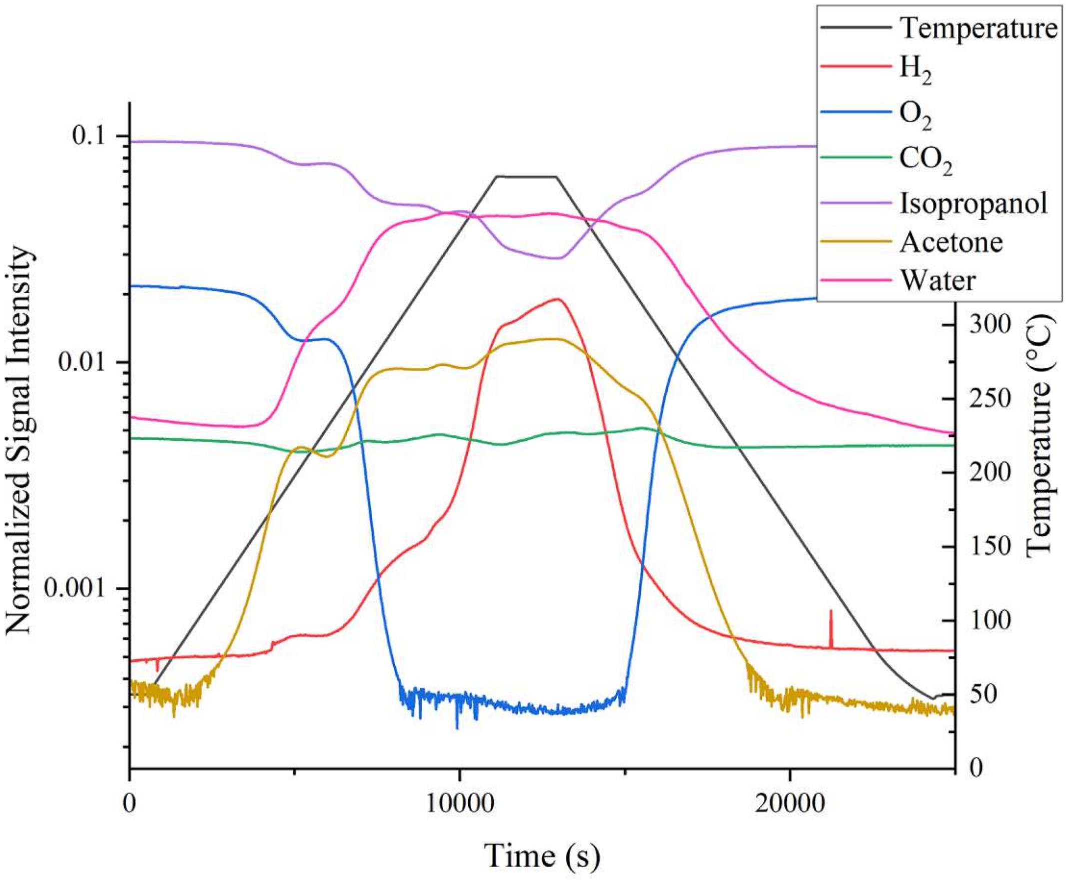

Figure 12: Reaction 2:1 (IPA:Oxygen) at 400°C for 30 min

The experimental data presented in Figure 12 aligns partially with these theoretical predictions. As the temperature increases, the acetone and hydrogen signal intensities rise, while the isopropanol and oxygen signals decrease. This behaviour is consistent with the dehydrogenation of isopropanol in the first step.

However, the absence of a significant increase in the CO_2 signal indicates that complete oxidation is minimal under the experimental conditions. This suggests that the conversion of isopropanol to acetone is highly efficient, with little to no further oxidation occurring. The data highlights the ability of the Co_3O_4 catalyst to selectively promote selective oxidation at the tested reaction conditions.

The reaction profile exhibits a shoulder at approximately 200°C, which could be a distinctive feature of this specific catalyst. Moreover, this observed shoulder has been previously noted in experiments conducted by other groups (T. Falk, 2022). This phenomenon will be further investigated and analyzed in the subsequent chapters.

Additionally, the selectivity and yield of the reactions will be thoroughly examined and discussed in Chapter 4.6.

4.1.5 Reaction 2:1 (IPA:Oxygen) at 200°C for 30 min

The following Figure 13 illustrates the catalytic oxidation of isopropanol over a Co_3O_4 catalyst, conducted at a constant temperature of 200°C for 30 minutes. Maintaining the temperature at 200°C allows for a detailed investigation of the previously observed shoulder in the reaction profile, enabling further analysis of its origin and significance.

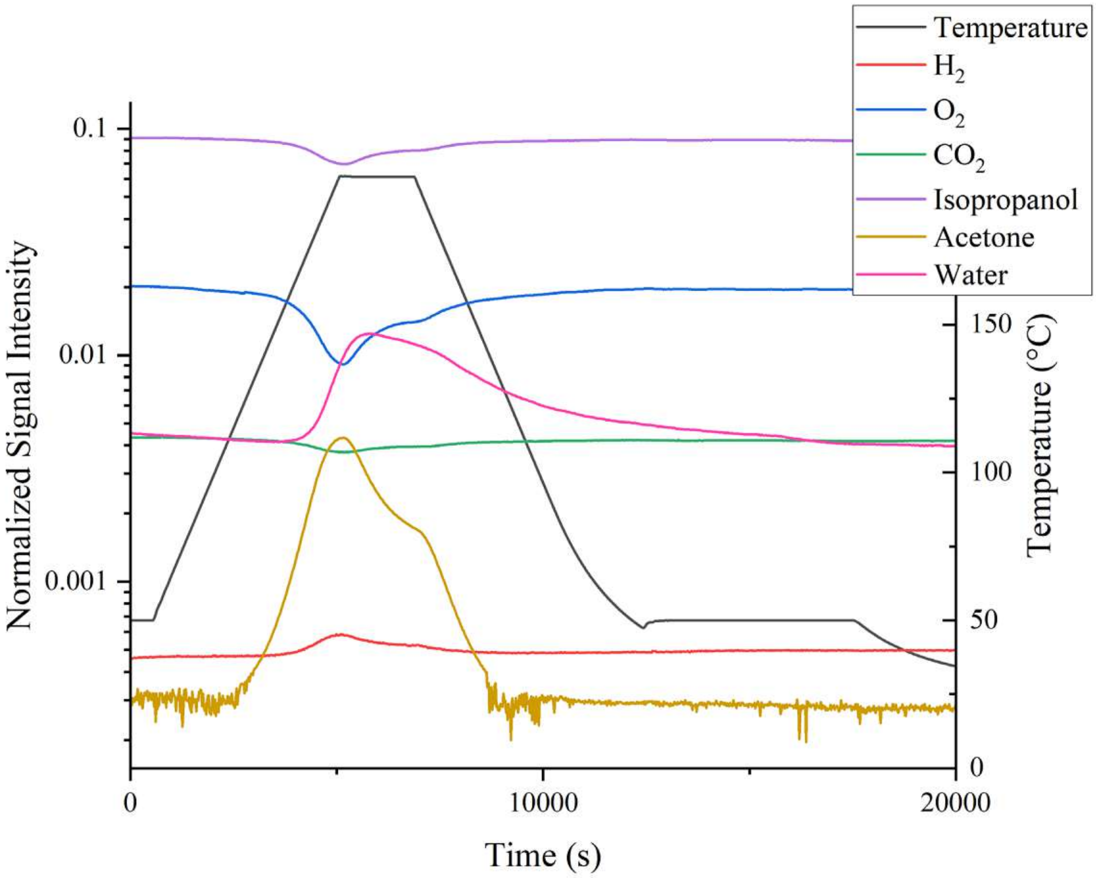

Figure 13: Reaction 2:1 (IPA:Oxygen) at 200°C for 30 min

At 200°C, the isopropanol signal exhibits a slight decrease, corresponding to the previously mentioned shoulder. The effectiveness of the selective oxidation of isopropanol to acetone is linked to the dehydrogenation process, as evidenced by the increase in the hydrogen signal. Although the hydrogen signal does rise, its change is less pronounced compared to that of acetone, suggesting that hydrogen evolution is consistent but modest under these conditions. Additionally, due to the low overall conversion, the oxygen concentration remains high, facilitating the combustion of hydrogen to water. At higher conversion levels, oxygen becomes depleted, leading to the accumulation of hydrogen.

A more significant change is observed in the oxygen signal, which decreases notably during the reaction. This decline indicates successful oxygen consumption as part of the oxidation process and supports the conclusion that selective oxidation to acetone is the dominant pathway at 200°C.

This analysis reinforces the temperature-dependent catalytic behaviour of Co_3O_4, with 200°C favoring selective selective oxidation of isopropanol to acetone. However, the overall catalytic activity remains lower compared to higher-temperature conditions, as evidenced by the limited changes in isopropanol and hydrogen signals and the absence of significant CO_2 production. Further analysis is required to quantify conversion efficiency, selectivity, and yield more precisely.

In summary, the data suggests that at 200°C, the Co_3O_4 catalyst demonstrates high selectivity for acetone production, with the observed shoulder potentially representing a transition phase or characteristic feature of the catalyst's performance at this temperature. Further investigations such as the XRD measurements were done to clarify the underlying mechanism and optimize reaction parameters for enhanced catalytic efficiency.

4.1.6 Reaction 2:1 (IPA:Oxygen) at 200°C for 8 hours

Figure 14 represents an extension of the previously conducted experiment, with the reaction time increased to eight hours. This extended timeframe allows for the identification and analysis of potential discrepancies, mechanisms, and effects that may not be apparent in shorter experiments.

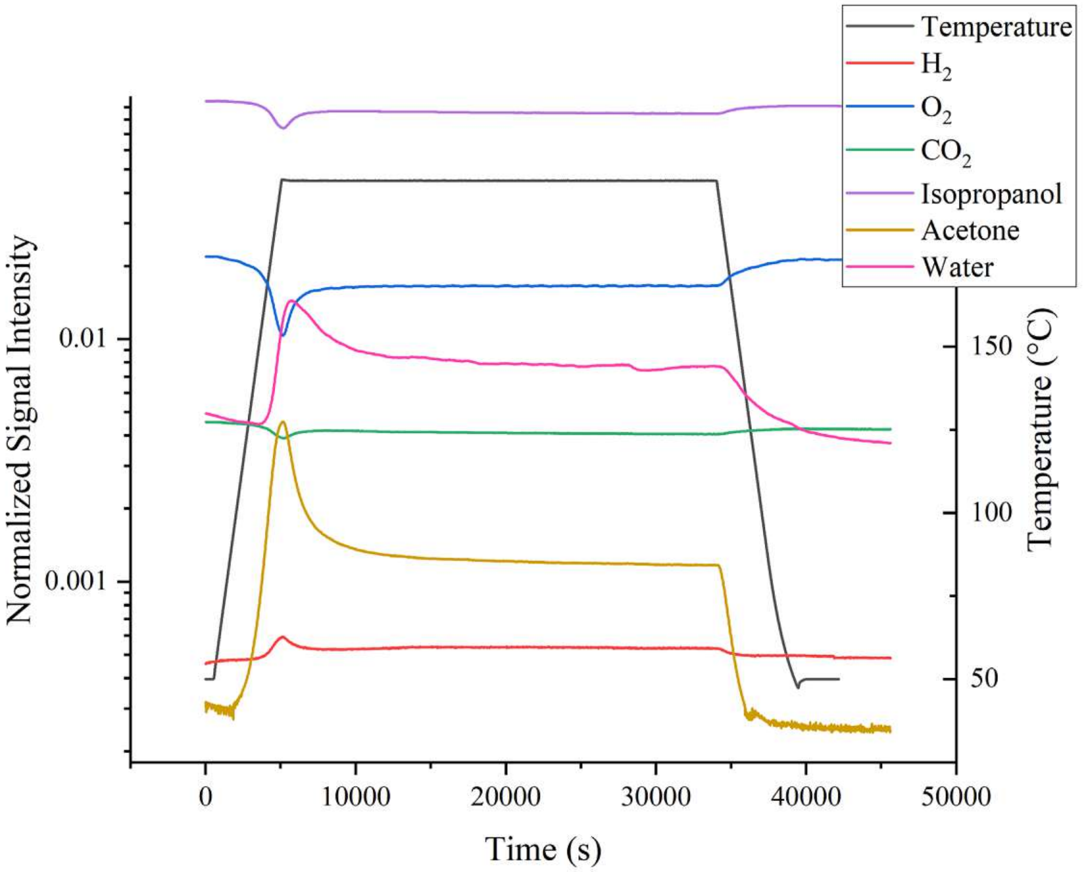

Figure 14: Reaction 2:1 (IPA:Oxygen) at 200°C for 8 hours

The prolonged reaction highlights that the shoulder observed in earlier experiments is a transient phenomenon, appearing only at the beginning of the reaction. As the reaction progresses, the acetone signal reaches its peak and then stabilizes, alongside the other signals, for the remainder of the reaction. This stabilization suggests a steady-state reaction regime, where the production of acetone and the consumption of isopropanol and oxygen proceed at consistent rates.

The data clearly demonstrates that the reaction achieves a stable operating state after the initial transient phase marked by the shoulder. The absence of further fluctuations in signal intensity suggests that the Co_3O_4 catalyst maintains its performance without deactivation or significant changes in activity during the extended reaction period. This behaviour is indicative of a robust catalytic system capable of sustaining long-term selective oxidation of isopropanol to acetone under the tested conditions.

Although the constant CO_2 signal might suggest that the reaction is highly selective under these conditions and that complete oxidation to CO_2 does not occur, it is unlikely that there is no variation in CO_2 production. This observation raises the possibility that an issue may have occurred with the signal detection.

4.1.7 Reaction 2:1 (IPA:Oxygen) two cycles at 200°C for 4 hours

Figure 15 illustrates an experiment conducted to further investigate the origin of the previously observed shoulder in the signal during the selective oxidation of isopropanol over the Co_3O_4 catalyst. This experiment involved two reaction cycles at 200°C, with each cycle maintaining the reaction temperature for four hours, separated by a cooling period of three hours.

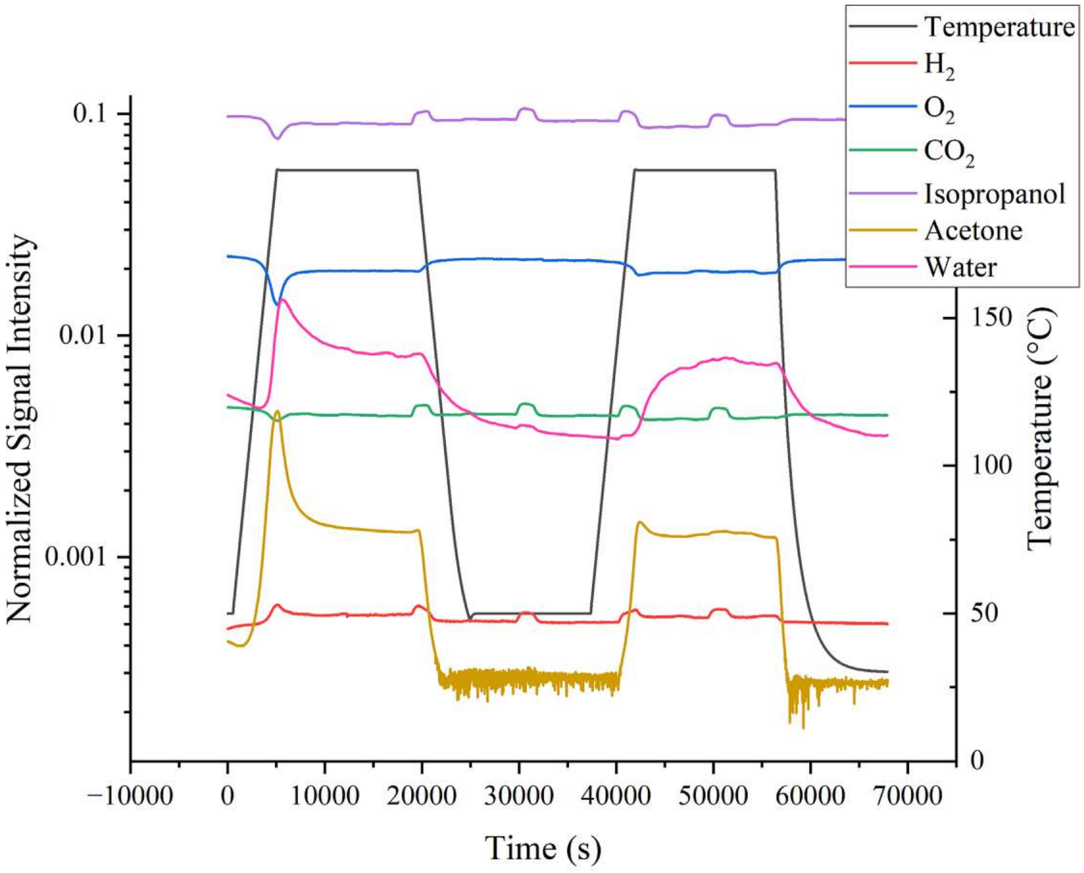

Figure 15: Reaction 2:1 (IPA:Oxygen) two cycles at 200°C for 4 hours

At the start of the first cycle, the characteristic shoulder in the acetone signal is observed once again, followed by stabilization of all signals after the initial transient phase. This behaviour aligns with previous experiments and suggests that the shoulder is an inherent feature of the catalytic process.

After the first cycle, the system was cooled, and the temperature was maintained at ambient conditions for three hours. The subsequent reaction was restarted at the same conditions (200°C) to determine if the shoulder reappeared under identical conditions.

In the second cycle, the shoulder is nearly absent from the acetone signal, with the reaction signals stabilizing more rapidly. This absence strongly suggests that the shoulder is not an artifact of isopropanol accumulation in the system or related to flushing effects. Instead, it indicates a transient property linked to the catalyst's initial activation or surface characteristics during the reaction.

The data strongly imply that the shoulder observed in the acetone signal originates from a characteristic property of the Co_3O_4 catalyst rather than an experimental artifact. The absence of the shoulder in the second cycle supports the hypothesis that this feature is linked to the initial activation or restructuring of the catalyst surface under reaction conditions. During the first cycle, specific catalytic sites on the Co_3O_4 may undergo changes (e.g., oxidation state transitions, rearrangements or consumption of adsorbed oxygen species) that temporarily enhance acetone production. By the second cycle, the catalyst surface has already undergone these changes, leading to a smoother transition into the steady-state reaction.

4.1.8 Reaction 2:1 (IPA:Oxygen) two cycles at 200°C for 2 hours with pretreatment step in between

The following figures present the final experiment aimed at investigating the origin of the observed shoulder in the acetone signal. The primary objective of this experiment was to confirm the hypothesis that the shoulder is an intrinsic property of the Co_3O_4 catalyst, likely associated with dynamic changes in its surface during the initial reaction phase. With the main aim being to find out whether an oxidative step, such as the pretreatment at 250°C, can restore this highly active state (shoulder).

Similar to previous experiments, the first cycle (Figure 16) was performed following a standard pretreatment step. The reaction was carried out at 200°C for two hours, during which the characteristic shoulder was observed, consistent with prior results.

Upon completion of the first cycle, the system was rapidly cooled to room temperature using external cooling. Once the system reached ambient conditions, it was flushed overnight with a flow of artificial air to remove any residual reactants or by-products.

The following day, a second pretreatment step was applied before initiating the same reaction cycle under identical conditions (200°C for two hours). This approach aimed to restore the catalyst's surface to its initial state, allowing further evaluation of the shoulder phenomenon.

Due to an experimental problem, the temperature detection only collected a few points during the process, although the temperature control worked normally. Consequently, tentative temperature curves (black) were estimated and manually added to approximately represent the reaction process.

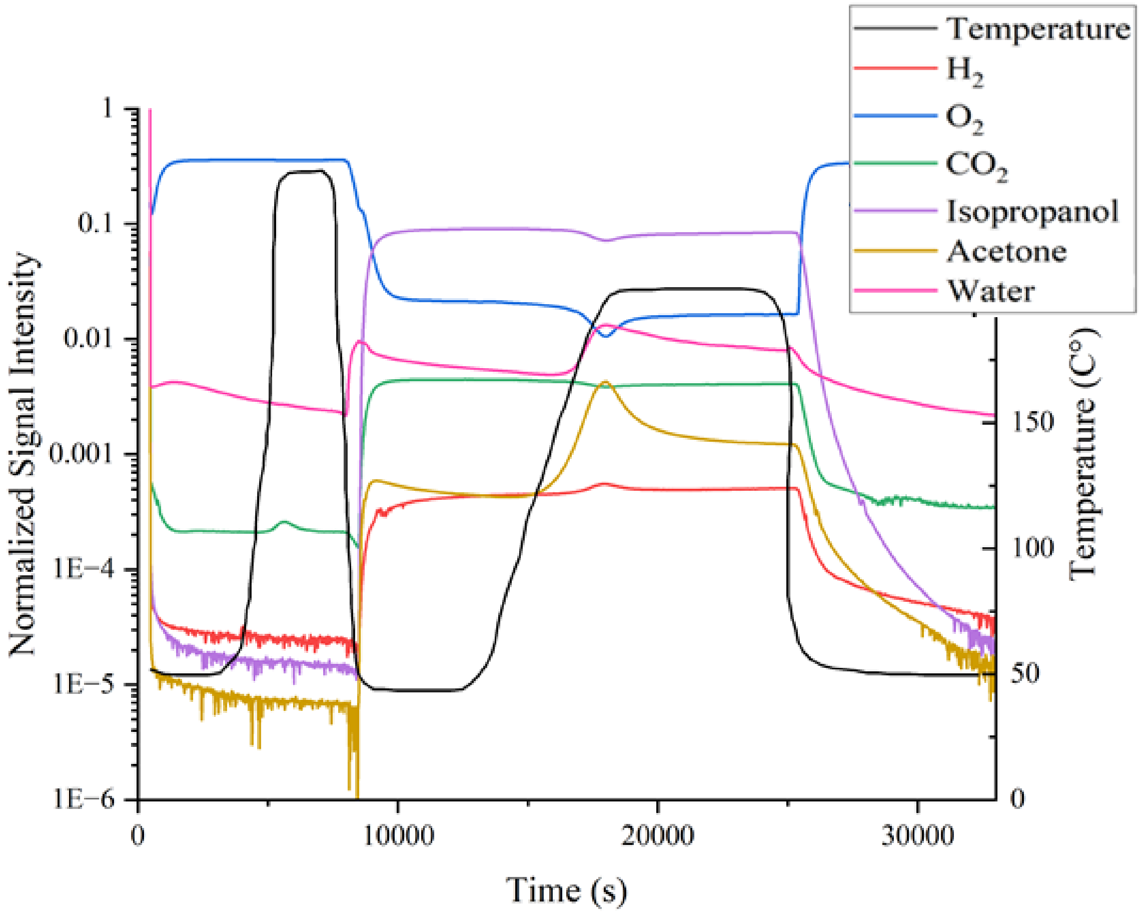

Figure 16: Reaction 2:1 (IPA:Oxygen) at 200°C for 2 hours, first cycle, including the pretreatment at 250°C

The acetone signal exhibits the characteristic shoulder, followed by stabilization of the reaction signals. This behaviour is consistent with previous findings and supports the hypothesis of dynamic structural changes occurring during the initial stages of catalysis.

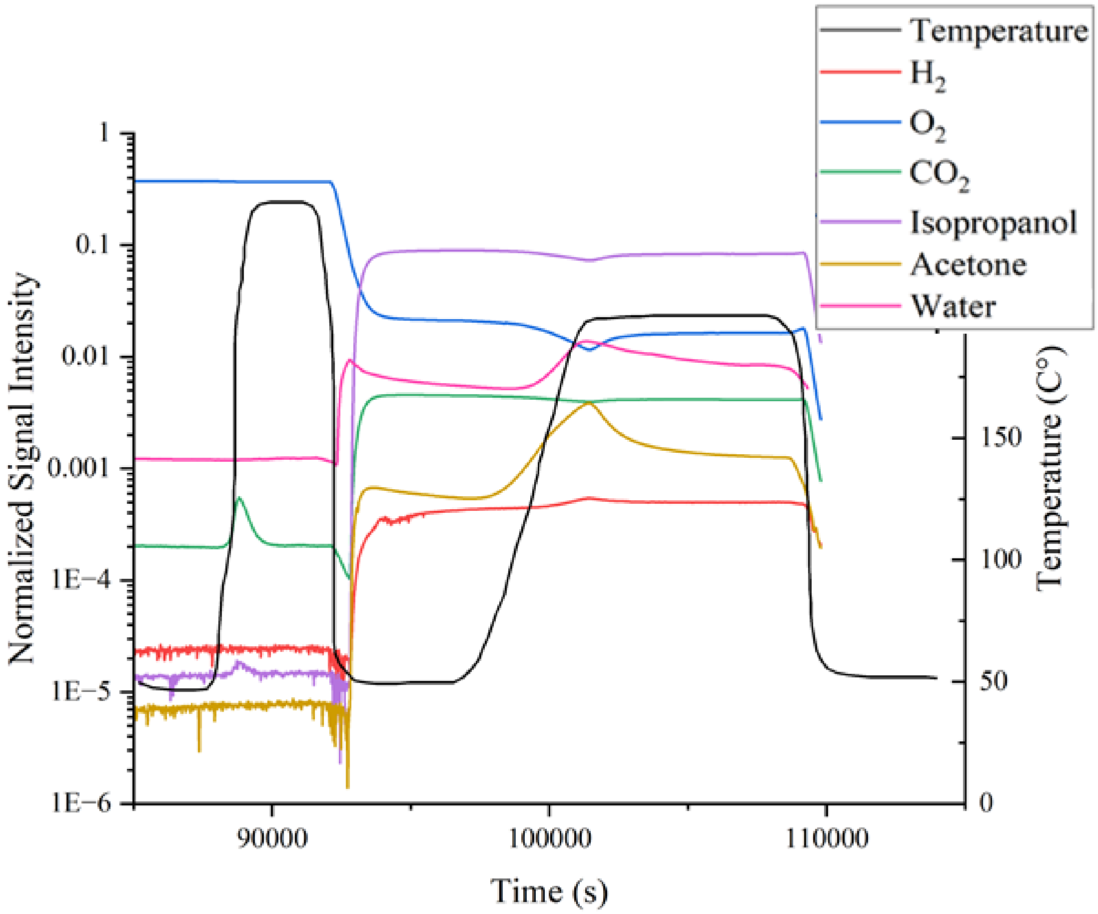

Figure 17: Reaction 2:1 (IPA:Oxygen) at 200°C for 2 hours, second cycle, including the pretreatment at 250°C

The second cycle (Figure 17) exhibits a shoulder in the acetone signal, persisting despite an overnight flushing and a thorough pretreatment step. This observation indicates that the shoulder, as it is restored, is an intrinsic property of the Co_3O_4 catalyst and is not attributable to external factors such as reactant accumulation or incomplete system flushing. This suggests a reactivation or restructuring of the cobalt oxide, potentially restoring its initial structural or chemical properties. This reformation likely resets the active sites on the catalyst surface, supporting the hypothesis that the shoulder originates from a dynamic restructuring of the catalyst.

Such behaviour reinforces the notion that the observed acetone signal shoulder is linked to intrinsic changes in the catalyst under reaction conditions. This assumption is emphasized as the CO_2 peak, observed during the second pretreatment, is heightened compared to the first, which could be an indication for the removal of carbonaceous species and/or residues that were formed during the first cycle.

Two mechanisms can explain these observations. First, the loss of oxidative enhancement posits that the pretreatment step imparts additional oxidative capability to the catalyst, effectively boosting its activity. This oxidative enhancement is subsequently expended at 200°C, after which the catalyst reverts to a baseline state with normal activity. Notably, simply cycling the temperature back down and returning to 200°C does not restore this boosted activity, whereas a new pretreatment step does. Importantly, the absence of phase changes in XRD confirms that no bulk reduction of the catalyst occurs during this process, although the lack of surface-specific data leaves open the possibility of subtle surface changes.

Alternatively, the observations could be explained by partial deactivation of the catalyst. While the persistence of the shoulder after rigorous flushing rules out the accumulation of intermediates, the possibility of a gradual deposition of material on the surface remains. Such deposits could deactivate some active sites while leaving others functional. This partial deactivation would align with the observed extra intensity of the CO_2 peak following the second pretreatment, suggesting that the pretreatment serves to clear these deposits and restore catalytic performance. The sustained acetone signal shoulder across cycles, even under these conditions, indicates that this deposition process, while impactful, does not fully inhibit the catalyst's activity.

Taken together, these findings provide strong evidence that the acetone signal shoulder is an intrinsic feature of the Co_3O_4 catalyst, linked to either a dynamic restructuring of the catalyst or processes affecting its surface activity under reaction conditions. The increased CO_2 signal during the second pretreatment underscores the dynamic and recoverable nature of the catalyst's active sites, reflecting potential changes in its surface structure. Further investigation, particularly with surface-sensitive techniques, is needed to fully resolve the contributions of these mechanisms.

4.2 Co_3O_4 by coprecipitation (1A)

4.2.1 N_2-physisorption

Figure 18 illustrates the hysteresis loop observed for the Co_3O_4 catalyst synthesized via coprecipitation. Additionally, a BET surface area of 121 m^2/g was determined.

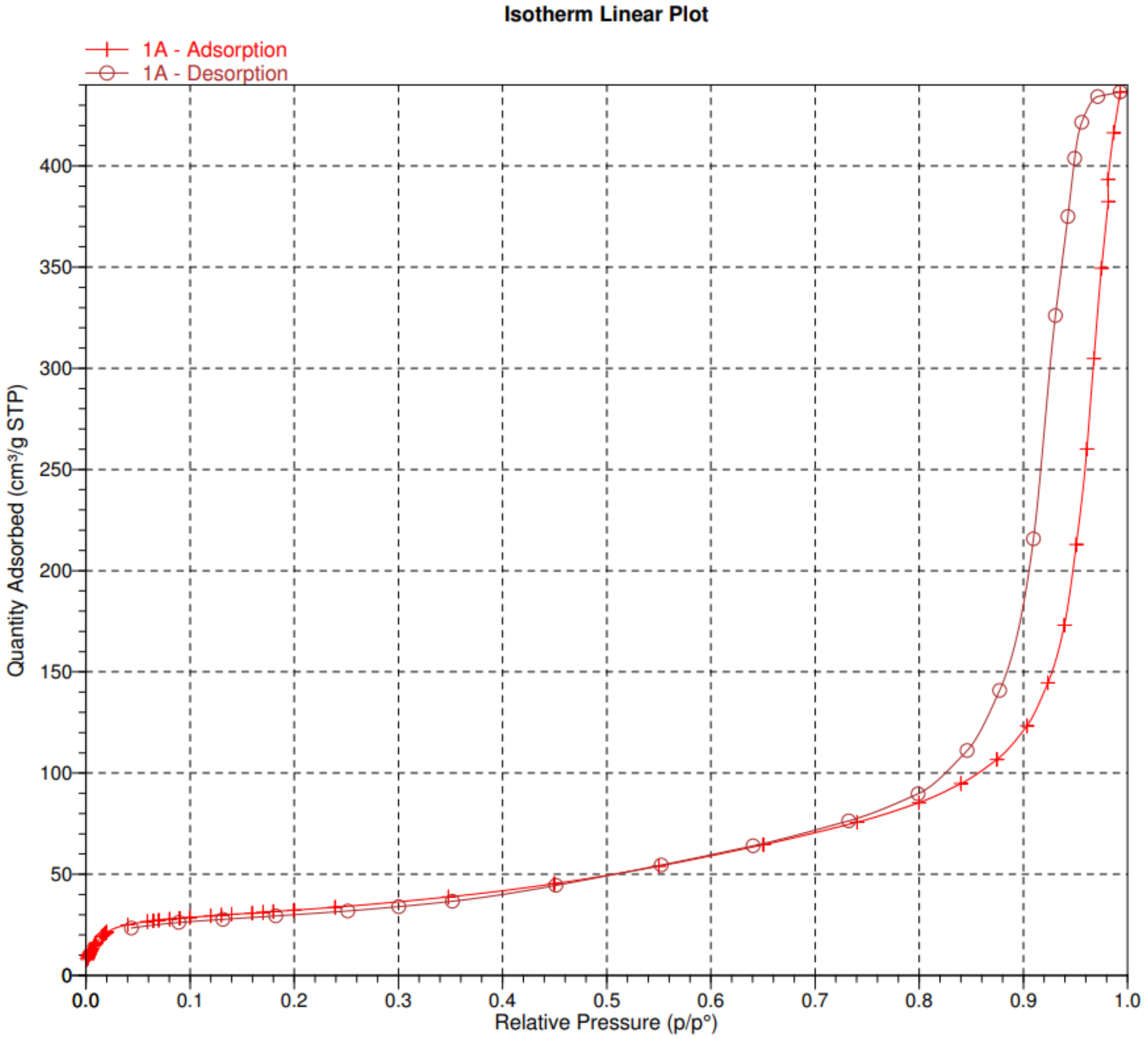

Figure 18: N_2 adsorption results for the 1A catalyst

The BET analysis of the Co_3O_4 catalyst synthesized by coprecipitation reveals significant differences compared to the combustion-synthesized sample discussed earlier. The isotherm, shown in Figure 18, displays features characteristic of a Type IV isotherm, including a pronounced hysteresis loop in the desorption branch, which indicates the presence of a mesoporous structure. At low relative pressures ($p/p_0 < 0.3$), the gradual increase in adsorption suggests strong surface interactions and the potential contribution of smaller pores, such as micropores or the initial filling of mesopores. This is followed by a steep rise in adsorption at higher relative pressures ($p/p_0 > 0.8$), consistent with capillary condensation occurring within mesopores.

The measured BET surface area of 121 m²/g is significantly higher than that of the combustion-synthesized Co_3O_4 catalyst, which measured 19.7 m²/g. This strong contrast highlights the impact of the coprecipitation synthesis method in producing a material with enhanced porosity and finer particle size. Furthermore, the maximum quantity adsorbed, exceeding 400 cm^3/g STP at p/p$_0$ ≈ 1, confirms the presence of a large pore volume, indicative of a highly porous structure.

These results suggest that the coprecipitation method leads to a well-developed mesoporous structure, with some contribution from micropores, providing high surface accessibility. The combination of a large surface area and mesoporosity likely enhances the material's catalytic potential, particularly in processes where surface interactions and diffusion through pores are critical. This distinct porosity and higher surface area emphasize the advantages of coprecipitation over combustion synthesis, further demonstrating the influence of synthesis methods on the resulting material properties. (M. Thommes, 2015)

4.2.2 XRD

The XRD pattern displayed in Figure 19 corresponds to the cobalt(II,III) oxide (Co_3O_4) material synthesized by combustion and subsequently calcined at 400°C for one hour.

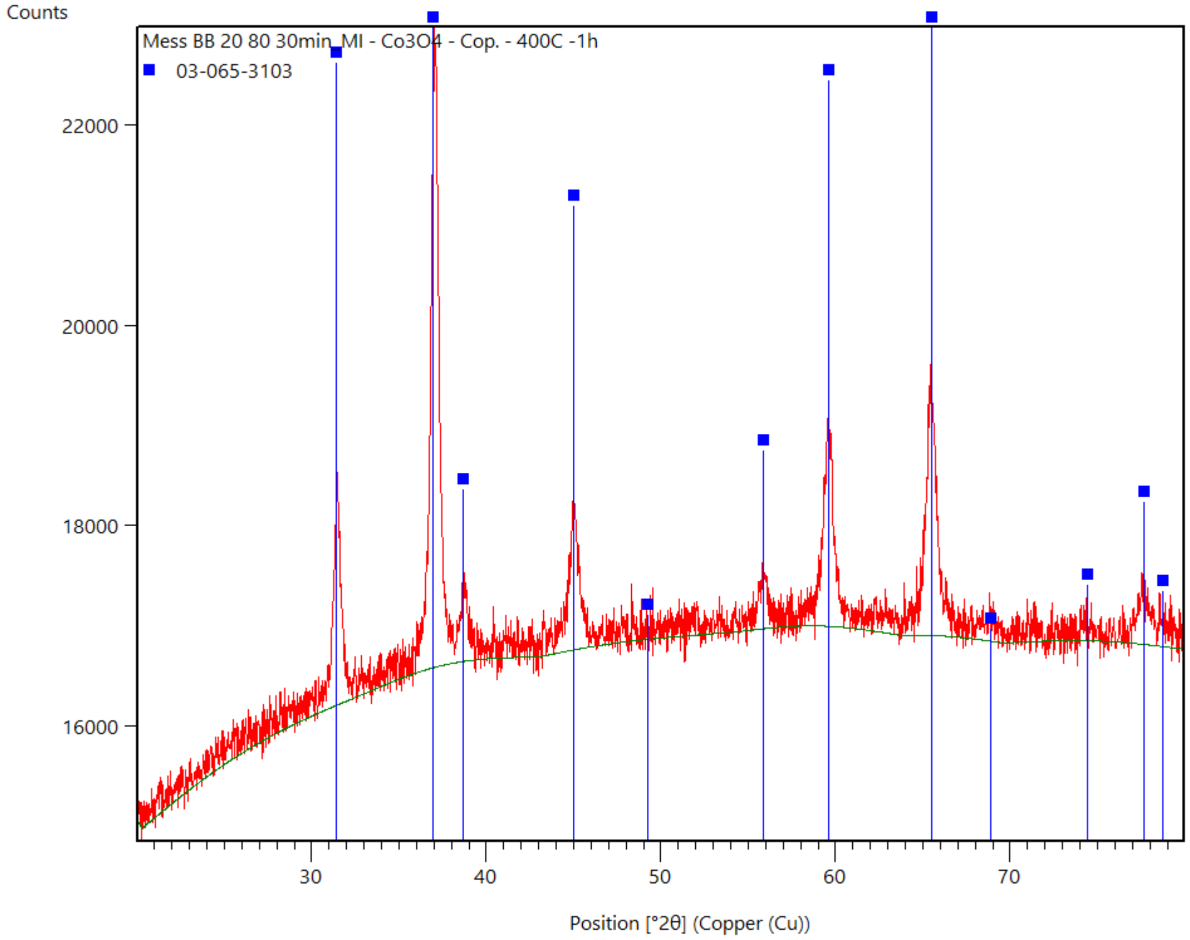

Figure 19: XRD of coprecipitation Co_3O_4 after calcination (400°C)

The red diffraction pattern represents the experimental data, while the blue lines denote the reference pattern for Co_3O_4. When comparing these results with those obtained from Co_3O_4

synthesized via combustion (Figure 10), the patterns appear nearly identical, with both clearly corresponding to the reference pattern of the spinel Co_3O_4.

The baseline, shown as the underlying green curve, is consistent with background contributions and does not obscure the identified peaks, affirming the clarity of the diffraction data.

In summary, the XRD analysis verifies the successful synthesis of phase-pure and crystalline Co_3O_4 with the spinel structure via the combustion process. The data reflect the material's structural integrity and high-quality crystalline nature.

4.2.3 Reaction 1:1 two cycles at 400°C for 30 min

The following Figure 20 illustrates the performance of Co_3O_4 synthesized via coprecipitation and calcined at 400°C for one hour in a reaction conducted over two cycles. Each cycle was carried out by keeping the final reaction temperature at up to 400°C for 30 min with an isopropanol-to-oxygen molar ratio of 1:1.

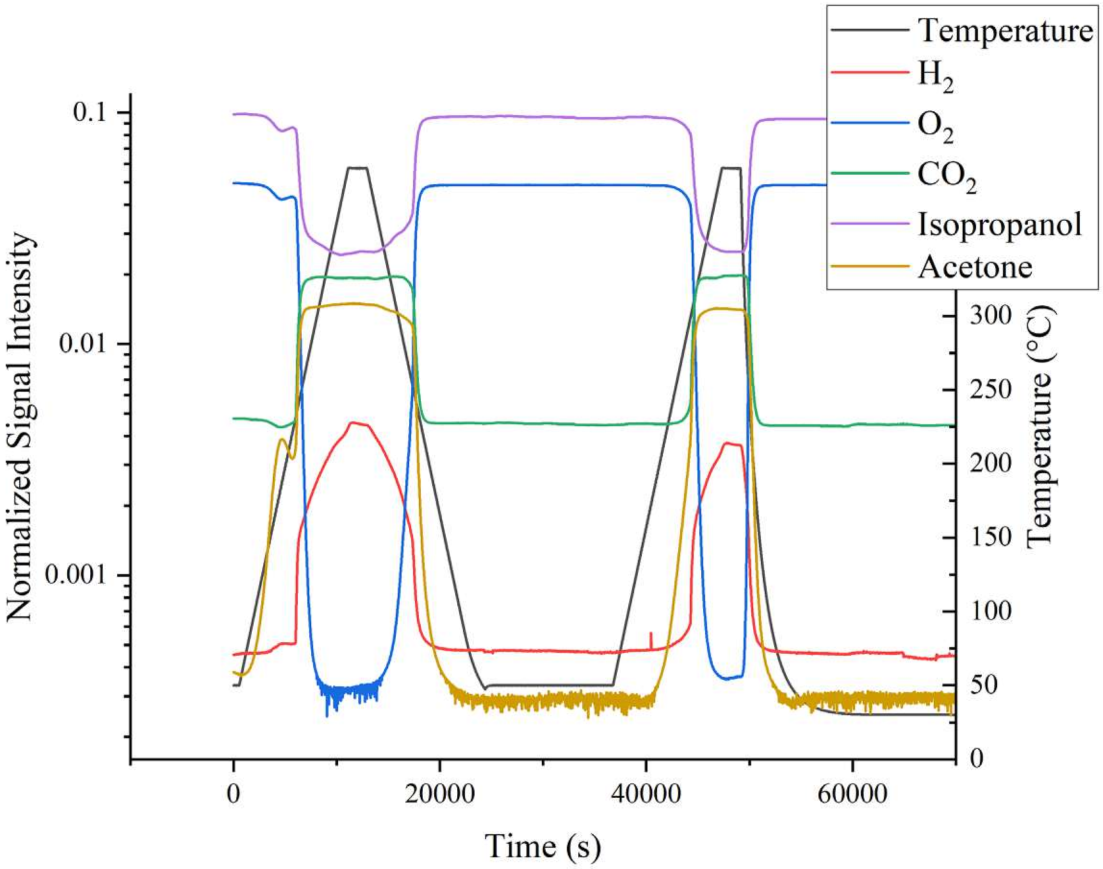

Figure 20: Coprecipitation sample after reaction 1:1 two cycles at 400°C for 30 min

The purpose of this experiment was to investigate the catalytic behaviour of cobalt oxide prepared by coprecipitation under elevated temperatures and repeated reaction cycles. Compared to the results discussed in Chapter 4.1, the characteristic shoulder observed in the first cycle is still present, even though the samples (C3A and 1A) were prepared using different synthesis methods. This consistency suggests that the shoulder is an intrinsic feature of cobalt oxides or that the calcination and/or pretreatment process leads to the production of surfaces with similar features.

At the higher reaction temperature used here, the shoulder appears more distinct, likely due to increased reaction rates or structural dynamics at elevated temperatures. Interestingly, no shoulder is observed during the second cycle, implying that the structural transformation of the catalyst was completed during the first cycle and that the highly active sites are completely blocked/deactivated.

A notable difference compared to the C3A sample is the significantly higher CO_2 signal intensity in the 1A sample, highlighting differences in catalytic behaviour between the two materials. Additionally, the signals for acetone, CO_2, and oxygen reach a stable plateau during both cycles, suggesting consistent reaction kinetics throughout the experiment.

Overall, the data confirm that both, selective and total oxidation occur during the reaction and that the 1A sample is less selective for acetone production compared to the C3A sample. This highlights the influence of the synthesis method on the catalytic properties of cobalt oxide.

4.3 Nanocast catalysts

The samples analyzed in this chapter were synthesized and provided by Dipl. Ing. Patrick Guggenberger from the research group of Professor Freddy Kleitz at the University of Vienna. The objective of this chapter was to evaluate the efficiency, performance, and catalyst compositions to identify the most effective one.

The nanocasting synthesis of catalysts was carried out using a hard template, such as ordered mesoporous silica, to fabricate materials with high specific surface areas and precisely controlled pore architectures. Transition metal nitrate salts are impregnated into the template, followed by a low-temperature calcination process in semi-sealed containers. This approach maintains mesoporosity while enabling the formation of phase-pure, multi-metal oxide spinels. The semi-sealed environment facilitates the retention of humidity and gaseous byproducts, which enhances the mobility of precursors, leading to better pore replication and uniform elemental distribution. The resulting materials exhibit excellent structural stability, making nanocasting a cost-effective and versatile method for synthesizing advanced catalysts. (P. Guggenberger, 2024)

All reactions were carried out under identical parameters to ensure optimal comparability. Additionally, the calcination temperature for all tested samples was maintained at 500°C. The experiments were conducted under the prescribed pretreatment conditions, followed by two reaction cycles with an isopropanol-to-oxygen molar ratio of 1:1 up to 400°C, with a controlled heating rate of 10°C/min instead of the previously used rate of 2°C/min.

The primary objective of these experiments was to obtain a general overview of the catalytic performance and to determine whether specific catalyst compositions deserve further investigation.

4.3.1 Co_3O_4 (PG621)

The first sample analyzed was a Co_3O_4 catalyst. This sample was selected as it served as the foundation for previous analyses, providing a standard reference point for comparability and facilitating a deeper understanding of catalytic behaviour.

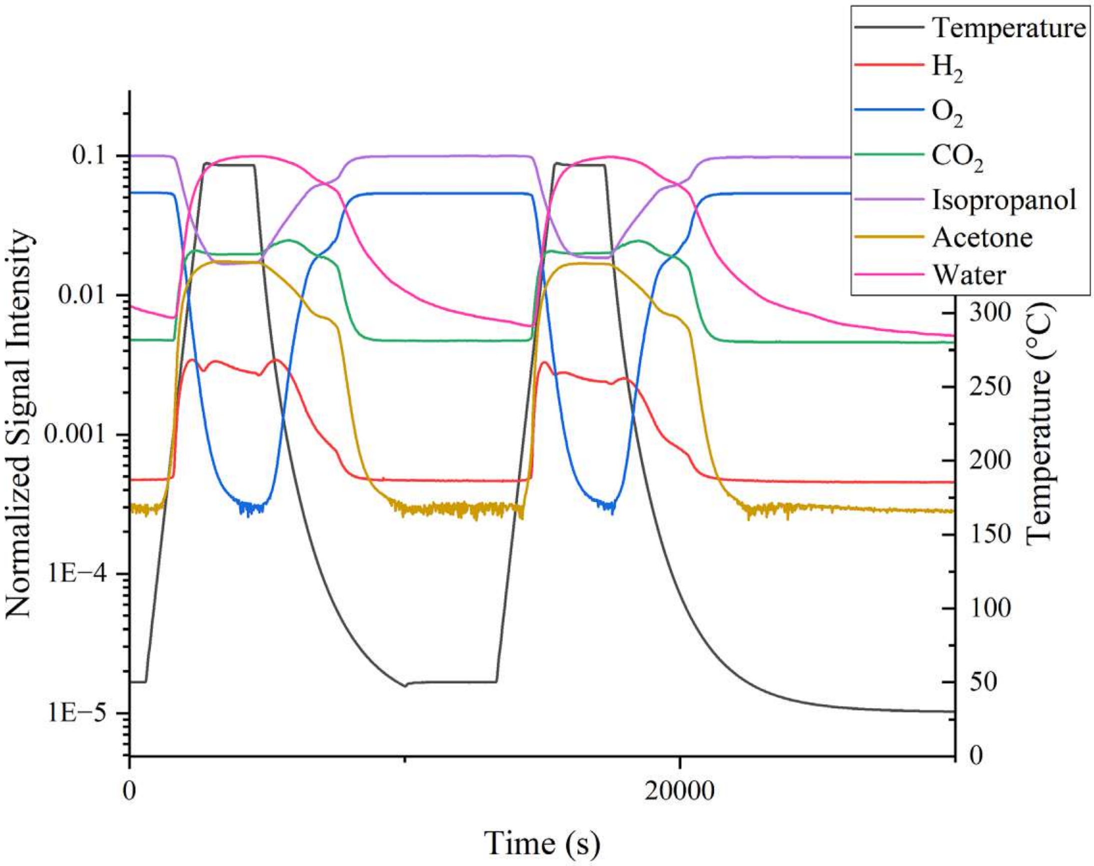

Figure 21: Reaction of Co_3O_4 (PG621) two cycles at 400°C for 30 min (1:1)

The Figure 21 illustrates the well-documented reaction trends of cobalt oxide with two notable distinctions. The first and most significant difference is the absence of the previously observed shoulder in the data, which can likely be attributed to the use of a higher heating rate during the measurements for this sample. A faster heating rate may have smoothed out transient features, thereby masking such details.

The second point of interest lies in the behaviour of the graphs during the cooling phase. Instead of a progressive decrease in the signals of acetone, CO_2, and H_2, along with a corresponding increase in oxygen and isopropanol, an unexpected transient increase in reaction activity is observed before the parameters return directly to their initial baseline values. This phenomenon suggests a brief surge in catalytic activity or a final reaction step occurring as the system transitions back to its starting conditions.

Another plausible interpretation is that the shoulder observed at the onset of the cooling phase could be a manifestation of catalytic hysteresis. This phenomenon may arise as variations in reaction rates or product yields between heating and cooling cycles in a temperature-dependent reaction, potentially caused by changes in the catalyst's surface states, active sites, or phase transitions.

4.3.2 $MnCo_2O_4$ (PG614)

Figure 22 depicts the reaction behaviour of the $MnCo_2O_4$ catalyst under the same reaction parameters as previously described.

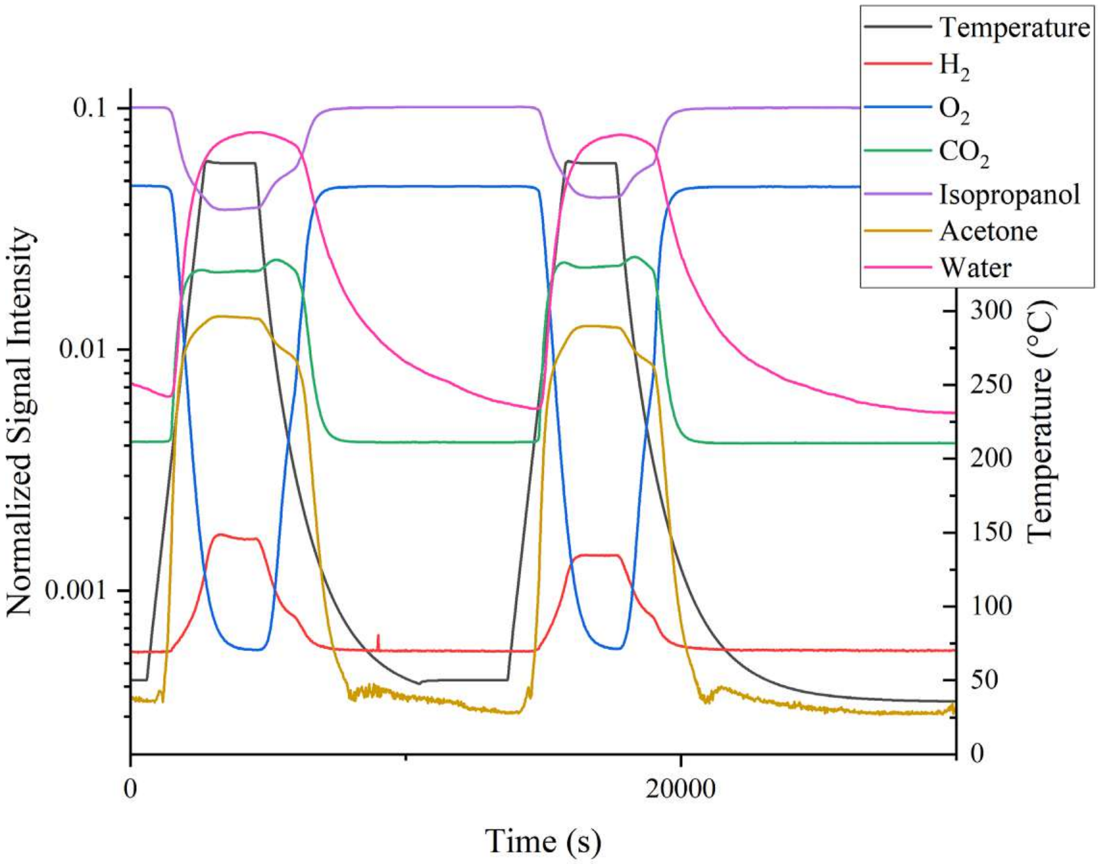

Figure 22: Reaction of $MnCo_2O_4$ (PG614) two cycles at 400°C for 30 min (1:1)

Compared to the Co_3O_4 catalyst, the reaction shows an absence of transient features. However, similar to the Co_3O_4 catalyst, a transient increase in reaction activity is observed during the cooling phase, although this phenomenon is less pronounced in terms of duration.

Additionally, the hydrogen production seems to occur predominantly at the reaction temperature of 400°C. The signal increases progressively with the temperature and stabilizes at a plateau once 400°C is reached. This behaviour suggests that the catalyst exhibits its highest activity for hydrogen production at this temperature.

4.3.3 $CrCo_2O_4$ (PG613)

Figure 23 illustrates the performance of the $CrCo_2O_4$ catalyst under the specified reaction parameters.

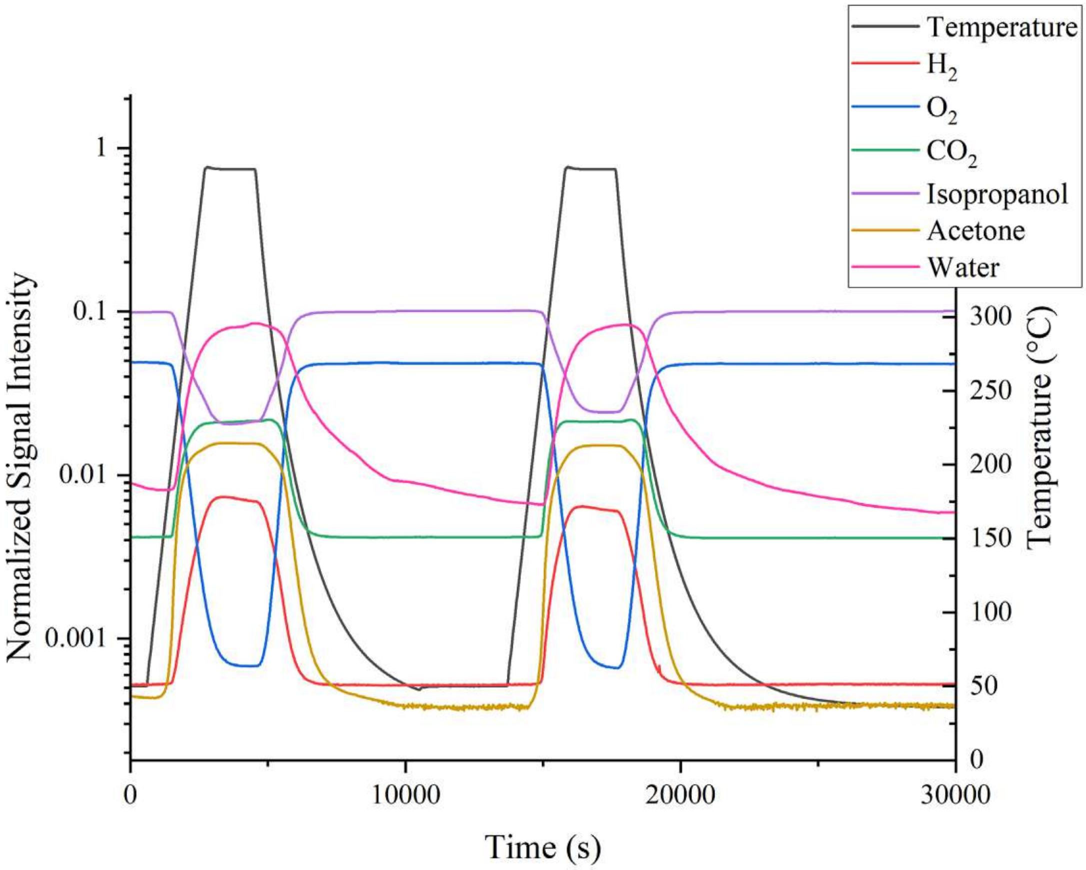

Figure 23: Reaction of $CrCo_2O_4$ (PG613) two cycles at 400°C for 30 min (1:1)

The reaction profile exhibits no significant deviations from the expected behaviour: a gradual increase in signal intensity as the temperature rises, a stable plateau during the reaction at 400°C, and a decline in signal intensity during the cooling phase with a less pronounced hysteresis. No additional notable features or transient phenomena are observed.

The reaction results indicate the production of CO_2, acetone, and hydrogen, suggesting that both selective oxidation (leading to acetone formation) and complete oxidation (resulting in CO_2 production) are occurring simultaneously.

4.3.4 $NiCo_2O_4$ (PG617)

Figure 24 shows the performance of the $NiCo_2O_4$ catalyst under the specified reaction parameters.

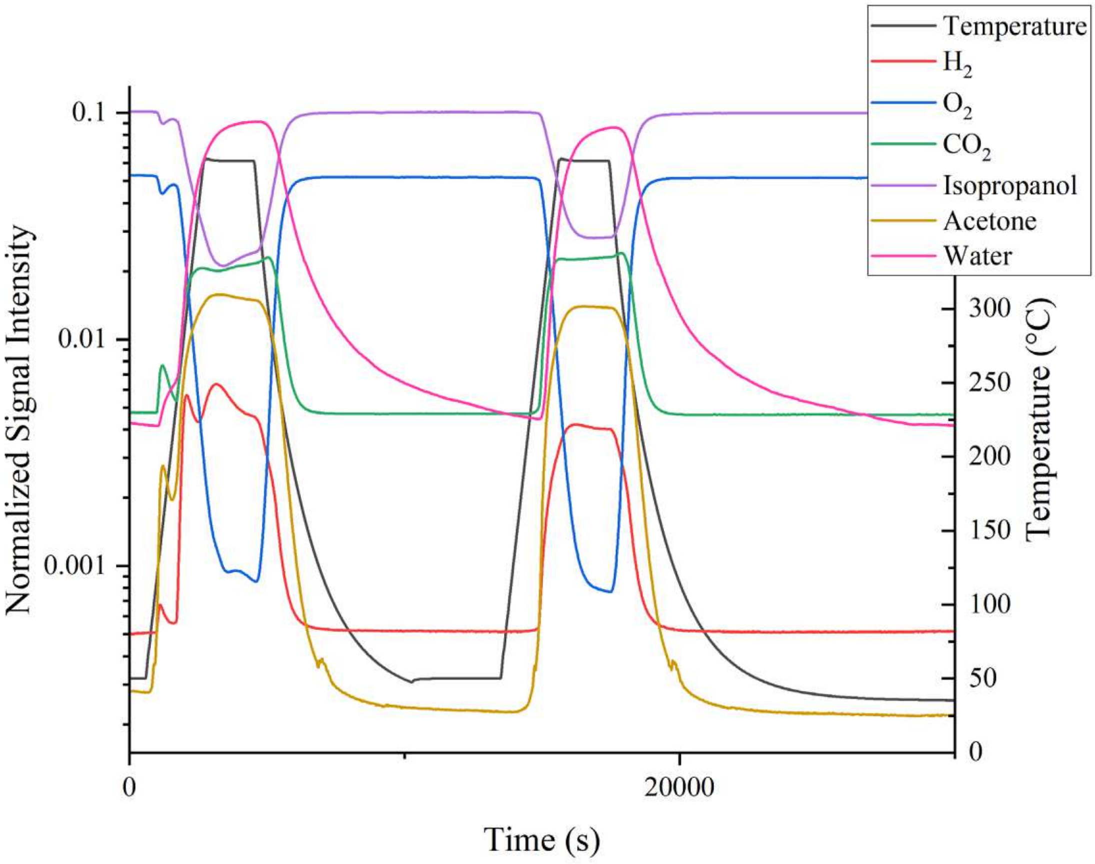

Figure 24: Reaction of $NiCo_2O_4$ (PG617) two cycles at 400°C for 30 min (1:1)

The reaction profile reveals intriguing results, particularly in terms of potential side reactions and/or alterations in surface or structural properties of the catalyst. Notably, while the first cycle exhibits a distinct shoulder across all signals, this feature is completely absent in the second cycle. This observation is especially significant, as similar shoulders were not detected for the Co_3O_4 catalyst when analysed under higher heating rates.

Additionally, the hydrogen signal displays not just one, but three distinct local maxima: the first occurs at approximately 70°C, aligning with similar features observed across all signals; the second peak emerges near 250°C, indicating an initial maximum in selective oxidation yield; and the third peak is evident at the onset of the 400°C heating phase. Following this, the hydrogen signal gradually decreases during the 400°C reaction plateau, while the CO_2 signal shows a slight increase. This behaviour suggests a potential reduction in selectivity toward selective oxidation at elevated temperatures.

The second cycle, in contrast, exhibits a simpler behaviour, resembling the profile observed for the $CrCo_2O_4$ catalyst, with well-defined increases, plateaus, and decreases in signal intensities, but lacking the complex transient features of the first cycle.

4.3.5 $CuCo_2O_4$ (PG619) and $ZnCo_2O_4$ (PG620)

The subsequent catalysts, $CuCo_2O_4$ (Figure 25) and $ZnCo_2O_4$ (Figure 26), were evaluated under identical reaction conditions. Both samples exhibit nearly identical reaction profiles, with the only clear distinction being the signal intensities. The $CuCo_2O_4$ catalyst demonstrates significantly higher reactivity compared to $ZnCo_2O_4$.

No additional shoulders or notable anomalies are observed in the reaction profiles of either catalyst. It is worth noting the intriguing behaviour of isopropanol during the reaction, as its concentration appears to decrease further with prolonged reaction time at a constant temperature. This observation suggests that the maximum rate of isopropanol consumption may not occur immediately at the onset of the reaction but rather after a certain delay.

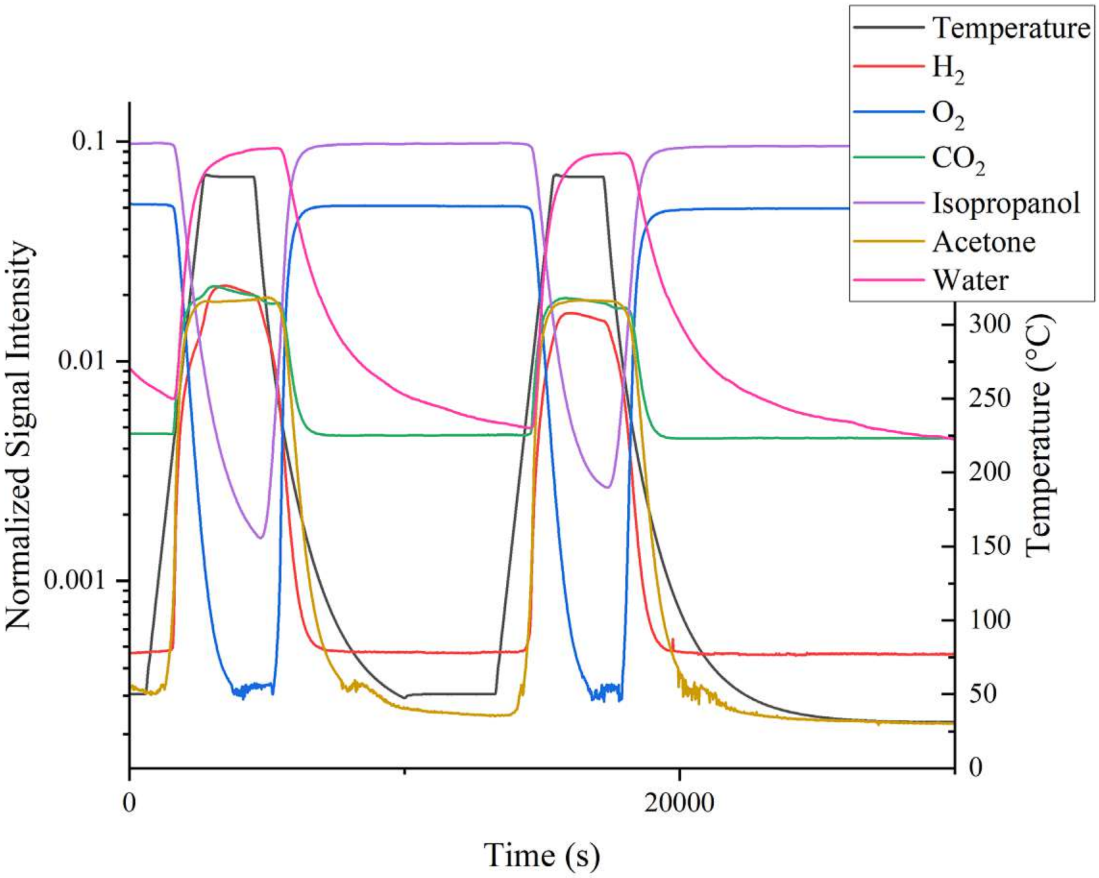

Figure 25: Reaction of $CuCo_2O_4$ (PG619) two cycles at 400°C for 30 min (1:1)

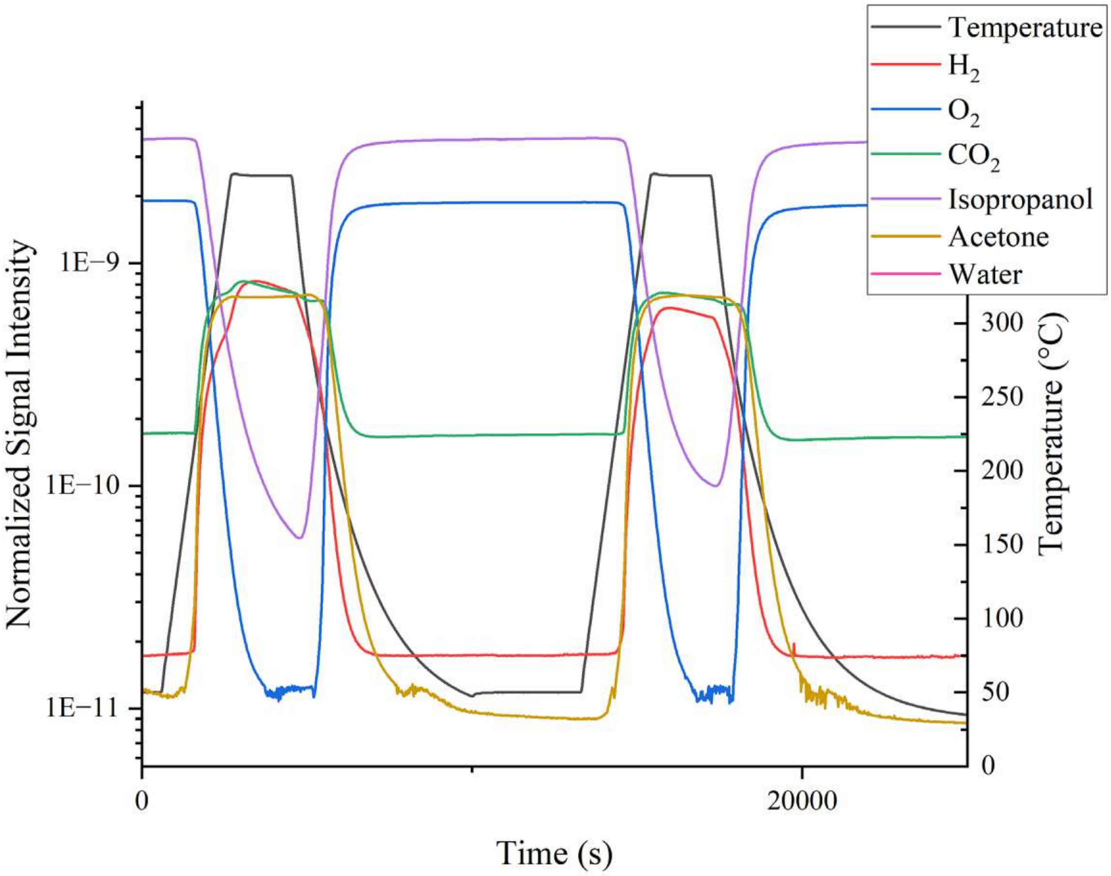

Figure 26: Reaction of $ZnCo_2O_4$ (PG620) two cycles at 400°C for 30 min (1:1)

4.4 XRD after reactions

4.4.1 C3A: Reaction 2:1 (IPA:Oxygen) at 400°C for 30 min

Figure 27 presents the XRD pattern of the combustion-synthesized Co_3O_4 catalyst following its use in a reaction conducted at 400°C for 30 minutes with an isopropanol-to-oxygen ratio of 2:1.

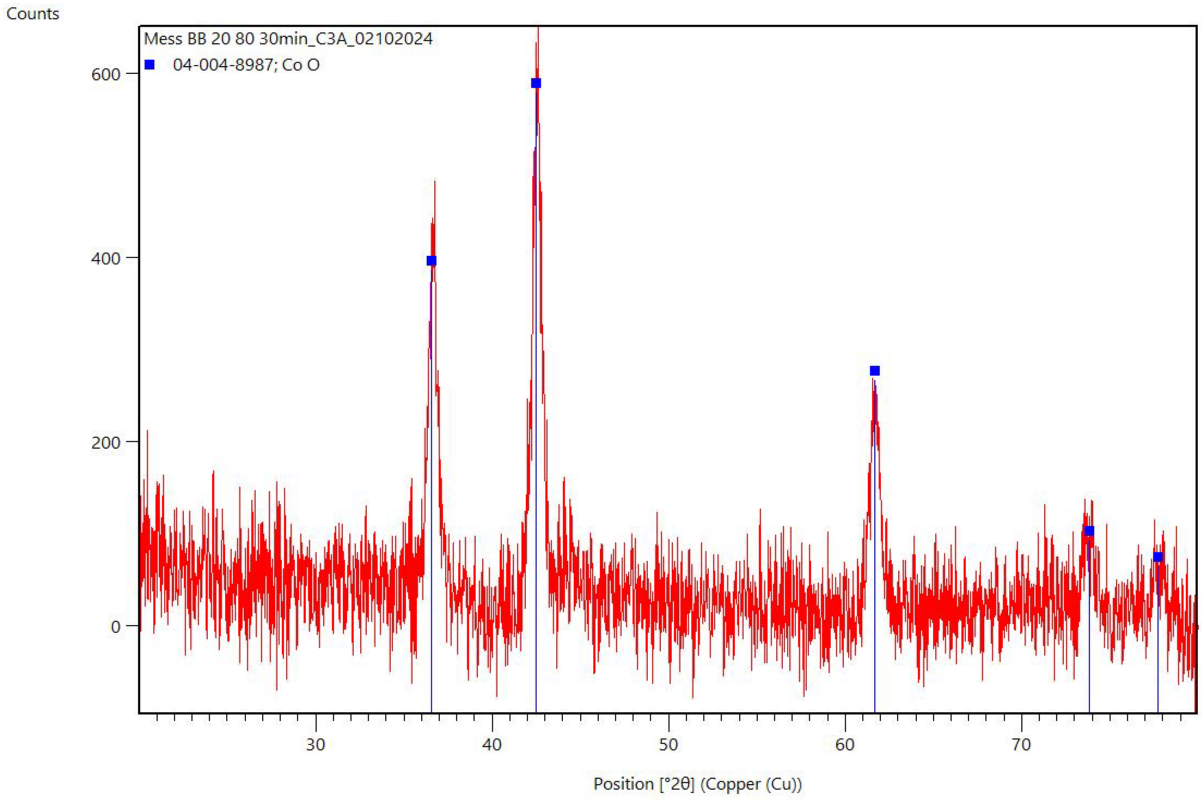

Figure 27: XRD of combustion Co_3O_4 after reaction at 400°C for 30 min

The diffraction peaks observed at approximately 36.5°, 42.4°, and 61.5° (2θ) are characteristic of CoO (cobalt(II) oxide), as confirmed by the blue reference pattern. The absence of peaks corresponding to metallic cobalt (e.g., ~44.2° and ~51.5°) or Co_3O_4 (e.g., ~36.8°, ~42.4°, and ~61.4° for the spinel phase) indicates a significant transformation of the catalyst during the reaction.

The data indicate that the catalyst predominantly consists of CoO after the reaction, with no detectable remnants of the spinel Co_3O_4 phase. The sharp and well-defined peaks in the XRD pattern demonstrate that the CoO phase is highly crystalline.

The results suggest that Co_3O_4 undergoes reduction under the reaction conditions, likely due to isopropanol (IPA) acting as a reducing agent. During the process, IPA oxidizes by extracting oxygen from the catalyst. This is followed by a lack of sufficient oxygen to replenish the catalyst, as the available oxygen concentration is inadequate to restore the missing oxygen. This reduction also accounts for the absence of the shoulder observed during a subsequent reaction cycle, suggesting that the reaction temperature of 400°C creates a highly reducing environment for the catalyst.

4.4.2 C3A: Reaction 2:1 (IPA:Oxygen) at 200°C for 30 min

Figure 28 presents the XRD pattern of the C3A catalyst following its following its use in a reaction conducted at 200°C for 30 minutes.

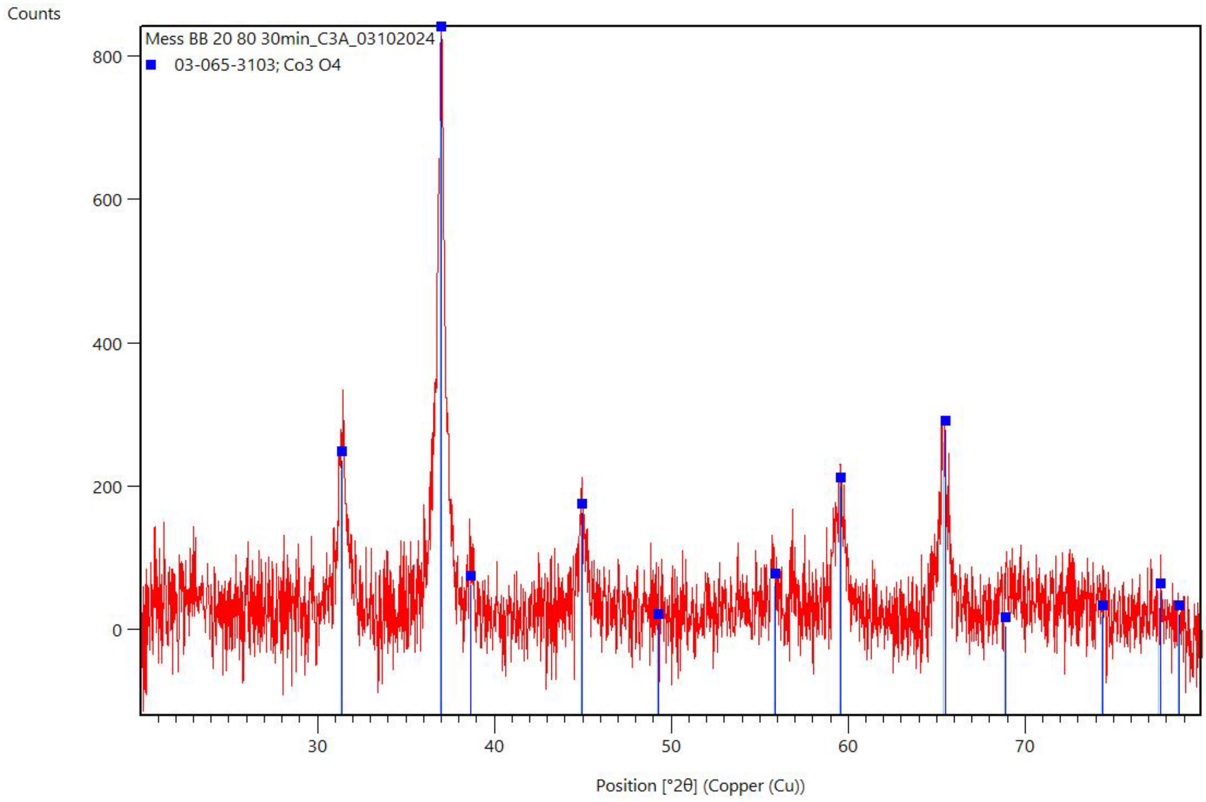

Figure 28: XRD of combustion Co_3O_4 after reaction at 200°C for 30 min

The catalyst shown in Figure 28 exhibits, in contrast to Figure 27, a clear match with the reference pattern for Co_3O_4 (spinel phase), as indicated by the blue markers. The most prominent peaks at approximately 31.2°, 36.8°, 44.8°, 59.4°, and 65.2° (2θ) correspond to the characteristic diffraction planes of the Co_3O_4 spinel phase. The presence of distinct and sharp Co_3O_4 peaks indicates that the catalyst retained its spinel structure during the reaction.

No additional peaks corresponding to other phases, such as CoO (cobalt(II) oxide) or metallic cobalt (Co), are visible. This suggests that the catalyst did not undergo significant reduction under the reaction conditions, even though it is possible that the surface was affected by the process.

Furthermore the sharpness of the Co_3O_4 peaks suggests that the reaction conditions did not affect the structure. The background remains relatively low and does not exhibit significant broadening, which suggests minimal amorphous content or secondary phases.

4.4.3 C3A: Reaction 2:1 (IPA:Oxygen) at 200°C for 8 hours

Figure 29 shows the XRD pattern of the combustion Co_3O_4 catalyst after its reaction at 200°C for eight hours.

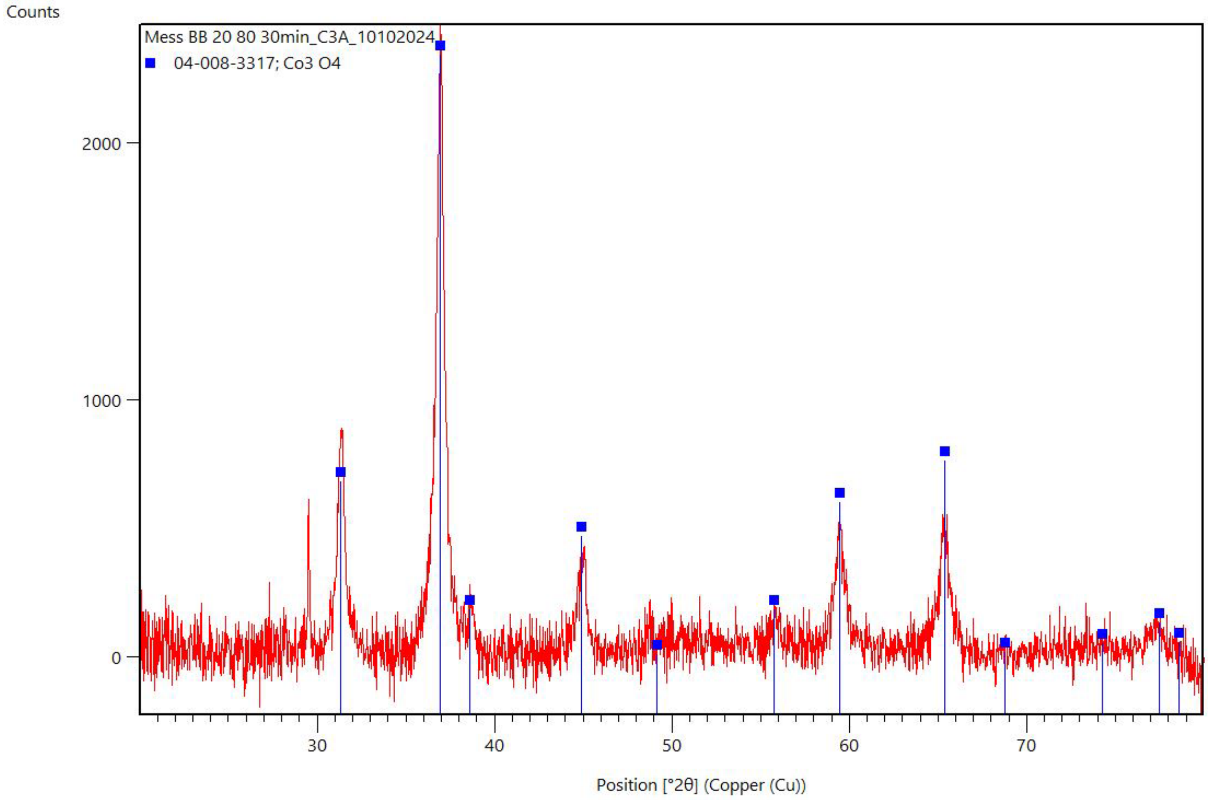

Figure 29: XRD of combustion Co_3O_4 after reaction at 200°C for eight hours

Similar to the catalyst in Figure 28, no evidence of the formation of other phases or oxidation states is observed. This is particularly noteworthy given that the reaction lasted for eight hours, which theoretically would provide ample time for reduction. However, the absence of any such transformation suggests that reduction of the catalyst occurs only at temperatures higher than 200°C, as seen in Figure 27. This supports the observation that the decrease in activity after the shoulder is not due to a significant reduction.

4.4.4 C3A: Reaction 2:1 (IPA:Oxygen) two cycles at 200°C for 4 hours

Figure 30 presents the XRD pattern of the C3A catalyst following its exposure to a reaction two cycles at 200°C for four hours.

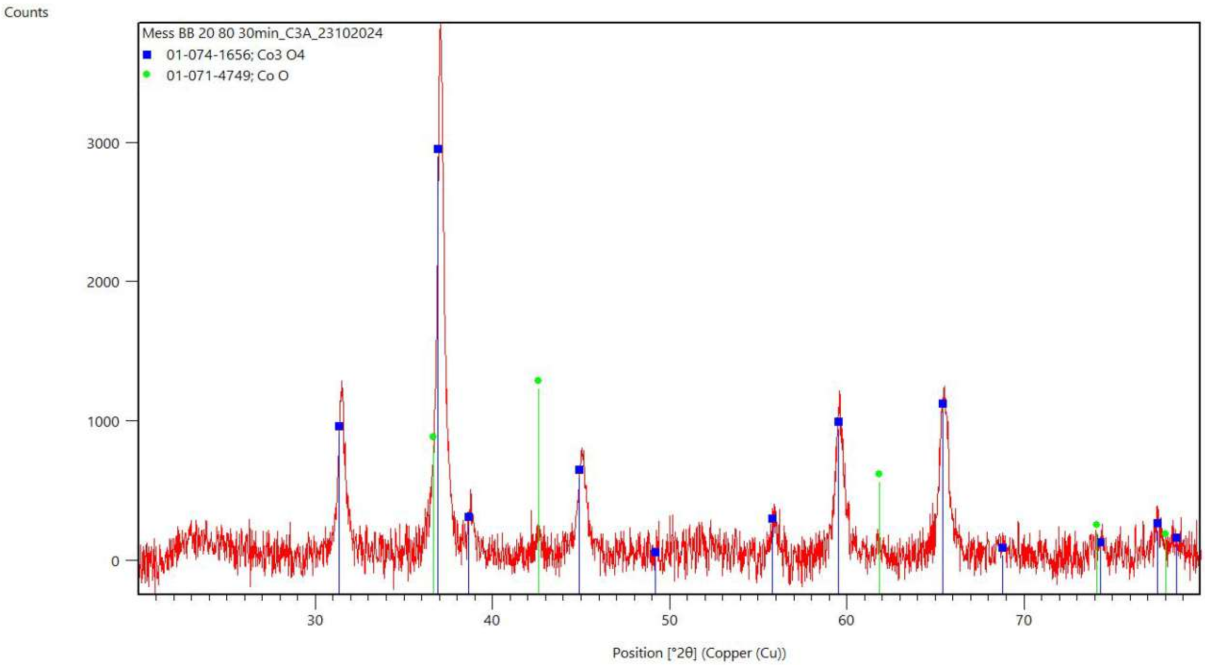

Figure 30: XRD of combustion Co_3O_4 after reaction two cycles at 200°C for 4 hours

Although the XRD pattern clearly demonstrates that the catalyst predominantly retained its initial spinel structure, the presence of CoO signals suggests the initiation of other oxide phase formations. This observation is particularly intriguing, as a previously conducted experiment, in which the catalyst was also subjected to eight hours of exposure at the same temperature, revealed no structural changes. This discrepancy could imply that the cooling process, and potentially even the heating procedure, influence the tendency to form alternative oxidation states. Alternatively, and perhaps more plausibly given the subsequent findings, the CoO signals might arise from contamination during sample preparation, as their intensity is relatively low.

4.4.5 C3A: Reaction 2:1 (IPA:Oxygen) two cycles at 200°C for 2 hours with a pretreatment step in between

Figure 31 shows the XRD pattern of the combustion Co_3O_4 catalyst after its reaction in two cycles at 200°C for two hours.

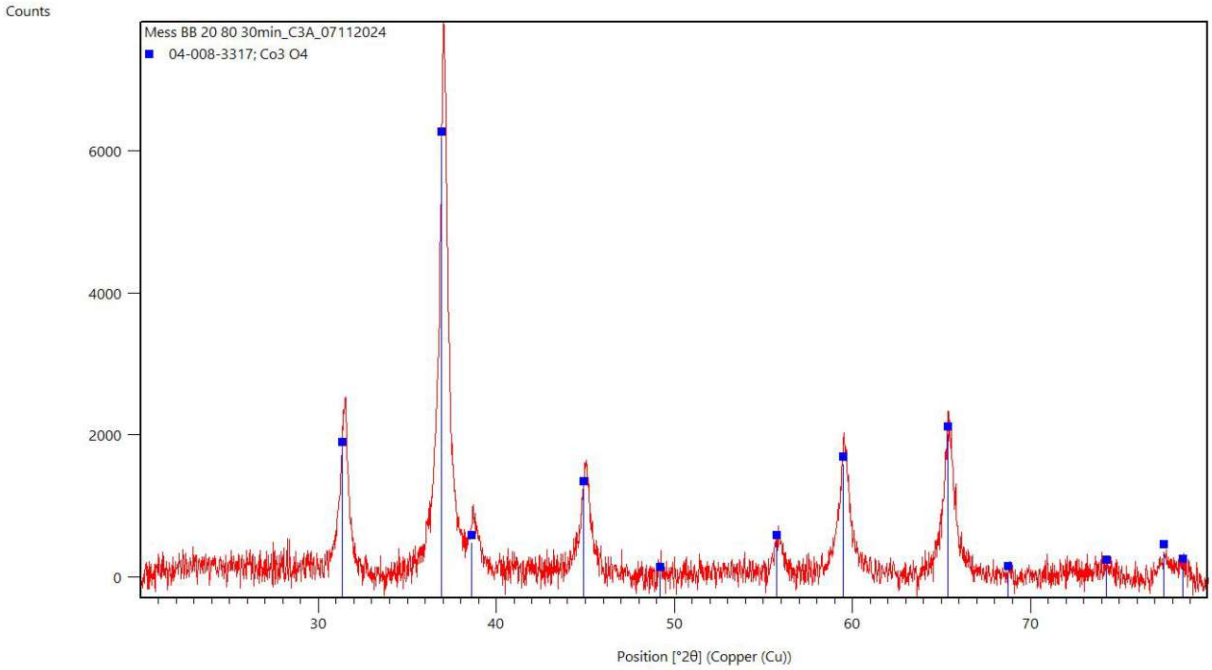

Figure 31: XRD of combustion Co_3O_4 after reaction two cycles at 200°C for 2 hours with a pretreatment step in between

The XRD pattern indicates the clear and potentially exclusive presence of the spinel structure in the catalyst, with no significant structural alterations observed. This finding supports the hypothesis that the catalytic structure is minimally, if at all, influenced by the heating and cooling processes itself during the reaction. Furthermore, the XRD data reveal that a reaction temperature of 200°C, regardless of the duration, does not impact the structural integrity of the catalyst. This suggests that structural changes require exposure to temperatures exceeding 200°C.

4.4.6 Co_3O_4 (PG621)

The shown XRD pattern (Figure 32) represents a post-reaction analysis of the PG621 (Co_3O_4) catalyst.

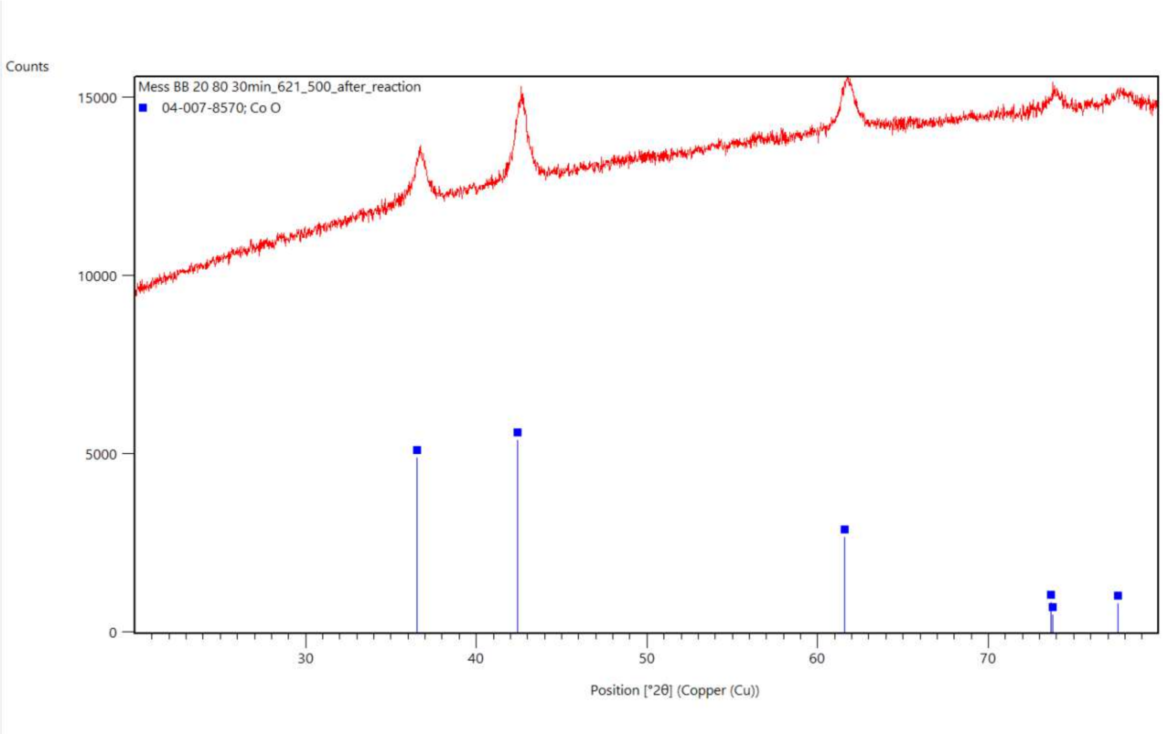

Figure 32: XRD of PG621 after reaction

The diffraction peaks observed in the spectrum correspond to CoO, indicating that the original Co_3O_4 phase underwent partial reduction to CoO during the reaction. This transformation is likely a result of the reducing conditions at temperatures up to 400°C. The characteristic Co_3O_4 peaks, typically located around $2\theta \approx 31°$, 36°, and 65°, are absent, further supporting a complete phase transition.

The reduction of Co_3O_4 to CoO is a well-documented phenomenon under reducing conditions and is often associated with the activation of cobalt oxide catalysts. The CoO phase is known to be catalytically active, particularly for selective oxidation reactions, as it provides accessible redox-active sites.

The phase transformation from Co_3O_4 to CoO could have implications for the long-term stability and selectivity of the catalyst, depending on the reaction conditions and the duration of operation.

4.4.7 $MnCO_2O_4$ (PG614)

Figure 33 shows the post-reaction XRD analysis of the PG614 ($MnCo_2O_4$) catalyst.

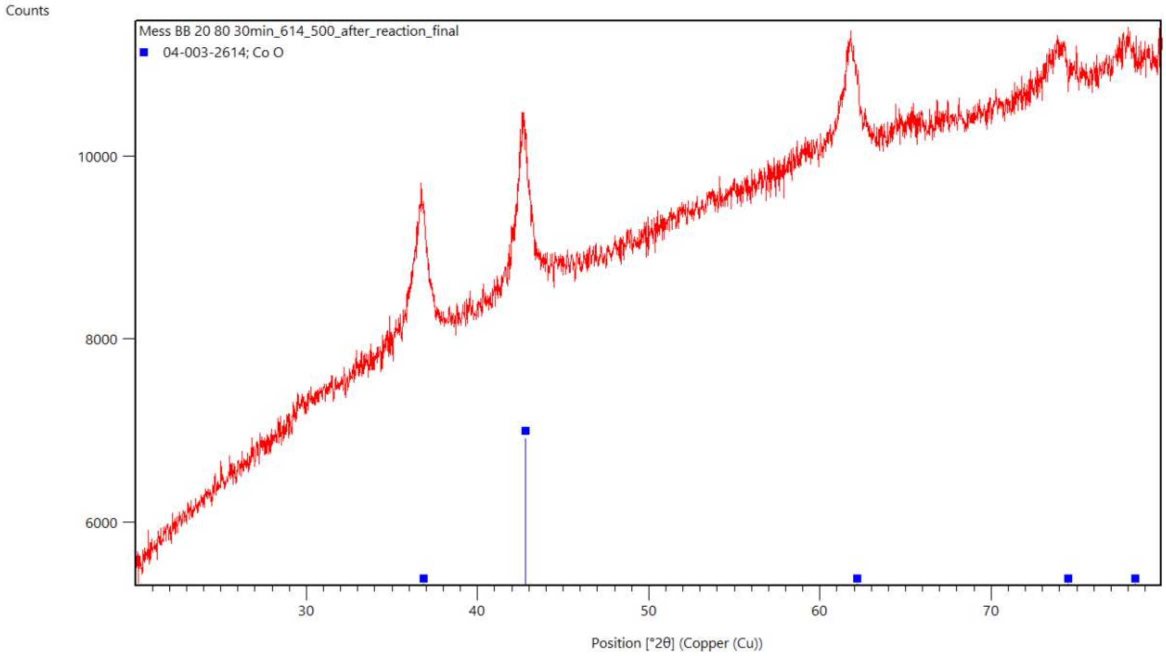

Figure 33: XRD of PG614 after reaction

The observed diffraction peaks align with the reference pattern for CoO, indicating a significant phase transformation during the reaction. The reduction of $MnCo_2O_4$ to (Mn,Co)O reflects the reducing conditions experienced by the catalyst during the process. The reduction to (Mn,Co)O implies that the catalyst undergoes substantial structural changes during the reaction, which could have implications for its long-term stability and catalytic performance. It is important to note that CoO and (Mn,Co)O possess the same crystalline structure, resulting in identical XRD reflection patterns.

No discernible diffraction peaks corresponding to $MnCo_2O_4$ or manganese-based oxide species are present. The sharpness of the diffraction peaks confirms the crystalline nature of the (Mn,Co)O phase, while the minimal peak broadening suggests moderate crystallite sizes.

The absence of $MnCo_2O_4$ diffraction features and the emergence of (Mn,Co)O signals indicate that manganese does not significantly stabilize the mixed oxide structure under the given reaction conditions. Furthermore the absence of crystalline manganese-based phases raises questions about the role of manganese post-reaction.

4.4.8 $CrCo_2O_4$ (PG613)

The following Figure 34 shows the XRD pattern of the PG613 ($CrCo_2O_4$) catalyst after usage in a reaction.

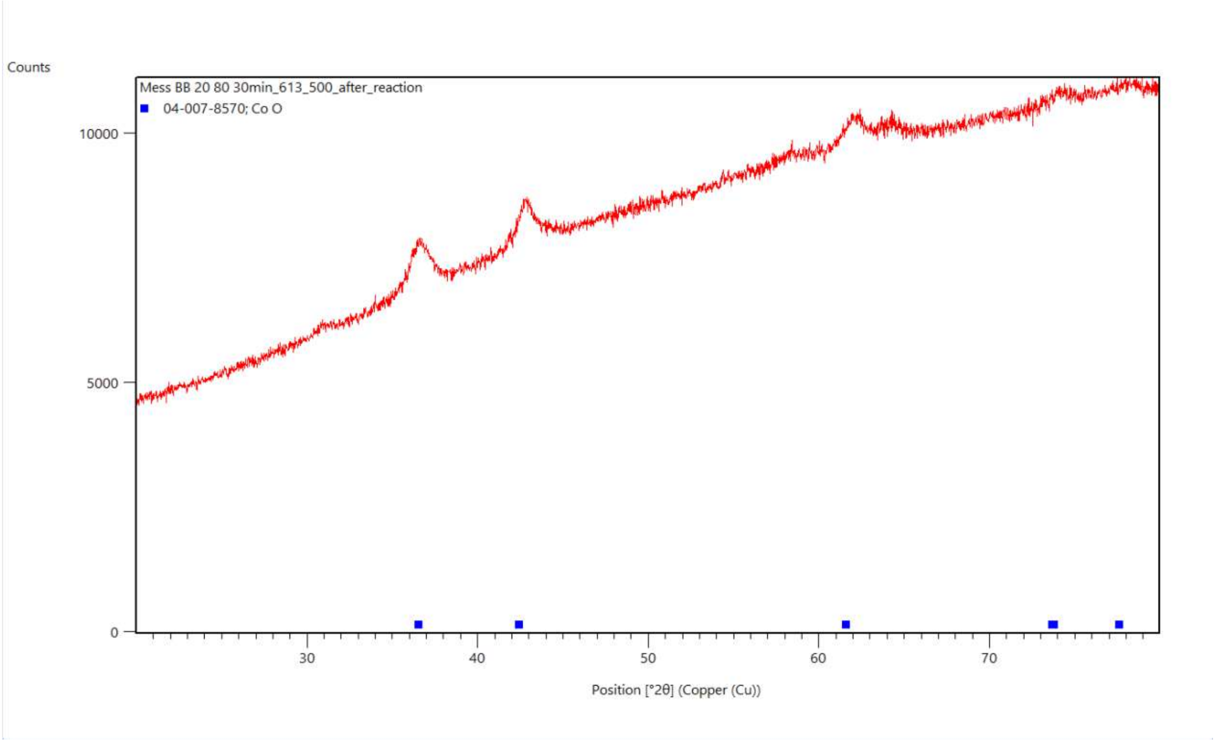

Figure 34: XRD of PG613 after reaction

The XRD pattern of the used $CrCo_2O_4$ catalyst reveals distinct diffraction peaks corresponding to CoO, indicating a phase transformation during the reaction. This suggests that the original $CrCo_2O_4$ phase underwent partial or complete reduction to (Cr,Co)O, driven by the reducing conditions present in the reaction environment.

Although the spinel peaks exhibit low intensity, traces of the characteristic spinel structure diffraction peaks are observable at 2θ positions of 31°, 58°, and 65°, providing additional confirmation of the phase transition process.

The observed peaks for CoO are sharp and well-defined, suggesting a crystalline CoO phase with moderate crystallite sizes. Minimal peak broadening is observed, which could imply that the CoO crystallites underwent limited sintering or structural reorganization during the reaction.

The reduction of $CrCo_2O_4$ to (Cr,Co)O aligns with expectations under reducing reaction conditions. The phase transformation to (Cr,Co)O and the lack of detectable crystalline chromium species raise questions about the specific role of chromium during and after the reaction. Chromium might function as a promoter or stabilizer during the initial reaction phase but may become structurally disordered under prolonged reaction conditions. This structural evolution could impact the catalyst's long-term stability, selectivity, and overall performance.

4.4.9 $NiCo_2O_4$ (PG617)

The XRD pattern (Figure 35) represents the analysis of the PG617 ($NiCo_2O_4$) catalyst after the completed reaction.

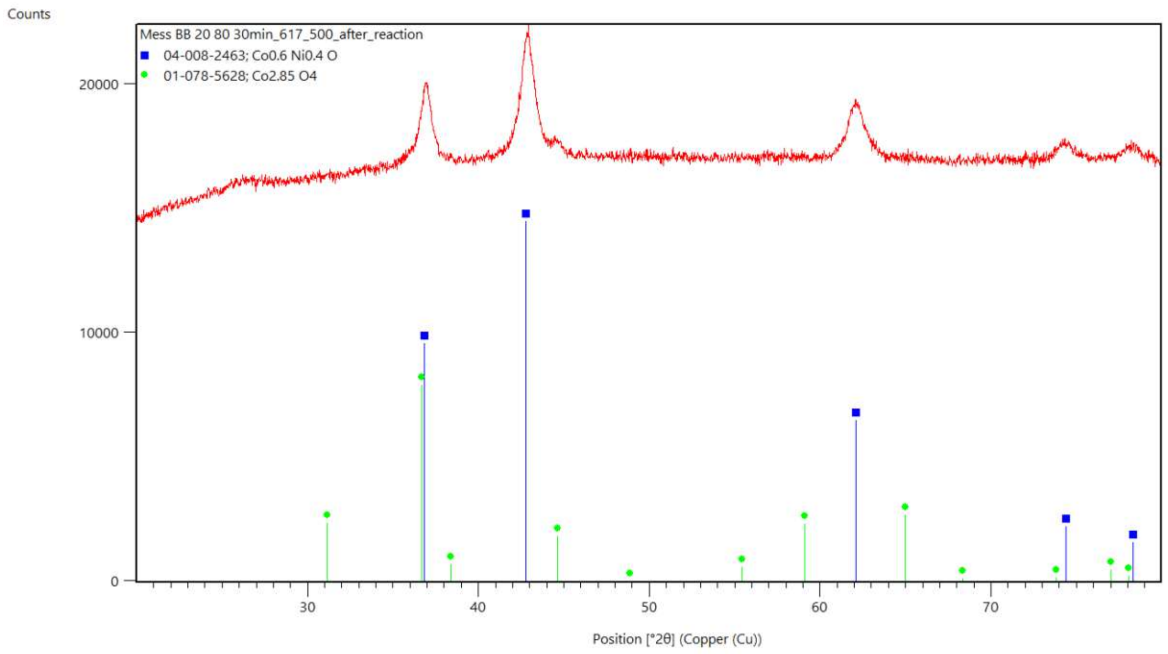

Figure 35: XRD of PG617 after reaction

The X-ray diffraction (XRD) analysis reveals a well-defined crystalline structure, as indicated by the sharp diffraction peaks in the observed pattern (red curve). The primary peaks at approximately $2\theta=45°$ are characteristic of a spinel structure, consistent with the $NiCo_2O_4$ phase.

Overlaying the experimental data are reference patterns for $Co_{0.6}Ni_{0.4}O$ (blue markers) and $Co_{2.85}O_4$ (green markers). The experimental diffraction peaks align predominantly with the $Co_{0.6}Ni_{0.4}O$ phase, confirming the partial preservation of the spinel structure after the reaction.

Notably, the sharpness of the diffraction peaks indicates that the catalyst maintains a high degree of crystallinity, with no significant peak broadening to suggest structural degradation or particle size reduction.

Additionally, a small and broad peak is observed at approximately 25° (2θ), which corresponds to amorphous carbon. This peak may be attributed to minor residues of glass wool or possibly carbon from the reactor. (S. R. Aravamuthan, 2013)

In summary, the $NiCo_2O_4$ catalyst remains structurally intact after the reaction, retaining its spinel configuration. The presence of minor cobalt-rich oxide phases may indicate partial phase segregation, which could be linked to the specific chemical environment or reaction dynamics. This suggests that the catalyst is structurally robust but may undergo slight compositional changes during the reaction process.

4.4.10 $CuCo_2O_4$ (PG619)

The X-ray diffraction (XRD) pattern for the $CuCo_2O_4$ catalyst after the reaction is presented in the Figure 36.

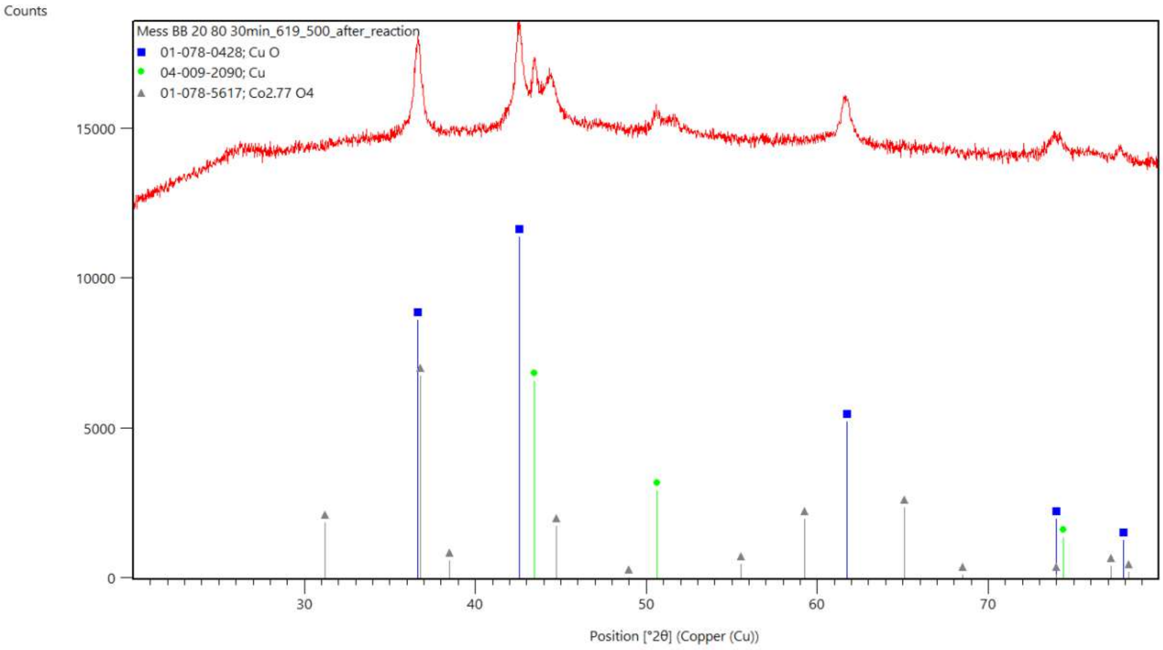

Figure 36: XRD of PG619 after reaction

After reaction, peaks associated with (Cu,Co)O (blue markers) are observed, suggesting the reduction of Co^{3+} during or after the reaction process. Additionally, peaks corresponding to metallic copper (green markers) are present, indicating the reduction of (Cu,Co)O to elemental copper in specific regions.

The sharp and well-defined diffraction peaks confirm that the material maintains a high degree of crystallinity, with no significant peak broadening to indicate structural degradation.

Overall, the XRD analysis reveals that the $CuCo_2O_4$ catalyst undergoes extensive phase transformation during the reaction. The presence of (Cu,Co)O and metallic Cu indicates that copper undergoes reduction, under the applied reaction conditions.

4.4.11 $ZnCo_2O_4$ (PG620)

The Figure 37 presents the X-ray diffraction (XRD) pattern of a $ZnCo_2O_4$ catalyst after reaction.

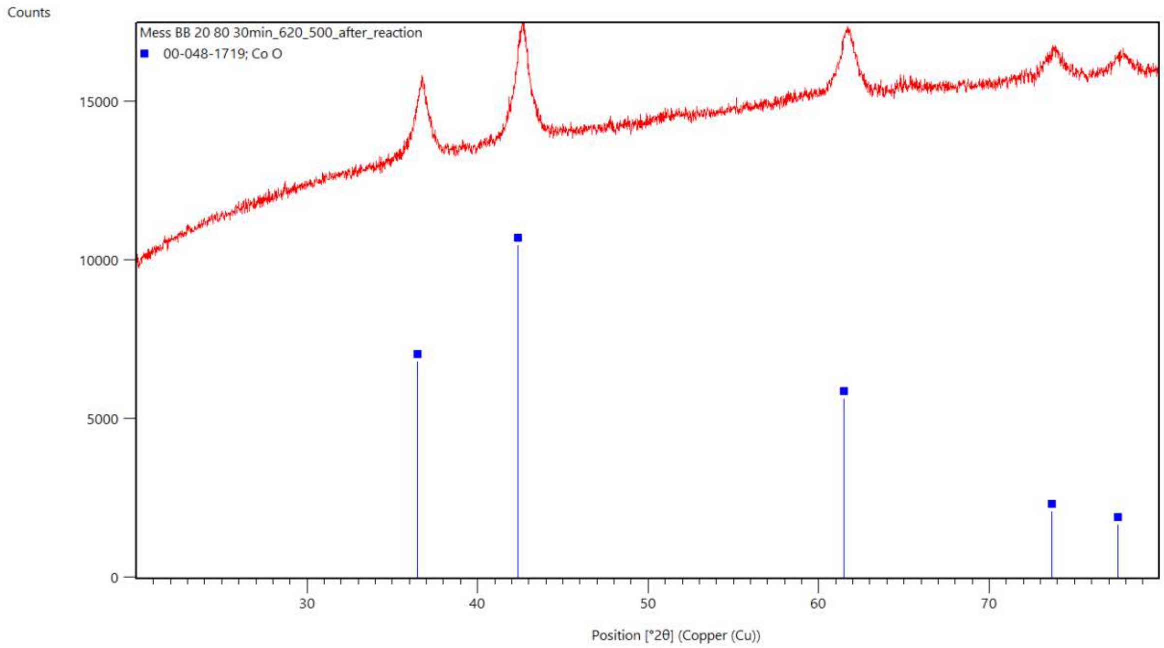

Figure 37: XRD of PG620 after reaction

The red diffraction pattern reveals broad peaks centered around 2θ positions of approximately 37°, 45°, and 60°, which align well with the most intense reflections of the (Zn,Co)O phase. These broad peaks suggest a degree of crystallinity in the (Zn,Co)O phase.

Overall, the comparison with the CoO reference data confirms the retention of cobalt oxide as a crystalline phase. Its lack of crystallinity or minimal lattice distortion may render Zn undetectable by XRD.

4.5 Comparison

4.5.1 Calcination temperature

Figure 38 presents five graphs all of which include three profiles: the grey curve represents temperature, plotted on the right y-axis, while the blue and purple curves correspond to Co_3O_4 samples calcined at 200°C and 500°C. Both catalytic tests were performed under identical conditions, with an isopropanol-to-oxygen ratio of 2:1, two reaction cycles at 400°C (each held for 30 minutes), and a heating rate of 2°C/min.

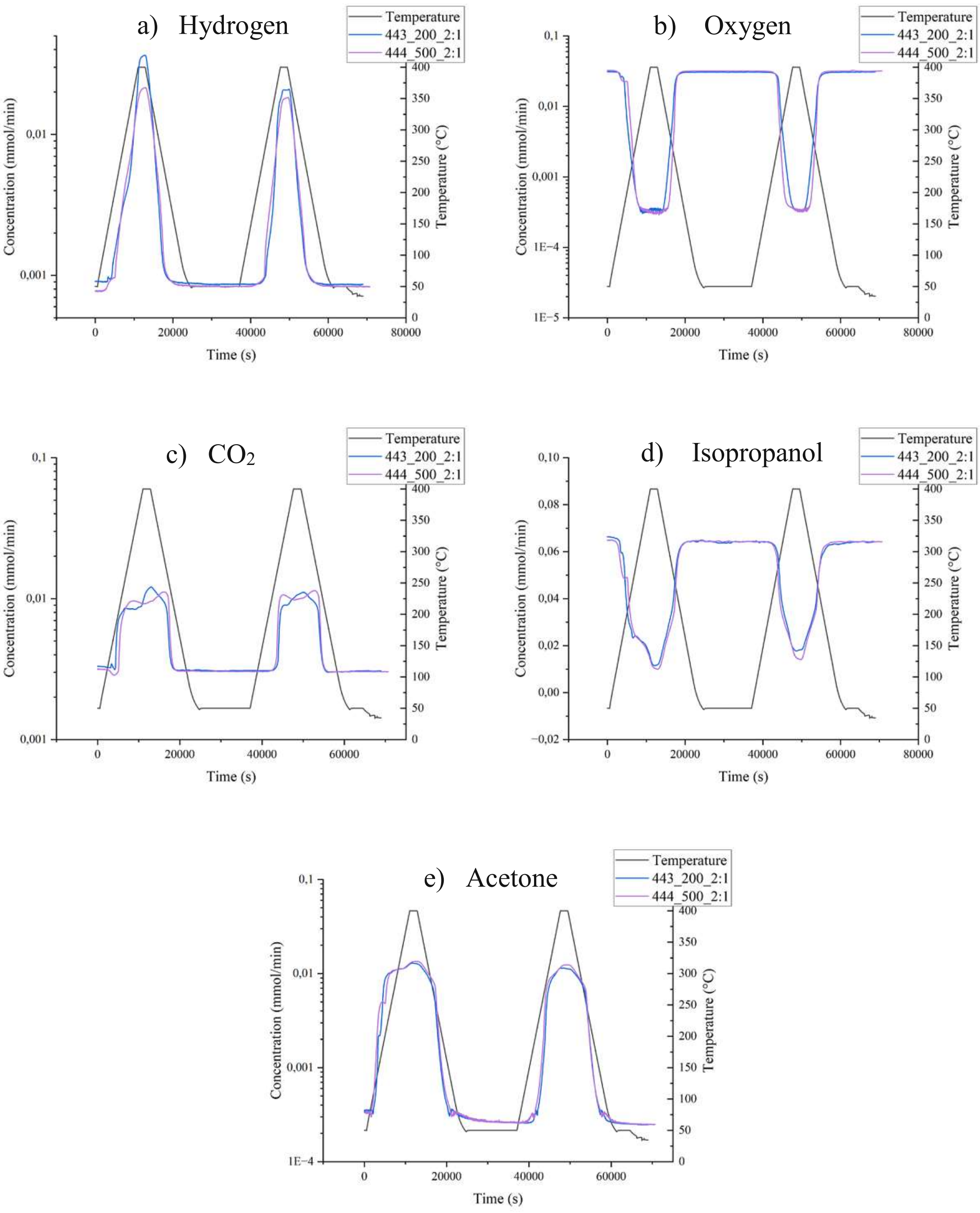

Figure 38: Comparison calcination temperature on Co_3O_4 (2:1 isopropanol-to-oxygen ratio) with hydrogen (a), oxygen (b), CO_2 (c), isopropanol (d) and acetone (e) signal comparison

While the signals for oxygen, isopropanol, and acetone show no significant differences between the two samples, the CO_2 signals exhibit notable variations in concentration and behaviour during the temperature-holding phase.

The hydrogen signal demonstrates a higher concentration for the Co_3O_4 sample calcined at the lower temperature (200°C). In contrast, the CO_2 signal shows distinct behaviour patterns for the two samples, which show a similar total production, but different signal profiles.

These observations indicate that the calcination temperature of Co_3O_4 somewhat influences the hydrogen and CO_2 production.

Overall, although differences are observed, they are not as significant or critical compared to other factors influencing the performance of the catalytic reaction. The most significant observation, although not directly related to the calcination temperature, is that the conversions and yields are lower in the second cycle compared to the first. This indicates a decline in the catalyst's activity over time and/or with repeated usage., which is more pronounced for hydrogen over the sample calcined at lower temperatures.

4.5.2 Isopropanol-to-oxygen ratio

Figure 39 compares two catalytic reactions conducted with different isopropanol-to-oxygen ratios (1:1 and 2:1) using a standard Co_3O_4 catalyst. The catalyst was calcined at 500°C and tested under standard reaction conditions, consisting of two cycles at 400°C with each cycle lasting 30 minutes. The IPA concentration was kept constant, whereas the oxygen concentration was varied.

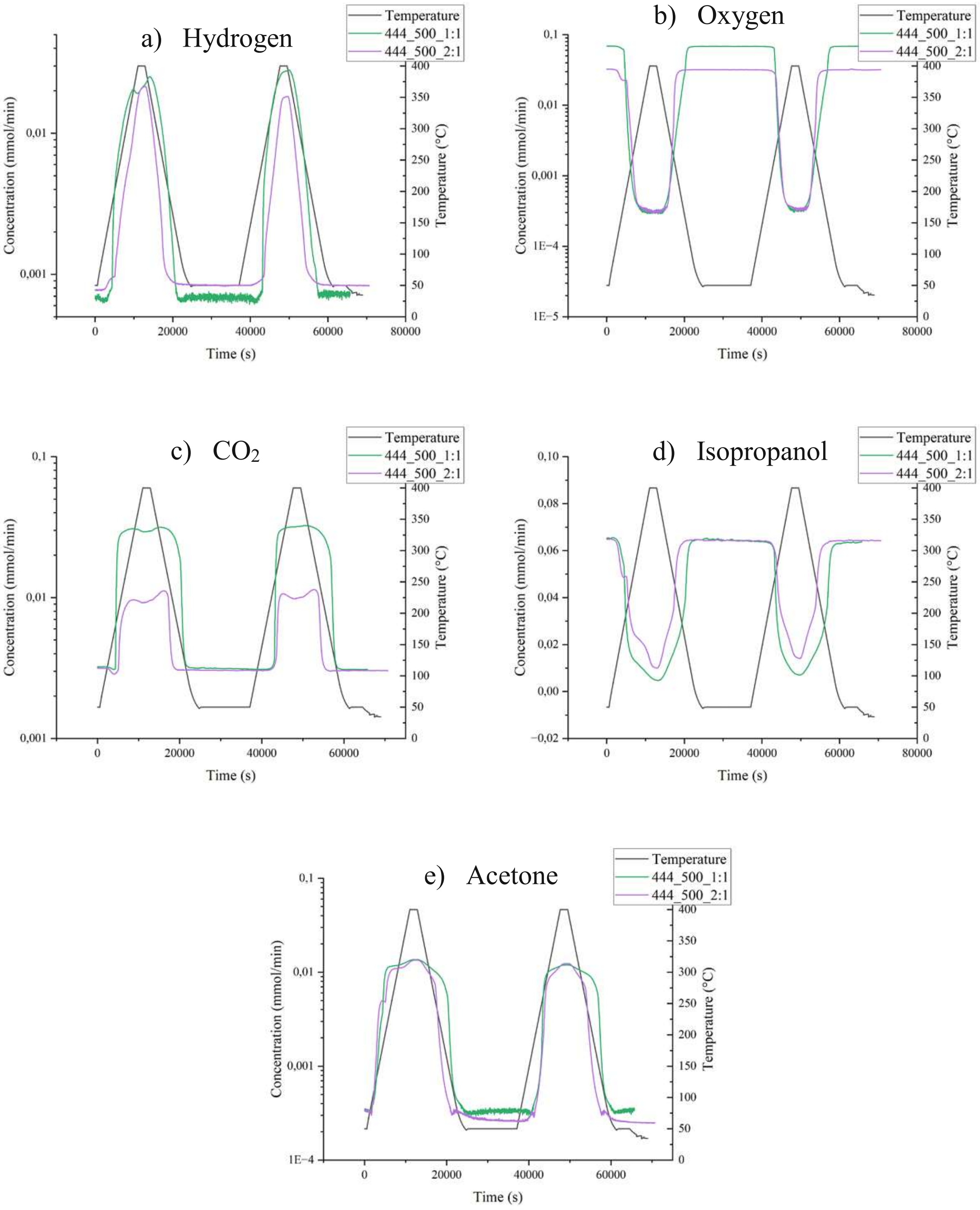

Figure 39: Comparison isopropanol-to-oxygen ratio on Co_3O_4 with hydrogen (a), oxygen (b), CO_2 (c), isopropanol (d) and acetone (e) signal comparison

In terms of reactant behaviour, the oxygen concentration profiles for both reactions are nearly identical, indicating complete oxygen consumption in both cases. However, the isopropanol concentration decreases more significantly in the reaction with the 1:1 ratio. The availability of more oxygen in the 1:1 ratio allows a larger amount of isopropanol to react, leading to relatively lower consumption in the 2:1 case.

The reaction products show more pronounced differences. In the case of acetone, the maximum concentration is nearly identical for both reactions, but a broader acetone peak is observed for the 1:1 ratio. This broadening suggests that the reaction continues even at the end of the holding phase, as cooling begins. This can be explained by the presence of residual reactants in the system, which allows further acetone formation during the cooling process. This is likely due to the increased oxygen availability, which reduces the stability of surface species, causing them to oxidize to CO_2.

The hydrogen concentration for the 1:1 ratio is slightly higher and more intense at lower temperatures compared to the 2:1 ratio, indicating that hydrogen production is enhanced or prolonged when more oxygen is available. This is somewhat counterintuitive since an excess of oxygen would rather favor a oxidative dehydrogenation over hydrogenation or even the total oxidation to CO_2. However, this observation could indicate an enhanced restoration of active oxygen sites or species. The most striking difference is observed in the CO_2 concentration profiles. While the trends in concentration behaviour are nearly the same for both ratios, the total CO_2 concentration produced in the 1:1 ratio reaction is almost twice as high as that produced in the 2:1 ratio reaction.

These results indicate that increasing the oxygen flow primarily favors the complete oxidation of isopropanol to CO_2 rather than enhancing the synthesis of acetone. The similar acetone production profiles for both reactions, coupled with the significant increase in CO_2 production in the 1:1 ratio, suggest that higher oxygen availability shifts the reaction pathway toward full oxidation rather than acetone formation. This highlights the influence of the isopropanol-to-oxygen ratio on product selectivity.

4.5.3 Nanocast catalysts: Hydrogen

Figure 40 compares the hydrogen concentration produced during catalytic reactions using various MCo_2O_4 catalysts.

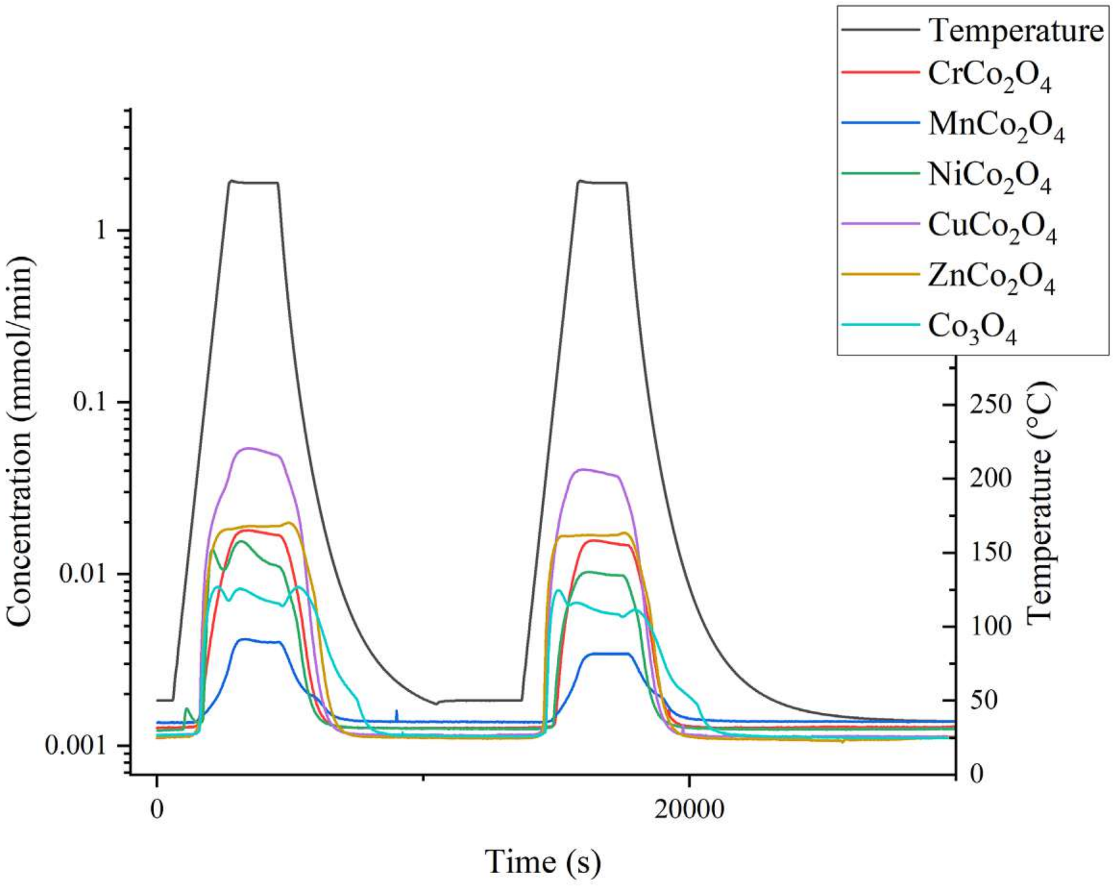

Figure 40: Comparison of the hydrogen production of nanocast catalysts

Analyzing the cycles reveals the following behaviour: the first and the second cycle show a consistent plateau, along with distinct signal increases and decreases for nearly all compositions, except for Co_3O_4 (both cycles) and $NiCo_2O_4$ (first cycle). The deviation, between the two cycles for $NiCo_2O_4$, suggests that the catalyst undergoes structural changes or loses key structural properties during the first cycle, which impairs its performance, in particular at lower temperatures.

The alteration of the structural properties due to the heating process results in a continuous reduction in activity at low temperatures with each cycle. This hypothesis is further supported by the XRD data discussed in Chapter 4.4, which indicates structural transformations.

Since hydrogen production serves as an indicator of reaction selectivity, the catalysts can be ranked by efficiency in the following order: $CuCo_2O_4$ > $ZnCo_2O_4$ ~ $CrCo_2O_4$ > $NiCo_2O_4$ > Co_3O_4 > $MnCo_2O_4$, with $MnCo_2O_4$ being the least effective in terms of hydrogen production. This ranking highlights the variation in catalytic performance based on the composition of the AB_2O_4 catalysts.

4.5.4 Nanocast catalysts: Oxygen

Figure 41 presents a comparison of oxygen consumption by the previously mentioned catalysts.

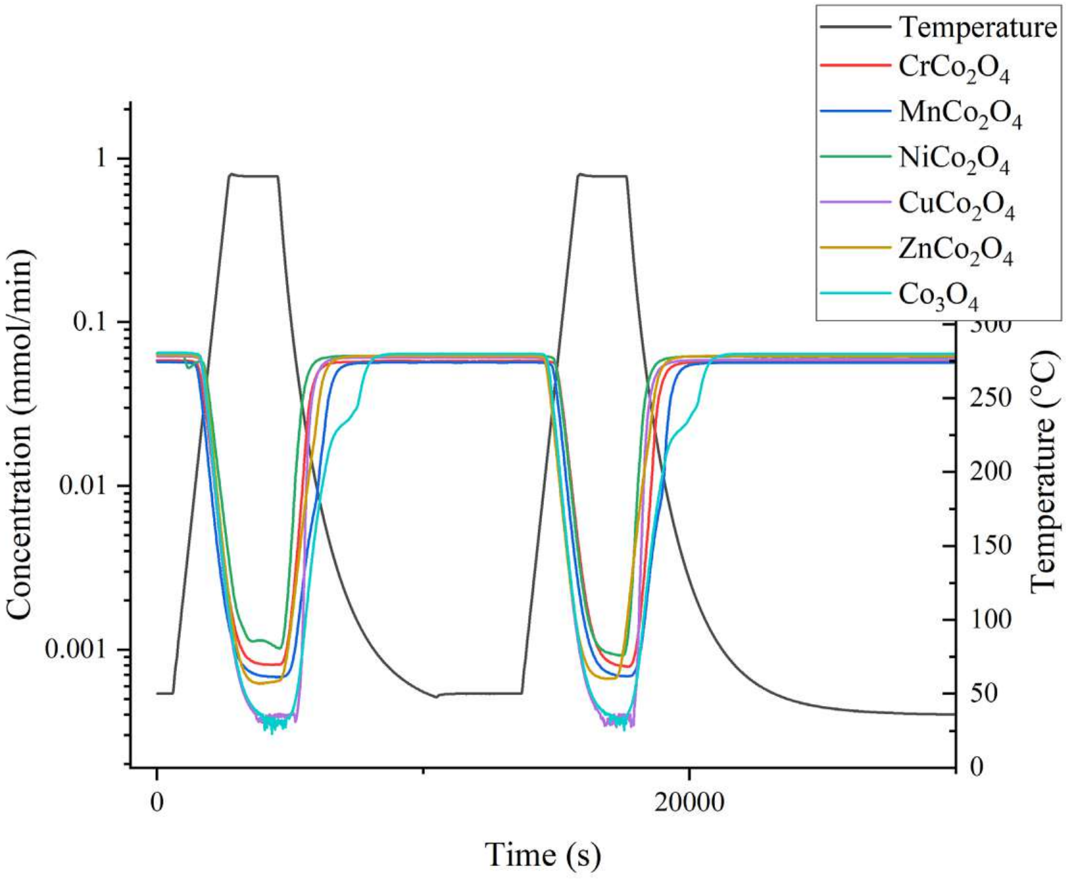

Figure 41: Comparison of the oxygen consumption of nanocast catalysts

The oxygen consumption appears to be nearly identical for the Cr-, Zn-, and Mn-based catalysts, whereas the Ni-based catalyst exhibits the lowest oxygen consumption. Notably, both the Co_3O_4 catalyst and the $CuCo_2O_4$ catalyst demonstrate complete oxygen consumption, highlighting their distinct behaviour compared to the other catalysts.

4.5.5 Nanocast catalysts: CO_2

Figure 42 illustrates the CO_2 concentration profile for the different catalysts.

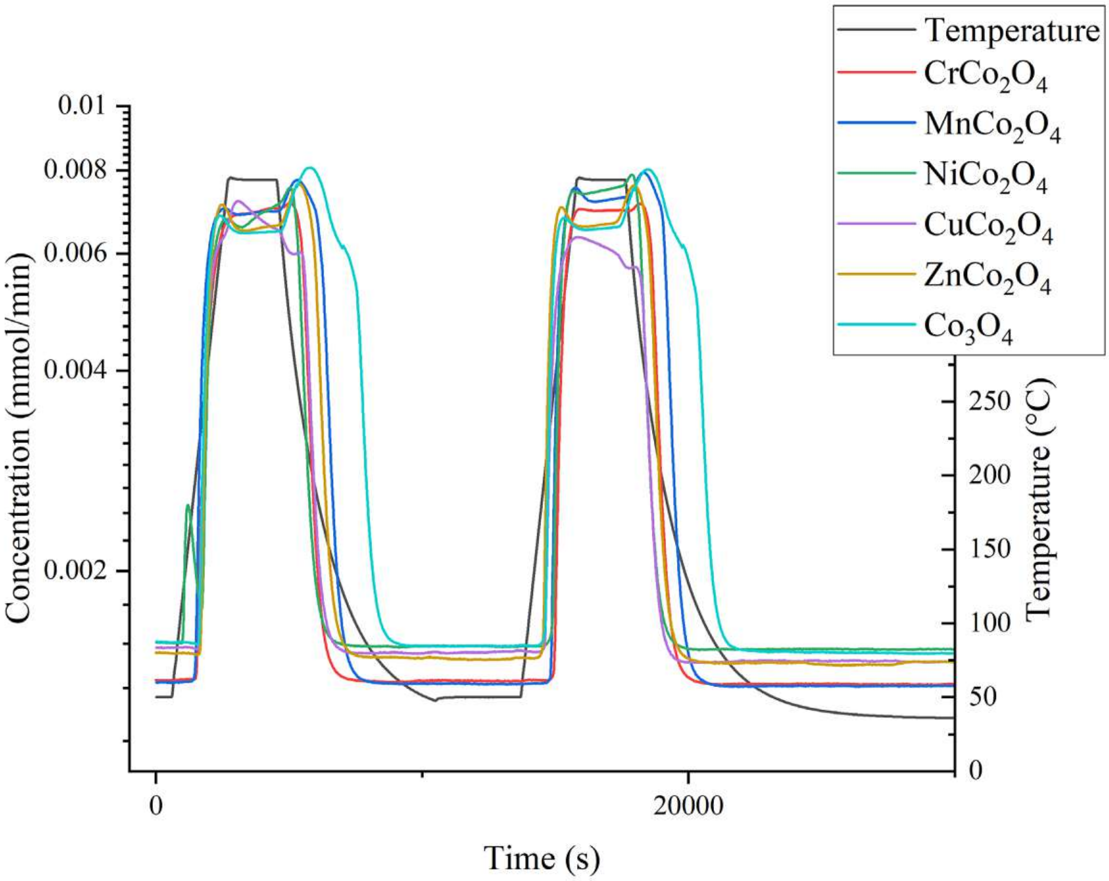

Figure 42: Comparison of the CO_2 production of nanocast catalysts

A direct comparison reveals no significant differences between the catalysts in terms of maximum CO_2 production during the reaction at the maintained temperature. However, an intriguing observation is that CO_2 production appears to continue even as the reaction temperature decreases. This hysteresis could be attributed to the accumulation of reactants in the system that continue to react even after the primary reaction has concluded.

4.5.6 Nanocast catalysts: Isopropanol

Figure 43 depicts the isopropanol consumption observed during testing of the different catalysts.

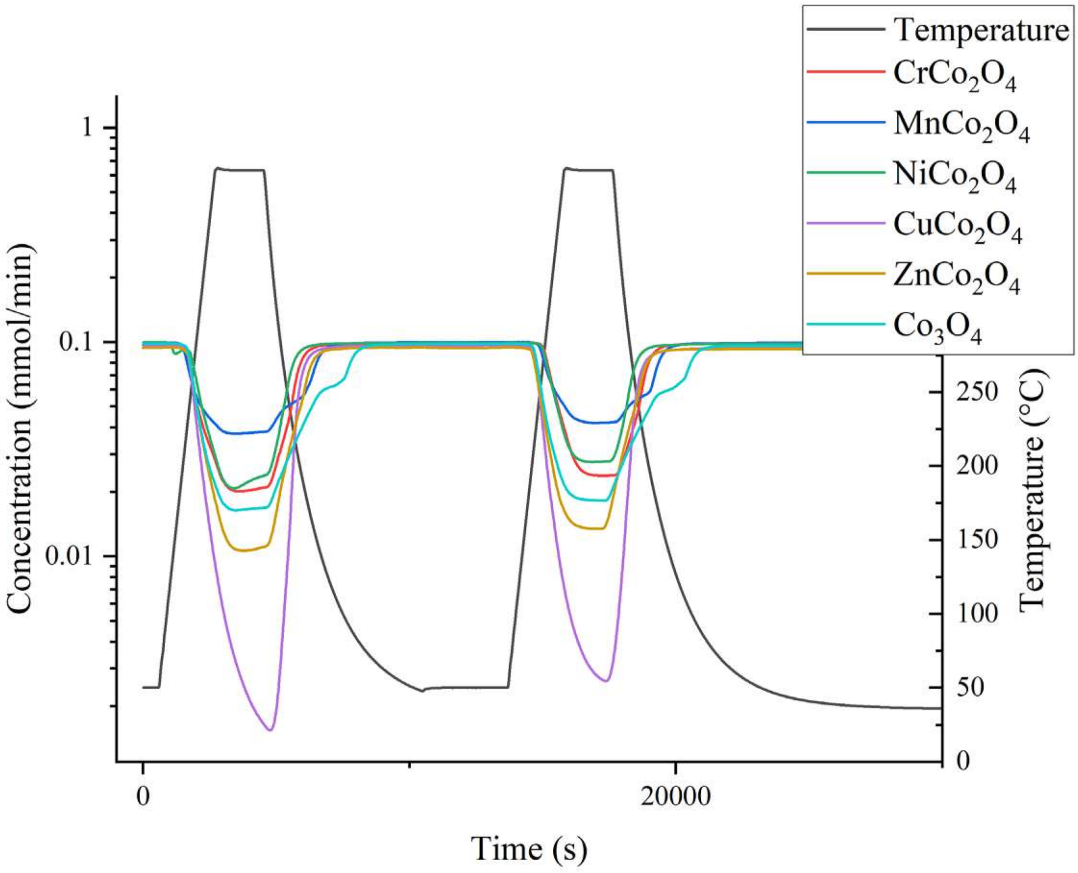

Figure 43: Comparison of the isopropanol consumption of nanocast catalysts

When considering the results from Figure 40, which ranked the catalysts by hydrogen production efficiency in the order $CuCo_2O_4$ > $CrCo_2O_4$ ~ $ZnCo_2O_4$ > $NiCo_2O_4$ > Co_3O_4 > $MnCo_2O_4$, the trends in Figure 43 show a similar pattern. The $CuCo_2O_4$ catalyst exhibits the highest isopropanol consumption, while the $MnCo_2O_4$ catalyst consumes significantly less. Among the other four catalysts, there are observable differences in isopropanol consumption; however, these values fall within a relatively narrow range.

4.5.7 Nanocast catalysts: Acetone

The final Figure 44 of this chapter compares the acetone concentration profiles for the different catalyst compositions.

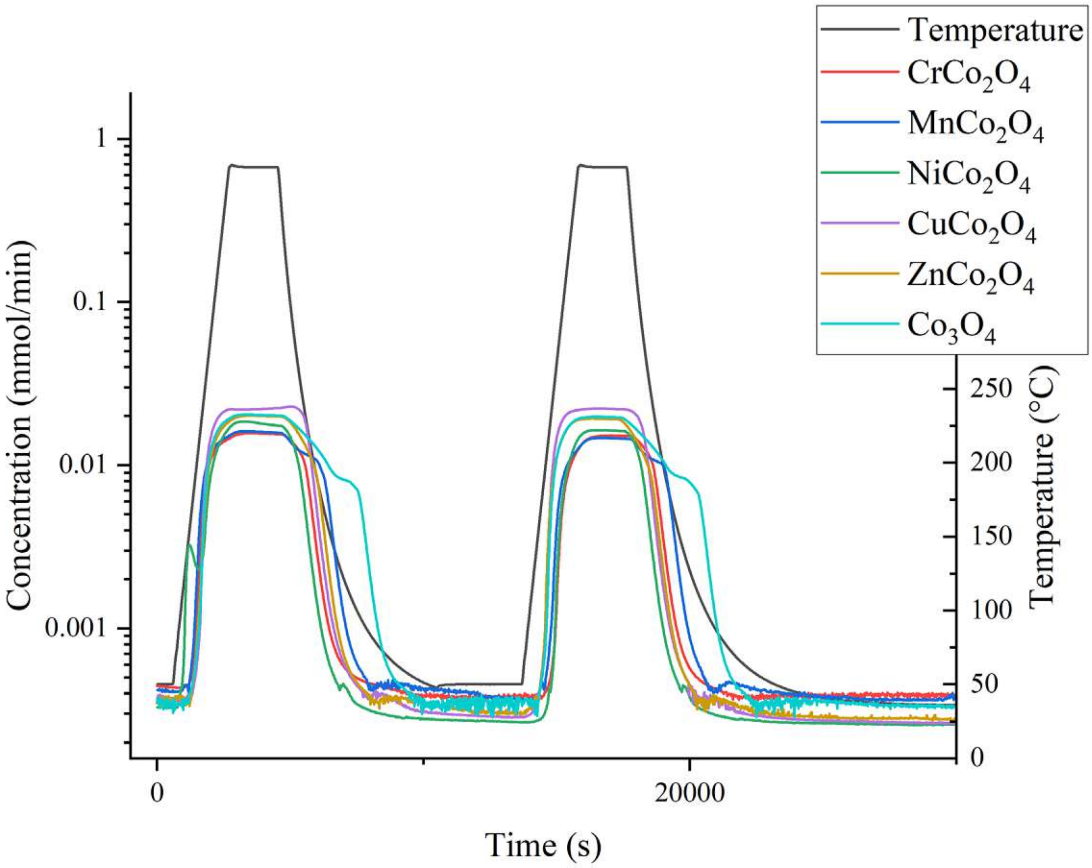

Figure 44: Comparison of the acetone production of nanocast catalysts

The acetone concentration curves exhibit a similar trend to the CO_2 concentration curves, with the various catalysts displaying comparable behaviour. The only two notable differences being that the Co_3O_4 catalyst appears to be the only catalyst that continues producing acetone and, furthermore, CO_2 even after the cooling process has begun and that only $NiCo_2O_4$ shows a characteristic shoulder (at ~150°C) in the first cycle

4.6 Selectivity, conversion, yield

The following chapter presents a comparison of the yields, conversions, and selectivities of the tested catalysts, with the results plotted as a function of temperature. The data points were plotted against the corresponding temperatures.

4.6.1 Yield

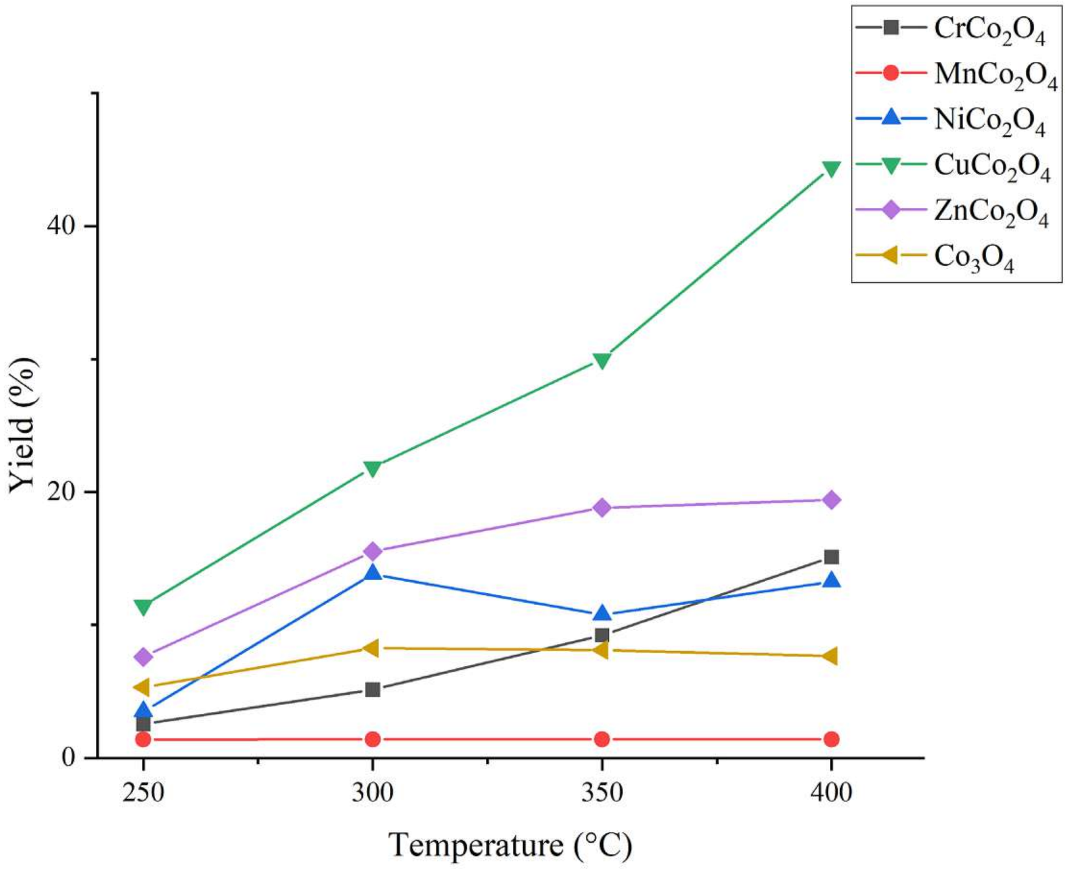

Figure 45: Comparison nanocast catalysts: Yield H_2

Figure 45 reveals that the $CuCo_2O_4$ catalyst consistently produces the highest yield of H_2 across all temperatures, thus confirming its superior catalytic efficiency. In contrast, $MnCo_2O_4$ demonstrates the lowest yield throughout the entire temperature range, which aligns with its previously observed low isopropanol consumption and hydrogen production efficiency.

$CrCo_2O_4$ and Co_3O_4 display intermediate yields, with $ZnCo_2O_4$ demonstrating slightly superior performance. While the H_2 yields of $MnCo_2O_4$ and Co_3O_4 remain relatively stable, those of $CuCo_2O_4$ and $CrCo_2O_4$ appear to increase proportionally with temperature. The observed instable behaviour of the $NiCo_2O_4$ graph may result from the selected temperature data points coinciding with the previously identified shoulder features.

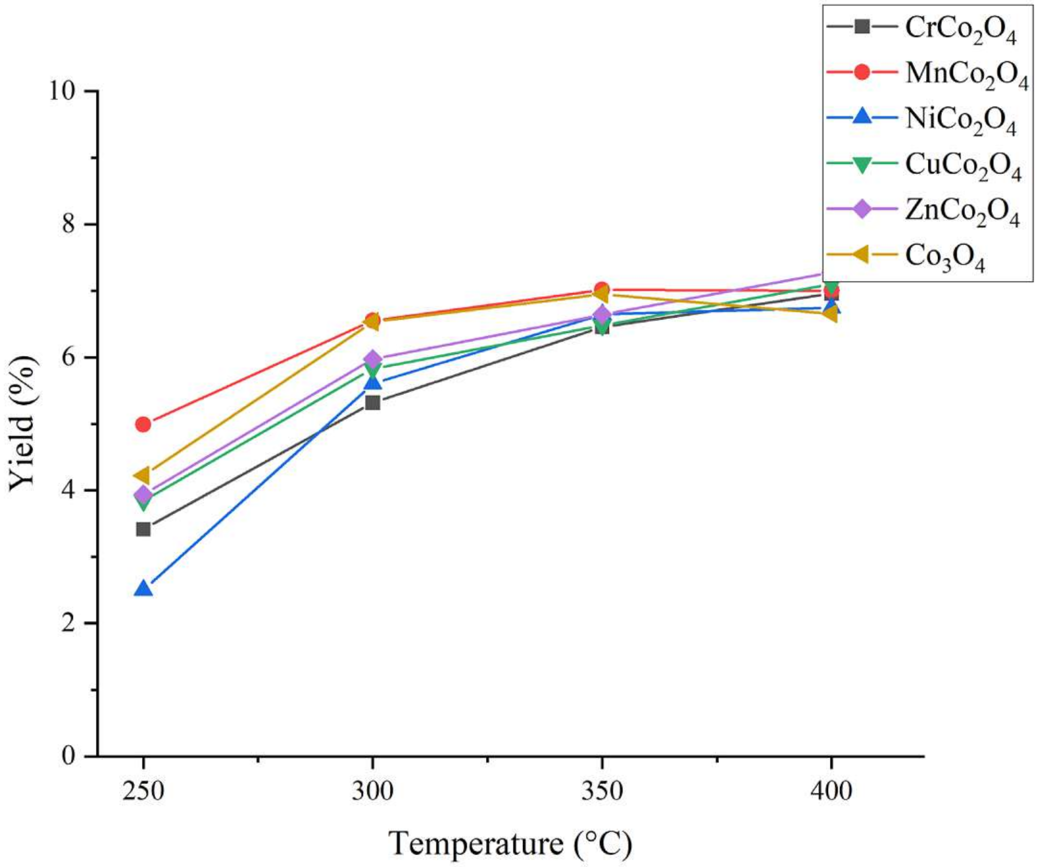

Figure 46: Comparison nanocast catalysts: Yield CO_2

A comparison of Figure 45 and Figure 46 reveals that the order of hydrogen yields does not correspond to the yields calculated for CO_2 production. This observation suggests the possibility of differences in selectivity among the various catalysts.

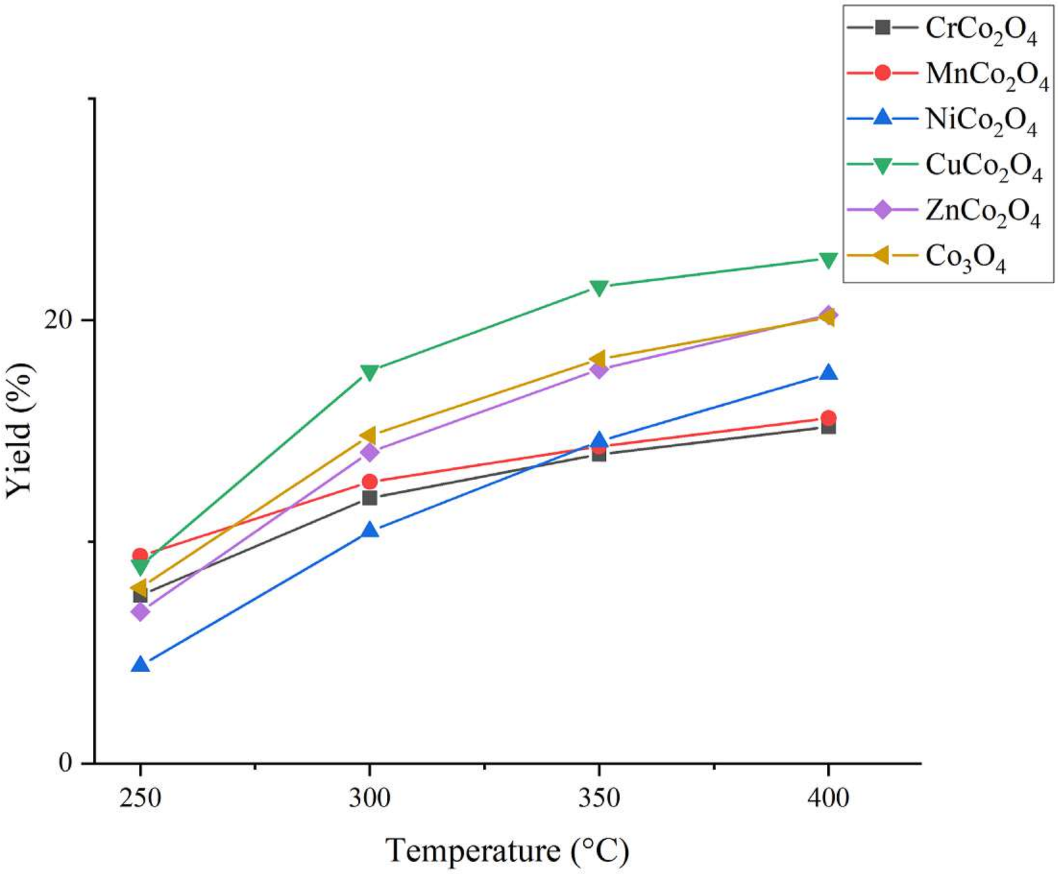

Figure 47: Comparison nanocast catalysts: Yield acetone

While the yields of hydrogen and CO_2 production provide valuable insights into the general trends, performance, and selectivity of the catalysts, the most critical factor is the yield of acetone, as this is the desired product. The data shows a clear trend of increasing acetone production with rising temperature. Similar to the previously discussed hydrogen production, the Cu-based catalyst exhibits the highest acetone production efficiency, followed by the Zn-based and pure cobalt catalysts, which display comparable performance. Notably, while the Mn- and Cr-based catalysts demonstrate relatively constant yields across all temperatures, the yields of the other catalysts increase significantly with temperature.

4.6.2 Conversion

Figure 48 and Figure 49 depict the average conversion levels of isopropanol and oxygen across the various catalysts studied. These data sets allow for a detailed comparison, revealing critical insights into the relationship between the conversion processes of these reactants.

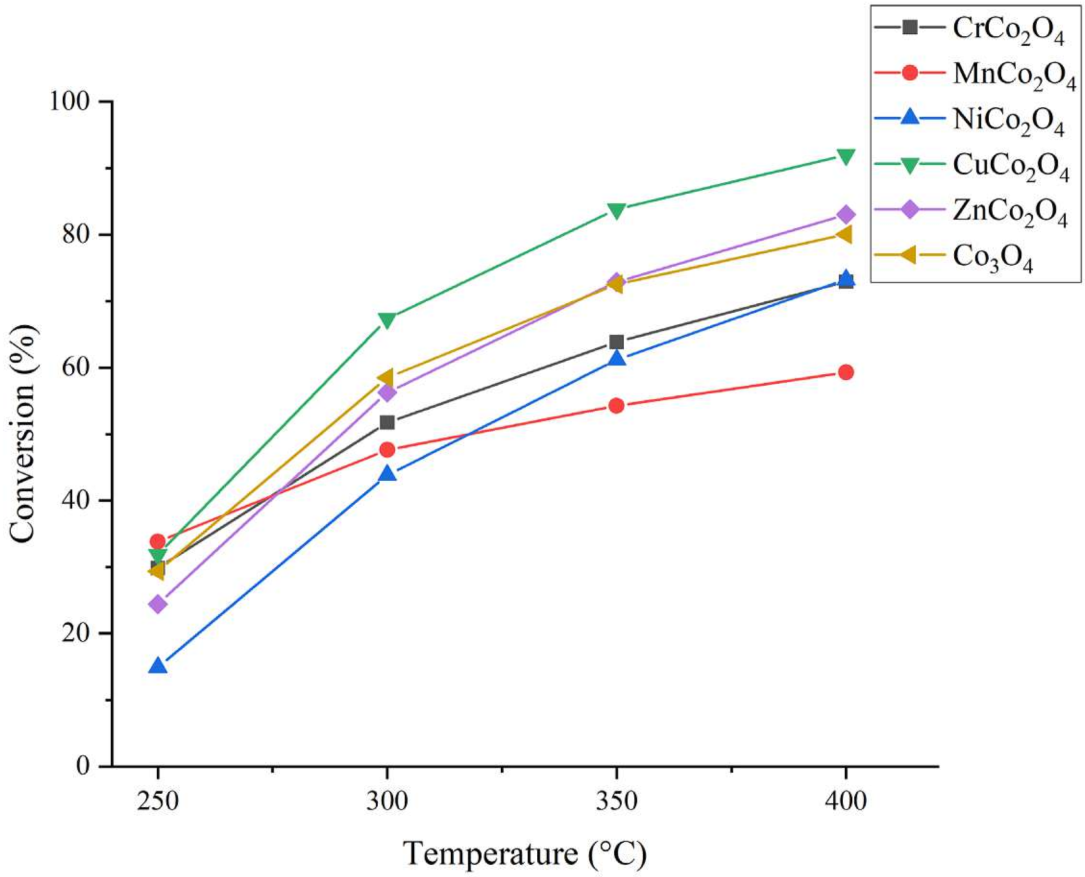

Figure 48: Comparison nanocast catalysts: Conversion isopropanol

A key observation is the interdependence of isopropanol and oxygen in acetone production. Both reactants play essential roles in the process; however, an imbalance, particularly with oxygen being consumed in excess of isopropanol, leads to the formation of significant quantities of byproducts. This trend aligns with the results obtained, as the conversion profiles reflect distinct catalytic behaviours.

Upon comparing Figure 48 and Figure 49 with Figure 41 and Figure 43, one would have expected reversed results, as the consumption of isopropanol varied significantly across the different catalysts, while the oxygen consumption appeared to be relatively similar for higher temperatures.

These findings substantiate the hypothesis that analyzing the conversion trends of isopropanol and oxygen provides valuable insights into catalytic selectivity. Specifically, catalysts that exhibit balanced consumption of isopropanol and oxygen tend to favor acetone production, whereas an inconsistent oxygen consumption is indicative of pathways leading to byproduct formation.

Our results are particularly intriguing as analogous experiments conducted by Falk et al. (T. Falk, 2022) yielded contrasting results, where the tested catalysts demonstrated isopropanol conversion performance ranked as Co_3O_4 ~ Ni-Co_3O_4 > Cu-Co_3O_4> Mn-Co_3O_4> Cr-Co_3O_4, whereas in our case, the isopropanol conversions appear to be rather different: $CuCo_2O_4$ > Co_3O_4 ~ $ZnCo_2O_4$ > $CrCo_2O_4$ > $NiCo_2O_4$ > $MnCo_2O_4$.

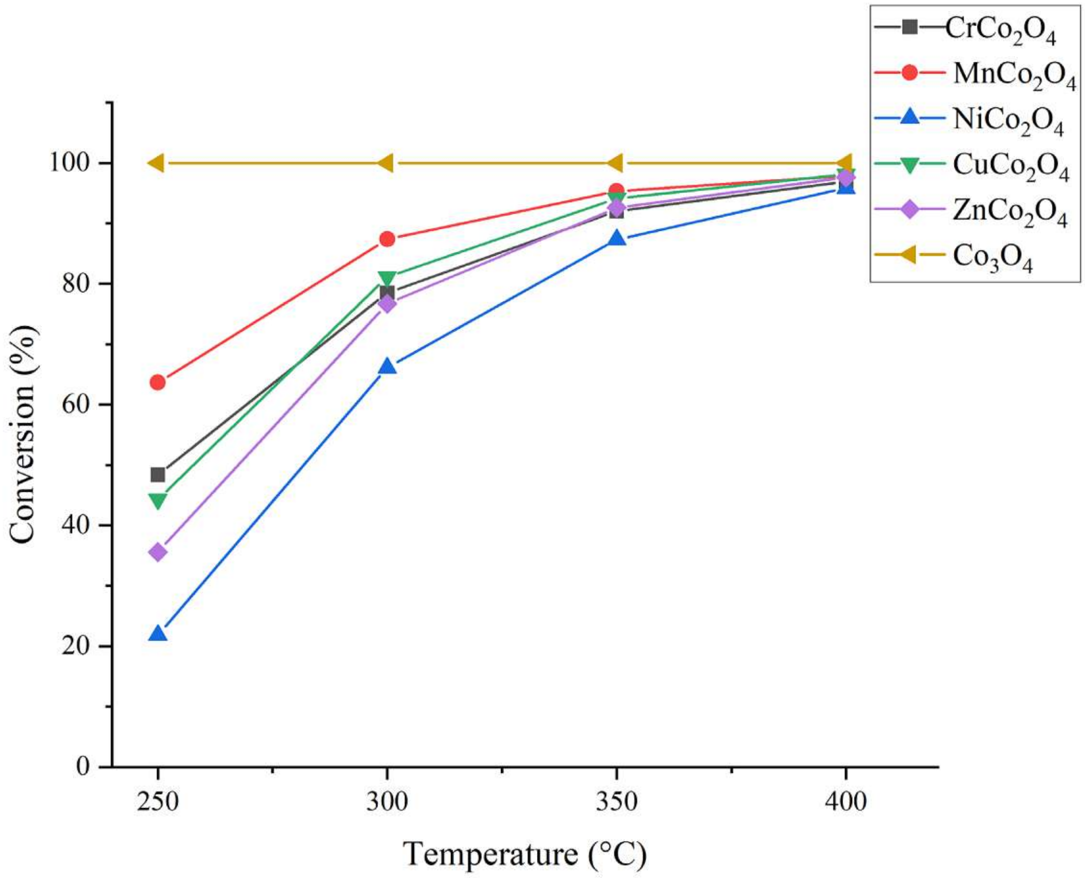

Figure 49: Comparison nanocast catalysts: Conversion oxygen

Figure 49 illustrates a clear trend of increasing oxygen conversion with rising temperature. Notably, the Co_3O_4 catalyst achieves 100% oxygen conversion, which is particularly intriguing given its relatively low hydrogen yield. This observation could be an explanation for the high CO_2 yield for this catalyst, which is comparable to that of the Mn-based catalyst.

4.6.3 Efficiency

Figure 50 illustrates the efficiency of the catalytic tests and offers valuable insights into the reaction's selectivity and overall performance.

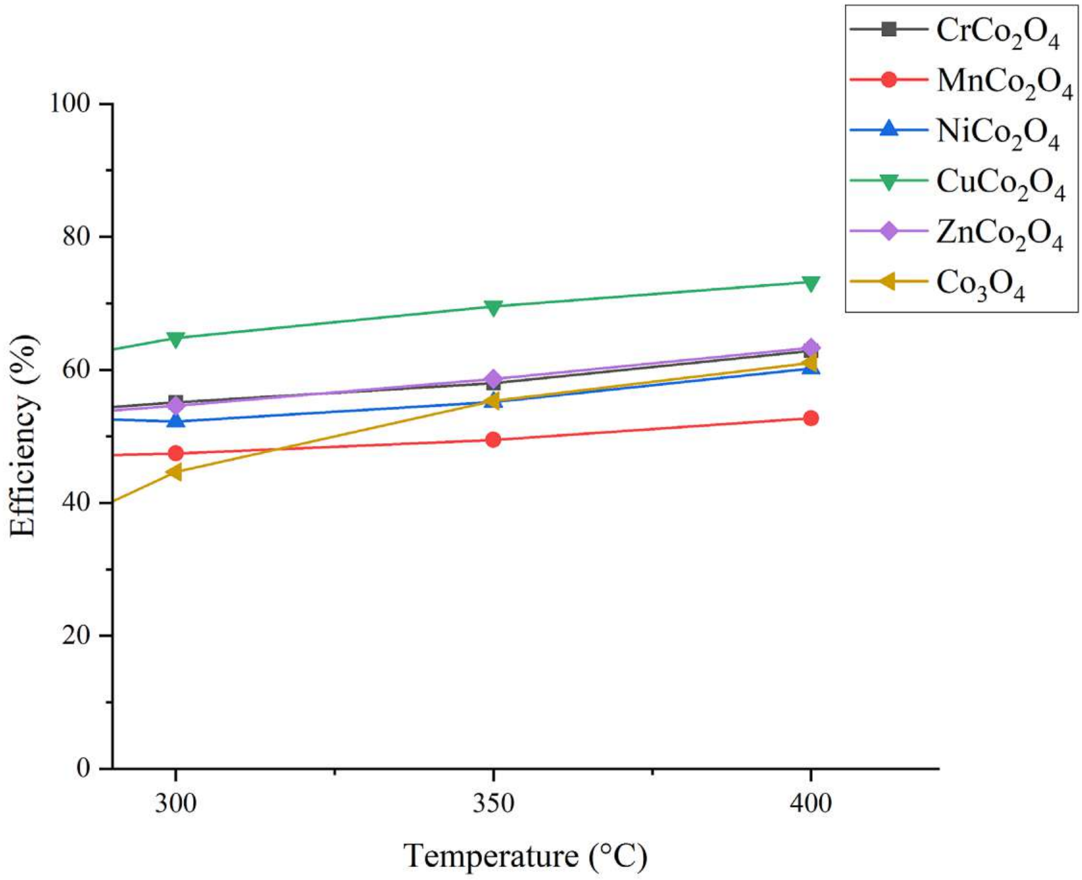

Figure 50: Comparison: Efficiency

The ideal outcome would be an efficiency of 100%, indicating a perfectly stoichiometric reaction in which oxygen and isopropanol are consumed precisely in their stoichiometric ratio. Another theoretical outcome, although not observed in this case, would be an efficiency exceeding 100%, suggesting that isopropanol might undergo reactions independent of oxygen, such as byproduct formation.

In this study, the observed efficiencies are below the theoretical maximum, implying that more oxygen is consumed than expected. This discrepancy could indicate overoxidation, such as the formation of CO or CO_2, or oxygen loss due to side reactions. Among the catalysts tested, the Mn-based catalyst exhibits the lowest efficiency, while the Cu-based catalyst demonstrates the highest efficiency.

4.6.4 Selectivity

Figure 51 presents a comparison of hydrogen selectivity among the different catalysts.

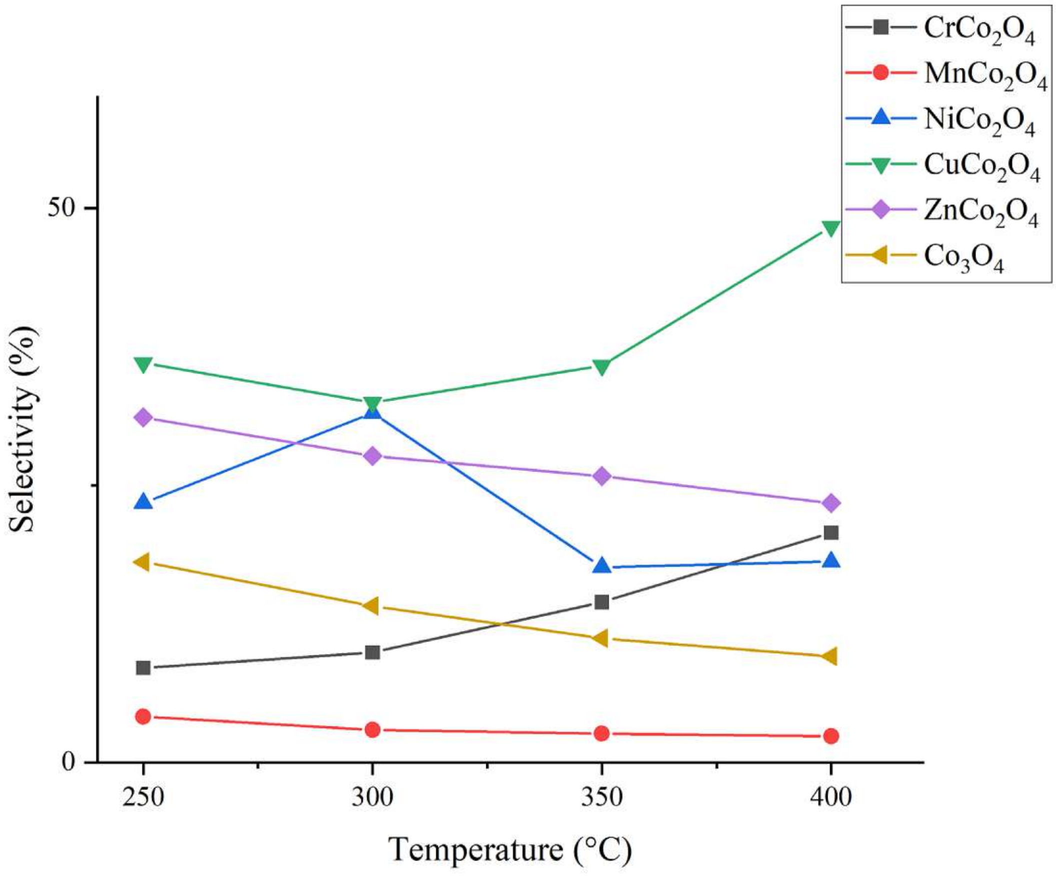

Figure 51: Comparison nanocast catalysts: Selectivity H_2

Considering the discussions and observations outlined in the previous chapters, the results presented in Figure 51 align well with the anticipated trends and assumptions. These findings are consistent with earlier conclusions, further substantiating the identified patterns.

As expected, the $CuCo_2O4$ catalyst exhibits the highest selectivity for H_2 and especially at temperatures exceeding 350°C, whereas the $MnCo_2O_4$ catalyst demonstrates the lowest overall H_2 selectivity.

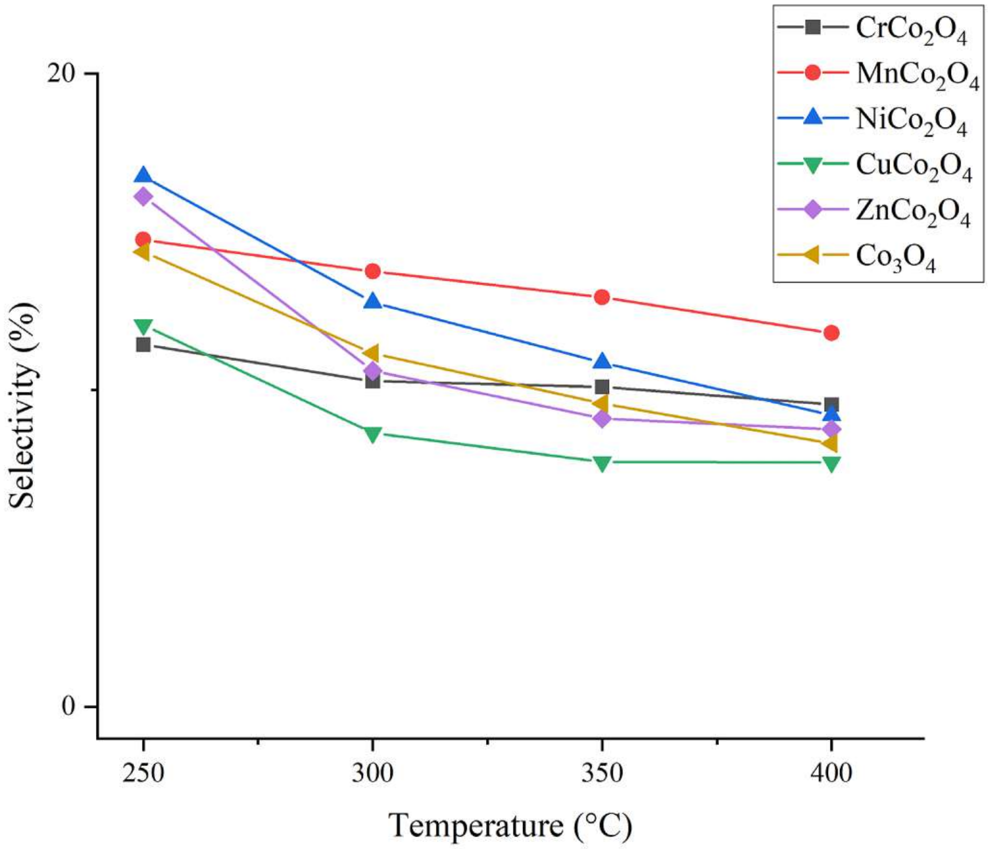

Figure 52: Comparison nanocast catalysts: Selectivity CO_2

Figure 52 reveals a significant trend: CO_2 selectivity decreases at lower temperatures and remains relatively constant at temperatures above 300°C for the Cu-, Cr- and Zn-catalyst. Furthermore, the $MnCo_2O_4$ catalyst demonstrates the highest CO_2 selectivity, whereas the $CuCo_2O_4$ catalyst exhibits the lowest values. This observation is consistent with previously discussed trends and the hypothesis that the Cu-based catalyst is likely to exhibit the highest overall acetone selectivity.

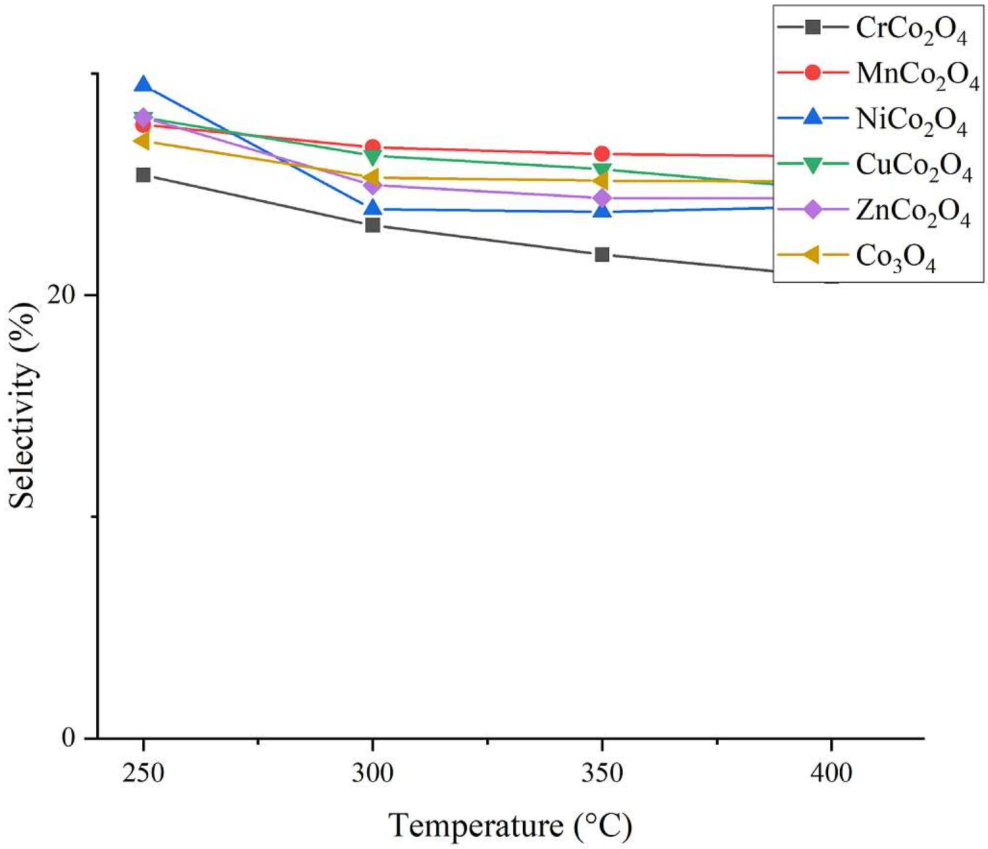

Figure 53: Comparison nanocast catalysts: Selectivity acetone

Although the trends discussed thus far suggested that acetone selectivity might increase with temperature, this pattern is not evident in Figure 53. A possible explanation is the formation of additional C-containing products such as CO, which were not quantified in this work. Instead, the figure displays a ranking of the catalysts ($MnCo_2O_4$ > $CuCo_2O_4$ > Co_3O_4 > $ZnCo_2O_4$ > $NiCo_2O_4$ > $CrCo_2O_4$), which is rather unexpected, given that the Mn-based catalyst demonstrated the poorest performance overall in terms of hydrogen and acetone yields, isopropanol conversion, and hydrogen selectivity. A potential explanation could be that the catalyst produces relatively low concentrations of products but with a high selectivity. This hypothesis could be further explored through the quantification of the water produced.

5 Conclusion and future perspectives

The primary aim of this master's thesis was to investigate the catalytic performance of Co-based spinel oxides in isopropanol oxidation reactions using a continuous solid-gas flow reactor system. This was achieved through a systematic exploration of various catalysts (MCo_2O_4 spinel oxides) under diverse reaction conditions, including variations in temperature, reaction duration, heating rate, gas flow rates, the number of reaction cycles, and calcination temperatures of the catalysts. Advanced characterization methods, such as temperature-programmed reaction (TPR) analysis, x-ray diffraction (XRD) and N_2-physisorption by the Brunauer-Emmett-Teller (BET) theory, were employed to gain deeper insights into the structural and mechanistic aspects of the catalytic processes.

The research was centered on two key objectives: (1) an in-depth testing of the Co_3O_4 catalyst under a range of reaction conditions to elucidate its structural and catalytic properties within this catalytic system; and (2) a comparative analysis of several Co-based spinel oxides to evaluate their performance and selectivity.

The detailed testing of the Co_3O_4 catalyst, provided valuable information regarding its behaviour and structural adaptability under different reaction parameters. However, this intensive focus on Co_3O_4 and its characteristic shoulder in the heating rate of 2°C/min at low temperatures (200°C), also underscored the need for more comprehensive studies on the other catalysts tested, which were examined under only a single set of conditions. For instance, the $NiCo_2O_4$ catalyst demonstrated a distinctive shoulder in its activity profile at a high heating rate and an isopropanol-to-oxygen ratio of 1:1, suggesting unique mechanistic features that merit deeper analysis.

One of the most compelling findings of this thesis are the apparently high catalytic ability of the $CuCo_2O_4$ catalyst and the rather interesting reaction profile of the $NiCo_2O_4$ catalyst. Additionally, while the data suggested that acetone selectivity tends to decrease with temperature, these assumptions could not be conclusively validated. This raises important questions regarding the parameters that govern acetone selectivity and the potential existence of additional, yet unidentified, factors influencing the observed effects.

Future research should focus on systematically varying key parameters, such as reactant ratios, residence times, and reactor configurations, to elucidate the underlying factors controlling acetone selectivity. Expanding the use of advanced characterization tools, including real-time in situ spectroscopy and more extensive TPR analyses, could provide invaluable insights into the structural evolution of catalysts during the reaction.

In conclusion, this thesis provides a strong foundation for the understanding and application of Co-based spinel oxides in isopropanol oxidation, while also highlighting several avenues for future exploration. Addressing the identified gaps and questions through targeted experimental and theoretical approaches will be crucial in advancing the field and optimizing these catalysts for industrially relevant processes.

6 Appendix

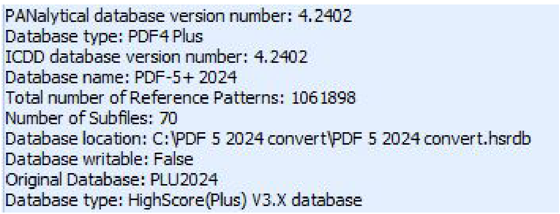

```
PANalytical database version number: 4.2402
Database type: PDF4 Plus
ICDD database version number: 4.2402
Database name: PDF-5+ 2024
Total number of Reference Patterns: 1061898
Number of Subfiles: 70
Database location: C:\PDF 5 2024 convert\PDF 5 2024 convert.hsrdb
Database writable: False
Original Database: PLU2024
Database type: HighScore(Plus) V3.X database
```

Figure 54: XRD database information

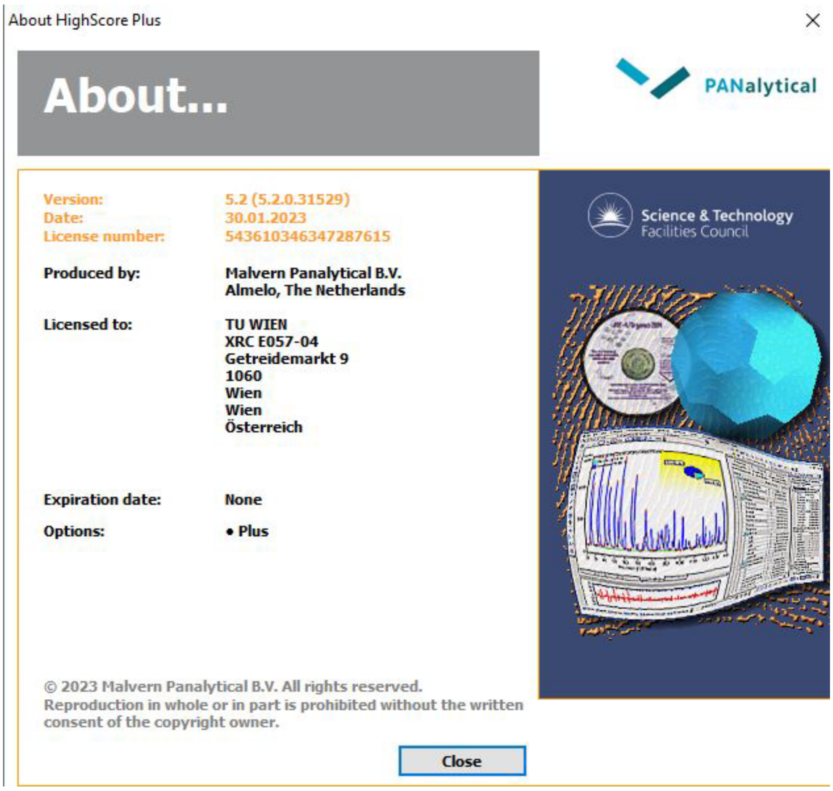

Version: 5.2 (5.2.0.31529)
Date: 30.01.2023
License number: 543610346347287615

Produced by: Malvern Panalytical B.V.
Almelo, The Netherlands

Licensed to: TU WIEN
XRC E057-04
Getreidemarkt 9
1060
Wien
Wien
Österreich

Expiration date: None

Options: • Plus

© 2023 Malvern Panalytical B.V. All rights reserved.
Reproduction in whole or in part is prohibited without the written consent of the copyright owner.

Figure 55: XRD program information

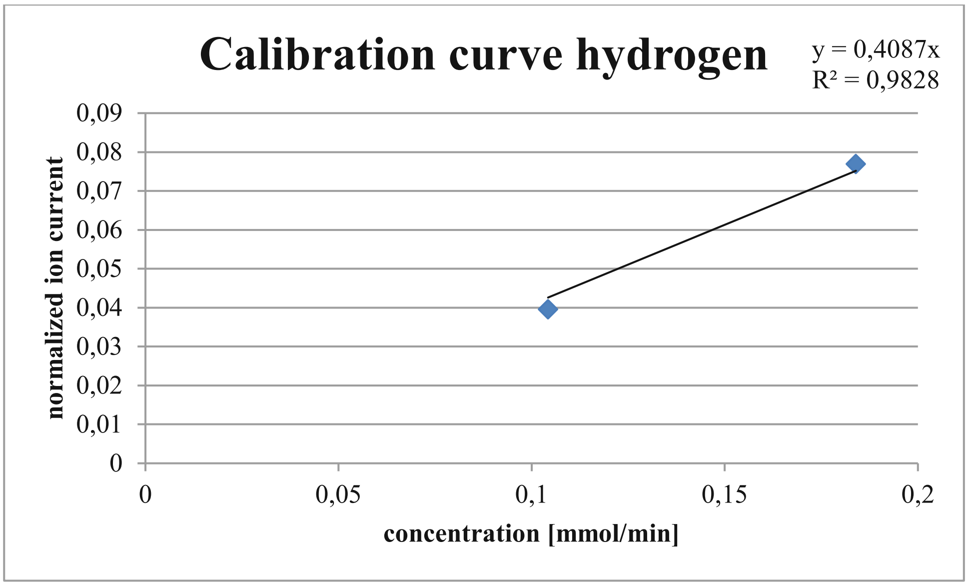

Figure 56: Calibration curve of hydrogen

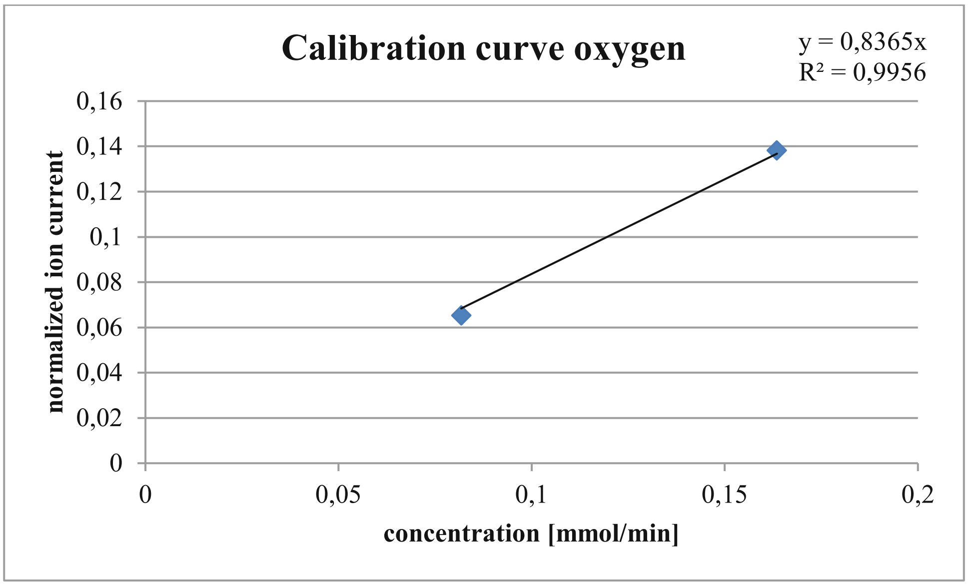

Figure 57: Calibration curve of oxygen

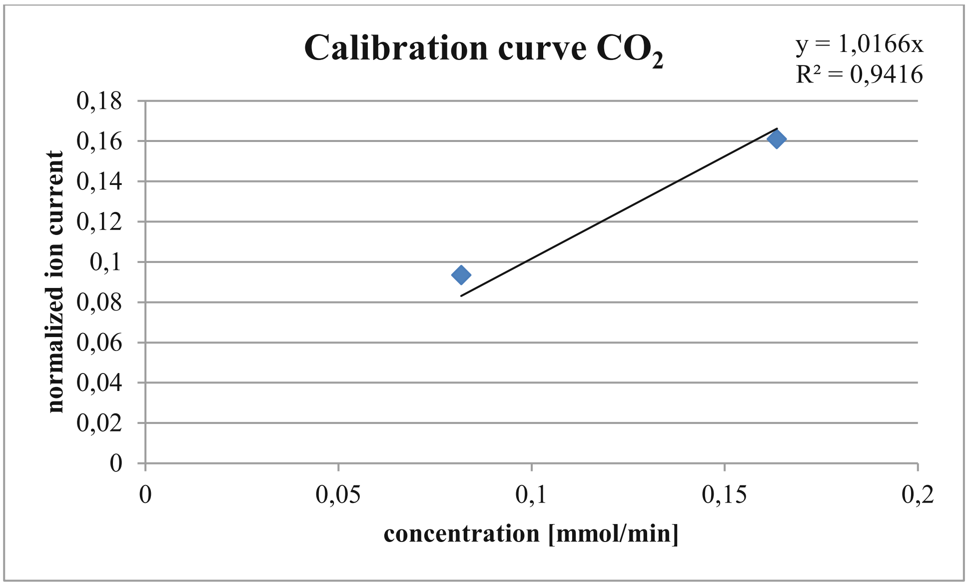

Figure 58: Calibration curve of CO_2

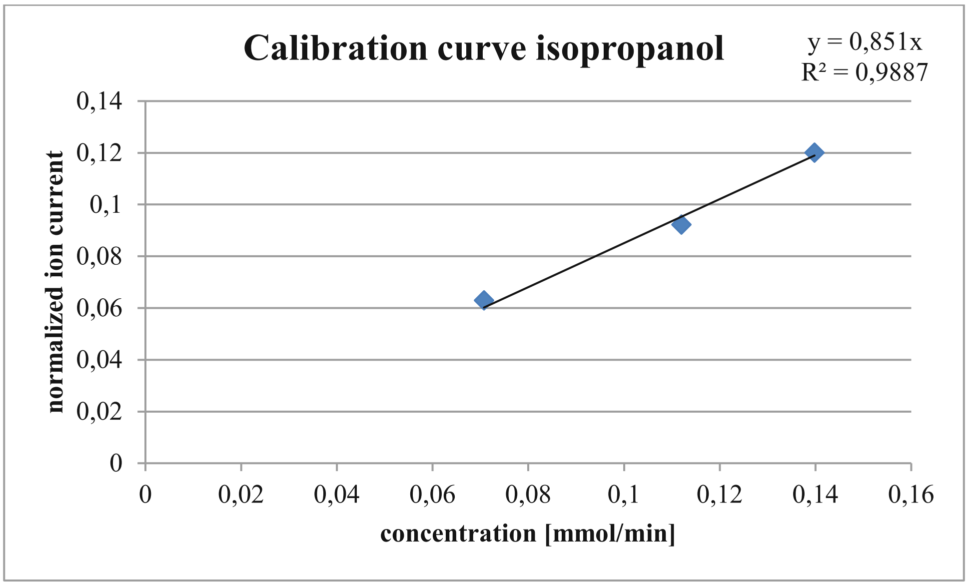

Figure 59: Calibration curve of isopropanol

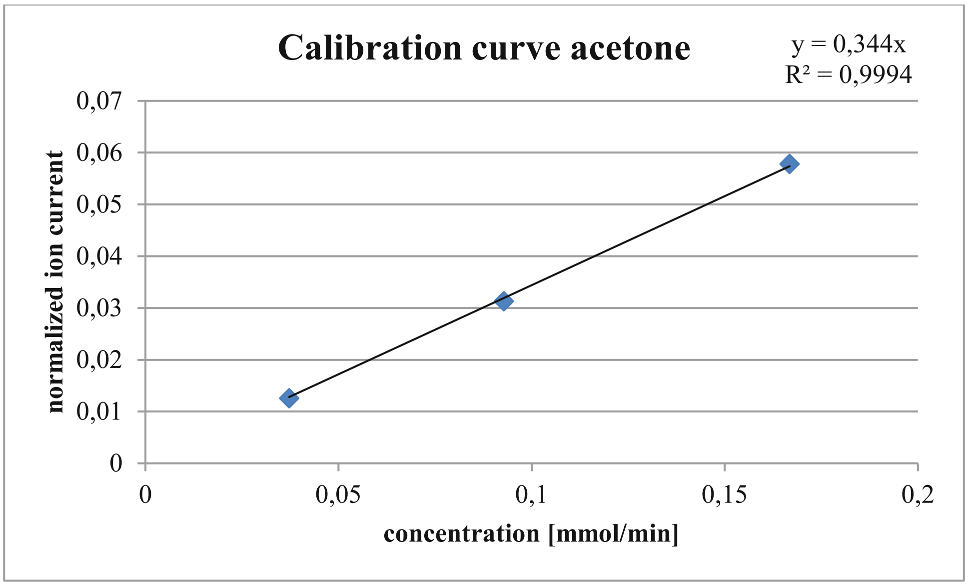

Figure 60: Calibration curve of acetone

7 References

A. K. Lebechi, A. K. (2022). Porous spinel-type transition metal oxide nanostructures as emergent electrocatalysts for oxygen reduction reactions. *Royal Society of Chemistry*, pp. 10717-10737.

A. Tampieri, F. R. (2024, October). Towards industrially-relevant liquid-phase flow.

A. Yelten-Yilmaz, S. Y. (2018, June 1). Wet chemical precipitation synthesis of hyfroxyapatite (HA) powders. *Ceramics International*, pp. 9703-9710.

C. Rodriguez, S. M. (2023, April 14). Operando DRIFT-MS for studying the oxidative steam reforming of ethanol (OSRE) reaction. *MethodsX*.

D. Srikala, S. D. (2. October 2024). Overview on Spinel Oxides: Synthesis and Applications in Various Fields. *Physics of the Solid State*, S. 327-340.

E. d. Hoffmann, V. S. (2007). *Mass Spectrometry: Principles and Applications (Third Edition).* West Sussex: Wiley.

F. Kapteijn, J. A. (2008). Laboratory testing of solid catalysts. In H. K. G. Ertl, *Handbook of Heterogeneous Catalysis (2nd Ed.)* (pp. 2019-2045). Weinheim: Wiley-VCH.

G. A. Somorjai, Y. L. (2010). *Introduction to Surface Chemistry and Catalysis (2nd Edition).* John Wiley & Sons.

G. F. Forment, K. B. (2010). *Chemical Reactor: Analysis and Design (3rd Edition).* Hoboken: Wiley.

G. Rupprechter, K. F. (2023). *Kinetik und Katalyse .* TU Wien.

J. Brame, C. G. (2016, September). Surface Area Analysis Using the Brunauer-Emmett-Teller (BET) Method. *Environmental Quality and Technology Research Program*.

J. Subrt, V. S. (2006, October 24). Synthesis of spherical metal oxide particles using homogeneous precipitation of aqueous solutions of metal sulfates with urea. *Powder Technology*, pp. 33-40.

K. E. Sickafus, J. M. (2004, December 21). Structure of Spinel. *Journal of the American Ceramic Society*, pp. 3279-3292.

M. A. Reiche, M. M. (2000, March 13). Characterization by temperature programmed reduction. *Catalysis Today*, pp. 347-355.

M. Boudart, G. D.-M. (1984). *Kinetic of Heterogeneous Catalytic Reactions.* Princeton University Press.

M. D, A. C. (2015, February 26). Heterogeneous Catalyst Deactivation and Regeneration: A Review. *Advances in Catalyst Deactivation*, pp. 145-269.

M. Thommes, K. K.-R. (2015). *Physisorption of gases, with special reference to the evaluation of surface area and pore size distribution (IUPAC Technical Report).* IUPAC & De Gruyter.

N. Sisakyan, G. C. (2023, November). Combustion Synthesis of Materials for Application in Supercapacitors: A Review. *Nanomaterials*.

Ostrovskii, N. M. (2022, March 23). Coking of Catalysts: Mechanisms, Models, and Influence. *Kinetic and Catalysis*, pp. 52-66.

P. Guggenberger, T. P. (May 2024). Low-Temperature controlled synthesis of nanocast mixed metal oxide. *Journal of Colloid And Interface Science*, S. 574-587.

P. H. Silva, H. S. (2020, April). Redox effects in Cu, Co or Fe in oxides nanocrystals with high catalytic activity for the acetonitrile combustion. *SN Applied Sciences*.

R. J. Harrison, A. P. (November 1998). The Magnetic Properties and Crystal Chemistry of Oxide Spinel Solid Solutions. *Surveys in Geophysics*, S. 461-520.

R. Kellogg, P. L. (1998, October 12). The production of acetone .

R. Prins, A. W. (2022). *Introduction To Heterogeneous Catalysis (Second Edition).* London: WSPC (EUROPE).

S. Najafishirtari, K. F. (2021, December 6). A persepective on Heterogeneous Catalysts for the Selective Oxidation of Alcohols. *Chemistry: A European Journal*, pp. 16809-16833.

S. R. Aravamuthan, S. S. (2013, October). An in Situ Graphite-Grafted Alkaline Iron Electrode for Iron-Based Accumulators.

Suresh, S. (2017, March). Precipitation method and characterization of cobalt oxide nanoparticles. *Applied Physics A* .

T. Falk, E. B. (16. November 2022). Doping of Nanostructured Co3O4 with Cr, Mn, Fe, Ni, and Cu for the Selective Oxidation of 2-Propanol. *ACS Applied Nano Materials*.

Thomas, R. (2001, October 1). Beginners's Guide to ICP-MS: PartVI - The Mass Analyzer. *Spectroscopy Tutorial*.

Thomas, R. (2002, April 1). A Beginner's Guide to ICP-MS: Part X - Detectors . *Spectroscopy Tutorial*.

Wagner, E. (1. May 1934). Oxidation of isopropyl alcohol to acetone. A student experiment. *Journal of Chemical Education*.

Warren, B. E. (1941, May 01). X-Ray Diffraction Methods. *Journal of Applied Physics*, pp. 375-384.

X. Wang, M. Q. (2017, September 30). Effect of glycine on one-step solution combustion synthesis of magnetite nanoparticles". *Journal of Alloys and Compounds*, pp. 288-295.

Y. Wang, X. W. (2019, April). Effect of Formic Acid Treatment on the Structure and Catalytic Activity of Co3O4 for N2O Decomposition. *Catalysis Letters*.

Y. Waseda, E. M. (2011). *X-Ray Diffraction Crystallography.* Springer Berlin Heidelberg.

8 List of figures

9 List of tables